Investigation of High Pulse Energy Solid State UV Laser Sources for Ablation of Corneal Tissue

PhD Thesis

Geoffrey Thomas Dair BSc. (Hons)

This thesis is presented for the degree of Doctor of Philosophy of

the University of Western Australia,

Centre for Ophthalmology and Visual Science,

2002

Abstract

The aim of this project was to develop, characterise and utilise high power solid state lasers for ophthalmic applications. Currently, excimer lasers operating in the UV, are widely and successfully employed to perform corrective refractive surgery. A more robust solid state laser with an output wavelength also in the UV would provide an attractive alternative to the current technology.

This project comprised two main objectives. The first objective involved the identification and development of an appropriate solid state laser to produce UV pulses. Two flash-lamp pumped, low repetition rate, Q-switched laser sources were investigated for this purpose. A Ti:sapphire and an Nd:YAG laser employing nonlinear optical crystals to convert the fundamental IR output wavelength into the UV were examined. For the Nd:YAG laser this meant generating the fifth harmonic wavelength of 213nm. In the case of the Ti:sapphire laser, an attempt was made to generate the fourth harmonic wavelength in the 210 – 220nm range.

The harmonic generation results for the Ti:sapphire laser were inadequate. Conversion to the second harmonic wavelength was limited to only a few percent and fourth harmonic energies were below the noise limit of our measuring equipment. In contrast, the fifth harmonic generation of the Nd:YAG laser operated with an overall conversion efficiency of typically >8% for an optimal 1064nm pump fluence. This translated to over 25mJ pulse energy at 213nm. This increased energy at 213nm allowed large beam ablations to be performed at this wavelength for the first time.

The second objective sought to characterise the ablation behaviour of these lasers. The materials investigated for ablation included porcine corneal tissue as well as the polymers PMMA and PHEMA. Due to the low UV energies generated with the

Ti:sapphire laser, only the Nd:YAG laser was used for quantitative ablation rate studies.

The fifth harmonic wavelength of this laser was further characterised in terms of the transmissive properties through various solutions commonly used in clinical ophthalmic practice. These included 0.9% sodium chloride solution and balanced salt solution. The results were then compared with those obtained at the excimer laser wavelength of 193nm.

For the ablation rate studies involving the polymer materials, ablation depth was measured using a light microscope. For the corneal tissue study, depth measurement was achieved using a more novel method. The ablated areas were measured using a confocal microscope arrangement. The data obtained from this process was then analysed using an algorithm based on extrapolation of the data points comprising the corneal surface and the ablated region.

The ablation rate of PMMA ranged from 0.11μm/pulse for a fluence value of 80mJ/cm^2 to 0.4μm/pulse at 335mJ/cm^2. For the dry PHEMA samples, the ablation rate was 0.06μm/pulse at 80mJ/cm^2 and increased to 0.40μm/pulse for a fluence of 320mJ/cm^2. The ablation rate of wet PHEMA was approximately 45% higher than the rates obtained for the dry PHEMA samples. These rates were lower than those observed for the porcine corneal tissue for which the ablation rate increased from 0.45 to 0.8μm/pulse for fluence values ranging between 150 and 250mJ/cm^2.

Absorption coefficients in balanced salt solution for the 193 and 213nm wavelengths were found to be 140 and 6.9cm^{-1}, respectively. In 0.9% sodium chloride solution, the absorption coefficient was 81cm^{-1} at 193nm and 0.05cm^{-1} at 213nm. In terms of the transmission properties through solution, the experiments revealed strongly reduced absorption for the longer wavelength of 213nm. While the difference in wavelength

between 193 and 213nm is about 10%, the respective molar absorption coefficients varied by one to four orders of magnitude. The increased penetration depths through sodium chloride and balanced salt solutions indicate that these substances cannot be used as a masking agent for keratorefractive procedures performed with the wavelength of 213 nm.

In conclusion, this study confirms that the corneal ablation properties at 213nm are comparable to the 193nm excimer laser wavelength. Increased pulse energy was obtained for the fifth harmonic of Nd:YAG lasers at 213nm through the use of new nonlinear optical crystals (CLBO) to perform the frequency conversion. The Ti:sapphire flashlamp pumped laser appears not to be a viable pulsed UV laser source for the current application.

Acknowledgments

Completion of this project would not have been possible without the help of a number of people. I owe to each of them, a debt of gratitude. In particular, I wish to give special thanks to the following individuals:

Professor Ian Constable, director of the Lions Eye Institute for not only making the project possible but for his personal involvement and supervision.

Dr. Fred Reinholz for his guidance, friendship and willingness to pass on his unsurpassed knowledge.

Dr. Wayne Pelouch who taught me a great deal about lasers and optics in the initial year of the project.

Mr. Philip Reid for his support, technical discussions and encouragement to persevere when things looked bleak.

Ms Sharon Humphris for lending her considerable ability in technical writing to assist in the preparation of this manuscript, including proof reading and suggestions on style.

Mr. Rob Symmans for making available his technical expertise for the construction of the power supply to drive the Ti:sapphire laser.

Mr. Hank Sciberras, a PhD student colleague, for his friendship and many helpful discussions and insights into possible directions of the research.

My other student colleagues, Dr. Natalie Taylor and Dr. Ross Ashman who were kindred spirits and provided many moments of levity often in trying circumstances.

Ms. Carolyn Boyce for being a good friend throughout the course of the project and for helping me keep things in perspective.

Finally I would like to thank my parents, Bill and Janice, for their unconditional support and constant encouragement to pursue a goal.

Table of Contents

List of abbreviations

AR	Anti – Reflection
BBHR	Broad Band High Reflector
BBO	Barium Borate
BSS	Balanced Salt Solution
CBO	Cesium Triborate
CD*A	Deuterated Cesium Dideuterium Arsenate
CLBO	Cesium Lithium Borate
CW	continuous wave
EGDMA	Ethylene Glycol DiMethAcrylate
FOM	Figure of merit
FWHM	Full width at half maximum
GSGG	Gadolinium Scandium Gallium Garnet
KBBF	Potassium Beryllium Borate Fluoride
KB5	Potassium Pentaborate Tetrahydrate
KDP	Potassium Dideuterium Phosphate
KD*P	Deuterated Potassium Dideuterium Phosphate
KTP	Potassium Titanyl Phosphate
LASIK	Laser assisted In situ keratomileusis
LBO	Lithium Borate
LiCAF	Lithium Calcium Aluminium Fluoride
LiSAF	Lithium Strontium Aluminium Fluoride
PHEMA	Poly(2-Hydroxyethyl Methacrylate)
PMMA	Polymethylmethacrylate
PRF	Pulse Repetition Frequency
PRK	Photo-Refractive Keratectomy
RDA	Rubidium Dihydrogen Arsenate
RDP	Rubidium Dihydrogen Phosphate

RTA	Rubidium Titanyl Arsenate
SBBO	Strontium Barium Borate
SHG	second harmonic generation
YAG	Yttrium Aluminium Garnet
YLF	Yttrium Lithium Fluoride
YSGG	Yttrium Scandium Gallium Garnet
YVO_4	Yttrium Orthovanadate

Chapter 1

1. Introduction

Since the advent of the first laser over forty years ago[1], lasers have become increasingly prevalent in society. Applications have been developed across a broad range of sectors including industry, medicine, commerce and entertainment. In terms of medicine, new applications are being found which mirror the advances being made in the field of laser development.

Ophthalmic applications using lasers have become commonplace only since the mid 1980's, with the Nd:YAG laser being used in capsulotomy procedures for example. Corneal refractive surgery using lasers gained momentum in the 1990's following the development of the excimer laser. Indeed, the current state of the art sees 193nm wavelength excimer lasers in widespread clinical use. Surgical procedures have evolved from PRK to LASIK and these techniques have proved both efficacious, in terms of patient visual outcomes, and safe, with seemingly few side effects.

Despite the encouraging patient results achieved using the procedures mentioned, a number of problems exist which pertain to the use of excimer lasers for ophthalmic applications. These problems include the use of the toxic gas Fluorine[2] creating a safety issue in the clinical environment. Operation of the laser in the atmosphere is also non-optimal due to high water absorption. Therefore, careful monitoring and control of temperature and humidity levels within the clinic is required. From a device perspective, optical delivery design is complicated due to the short optical lifetime of various lens substrate materials. Delivery systems may be purged with nitrogen gas or maintained in vacuum to increase component lifetime, however this adds complexity to

the system. Also, due to the nature of the gases involved, laser cavities of excimer lasers suffer corrosion and therefore require regular maintenance.

The combination of these problems led to the desire to develop a solid state laser alternative to the excimer laser. Solid state lasers can potentially provide increased reliability, robustness of design, safety, and lower operating costs than gas or dye lasers. Also, the physical size of solid state lasers is generally significantly less than gas lasers for the production of an equivalent amount of energy.

The fifth harmonic wavelength of the Nd:YAG laser (213nm) was identified as a possible alternative to the excimer laser in the early 1990's. Early development efforts were hampered by low pulse energies due to low harmonic conversion efficiency. However, with the invention of the nonlinear crystal CLBO, great improvement to the conversion efficiency was obtained[3]. Therefore a renewed need existed to examine the ablation characteristics of this type of laser using a larger beam and pulse energy than had been attempted previously.

The scope of this project sought to affirm the ablation characteristics of a larger beam, high energy 213nm wavelength Nd:YAG laser. As the earlier low pulse energy work also focused on the ablation behaviour, other fundamental work was required to gain an understanding of the ablation and absorption characteristics of this wavelength. This took the form of studies of the absorption properties of various solutions in common clinical use. The 10% shift in wavelength from the excimer 193nm to the solid state 213nm wavelength – while not large – proved decisive when the properties were investigated.

Even though the Nd:YAG laser has been most successful commercially, the opportunity existed for investigation of other potential solid state laser sources. Therefore, Ti:sapphire was considered in this project as a potential solid state laser

source of UV. This involved the development of a viable flashlamp pumped laser device, and the design and optimisation of a suitable harmonic conversion scheme.

1.1 Thesis Overview

The following chapter presents a review of the available relevant literature. The chapter begins with a general discussion of solid state lasers. Emphasis is then given to two flashlamp pumped solid state lasers able to provide the appropriate output wavelength and pulse duration for corneal ablation. These include the Nd:YAG laser and the Ti:sapphire laser. Following this, the nonlinear optical configurations and crystal types that have been used for converting the wavelengths of these lasers into the UV are presented. Focus is given to the crystal properties and interaction types that affect the conversion efficiency. A brief explanation of the nonlinear optical conversion process is also provided. Next, the mechanisms of corneal ablation for various wavelength regions are presented. Also in this section, a review of the methods that have been employed to measure the rate of ablation. The next section is devoted to comparing the results of ablation rate studies conducted on cornea and polymer materials. Finally, a brief discussion of the well-known law of attenuation (Beer-Lambert) of light through solution is given.

Chapter 3 is titled "Development of pulsed laser sources" and examines the work done to characterise the harmonic generation of the Nd:YAG laser source. Later sections of the chapter are devoted to the construction of the flashlamp pumped Ti:sapphire laser source.

Chapter 4 presents the ablation rate results of two polymer materials, specifically PMMA and PHEMA. In the case of the PHEMA experiments, the issue of hydration is discussed in light of the results obtained. The data for both materials is then compared with results from the literature at both the 193 and 213nm wavelengths.

Chapter 5 is dedicated to the presentation and discussion of the ablation of porcine corneal tissue. This chapter is similar in format to chapter 4, although a more detailed discussion of the apparatus and analysis method employed for measuring the ablation rate is given.

Chapter 6 discusses the absorption properties of various substances in solution. The compounds chosen make up the components of BSS, a common solution in clinical use. A comparison is made between the observed transmission properties for both the excimer 193nm and solid state 213nm laser wavelengths. The results are then discussed in terms of the possible implications for use in a clinical environment.

The final chapter of this thesis outlines the conclusions deduced from the project. Scope for future work is discussed and suggestions are made for possible directions of further research.

Chapter 2

2. Literature Review

2.1 Introduction

The emergence of the excimer gas laser as an ophthalmic instrument followed the discovery in the early 1980's that pulsed UV laser radiation could be used to etch various biological materials with high precision and control[4]. The word "excimer" is a hybrid of the terms excited dimer and may be applied to a variety of gas mixtures. An excited dimer is a diatomic molecule, which can only exist in a bound excited state. In the ground state, the molecule forms a monomer[5]. Examples of excimer gas lasers include KrF (248nm), XeCl (308nm) and XeF (351nm). Of particular interest in ophthalmology is the excimer wavelength of 193nm that is produced from argon and fluorine (ArF).

With regards to human vision, the interface formed by the cornea with the surrounding atmosphere is most important. It is at this interface that the eye achieves approximately two thirds of its refractive power. Convenience of access to the cornea for the correction of refractive errors allows surgery to be completed with great efficacy. UV lasers provide improved precision over diamond or steel knives[6] allowing the cornea to be "sculpted" to a required shape. Therefore, laser surgery provides a tremendous advantage for vision correction.

As mentioned, attempts have been ongoing to develop a solid state laser capable of performing refractive surgery. Although solid state laser mediums generally operate with an output wavelength in the visible to IR region, nonlinear optical crystals have been used to frequency convert these laser outputs to UV wavelengths.

2.2 Solid state lasers

A number of different solid state materials have been developed for laser use. The active ions responsible for producing laser action come largely from the rare earth and transition metal elements of the periodic table. The rare earth ions Neodymium, Erbium, Holmium and Thulium have all been used successfully as laser mediums. Of these, Neodymium and Erbium have received the most interest and found application in a variety of industries. The transition metals Chromium and Titanium are of particular interest for their use as tunable laser sources.

Although the active ion element in a solid state laser material determines the macroscopic output properties of the laser, the specific output wavelength of a particular laser is also dependent upon the host material. Different varieties of glass, sapphire, garnet, vanadate and fluoride have been used as host materials for the active ions mentioned. The crystalline structure (or lack thereof in the case of glass) is responsible for slight shifts in the output wavelength behaviour of most solid state lasers. Predominantly, the output wavelength of these lasers falls in the near to mid IR region of the spectrum. Some solid state laser materials are listed in Table 2.1 along with their output wavelengths.

It should be noted that the list of materials shown in Table 2.1 is far from complete and provides merely a sample of possible solid state laser mediums. The role of the host material in determining the output spectrum of the laser is illustrated in the table for Neodymium, Erbium and Chromium. Chromium, when doped in a sapphire host (Al_2O_3) to form ruby, does not exhibit tunability. However, in the form of Alexandrite ($Cr:BeAl_2O_4$) the chromium ions are able to provide amplification across several vibronic transitions to achieve a wide range of tunability. Likewise, in the YAG and LiSAF hosts the output spectrum is again shifted. Amplification across vibronic transitions is a characteristic of all the tunable lasers listed in table 2.1.

Fixed wavelength		Tunable Lasers	
Laser rod	λ (nm)	Laser rod	λ (nm)
Nd:YLF	1053	Ti:Al_2O_3	680-1000
Nd:Glass†	~1060	Cr:$BeAl_2O_4$	700-820
Nd:YAG	1064	Cr:YAG	1300-1600
Nd:YVO_4	1056	Cr:LiSAF	780-920
Er:Glass	1550	Cr:LiCAF	720-840
Er:YSGG	2790	Co:MgF_2	1750-2500
Er:YAG	2940	Cr:GSGG	700-900
Ho:YAG	2120		
Tm:YAG	2010		
Cr:Al_2O_3	694		

Table 2.1. Spectral output of various solid state laser rods.[7] †Actual wavelength also varies with type of glass.[8]

An equally critical component of a solid state laser system is the proper selection of a pumping method for the laser rod. Unlike gas lasers, which generally employ electrical excitation as the preferred pumping method, solid state lasers are usually pumped via optical means. Methods of optical pumping can be broken into three major categories; noble gas flashlamps (filled with Xenon or Krypton), laser diodes and other lasers. In selecting a pump source a number of factors need to be considered. These include the absorption bands of the active ion, the required laser output power and therefore required pump power, the mode of laser operation and, also repetition rate in the case of pulsed operation.

Until recently, if pulsed operation and large output energies were required (tens of millijoules per pulse) only flashlamps could provide the levels of input pump power to achieve this. Flashlamps are able to discharge large amounts of electrical energy with a controllable duration[9-11]. One disadvantage of flashlamps is the broad spectral output they produce[12]. This may lower the overall efficiency of the laser if too much of the flashlamp output spectrum is contained in wavelengths not within the absorption range of the pump bands of the laser medium.

For use in this project, the Nd:YAG laser was selected due to the wide commercial availability and large output energy of this laser. The Ti:sapphire laser was selected as a second potential source due to the broad tunability this laser presents at the fundamental wavelength. This created the potential to investigate a range of UV wavelengths produced through fourth harmonic generation. Also, from a theoretical viewpoint, harmonic conversion of this laser into the UV can be achieved with a simpler arrangement than that required for the Nd:YAG laser.

2.2.1 Q-switching

One method of achieving an output pulse duration in the nanosecond regime employs a technique known as Q-switching. In this technique the laser cavity is switched from having high round trip loss, such that any laser action is suppressed, to one of low loss. In the low loss state oscillation is allowed to occur and an output pulse results. As this method actively alters the loss parameter of the cavity (Q value) the process is termed Q-switching[13]. The motivation for using Q-switching lies in the control that is obtained over the duration, energy and temporal shape of the output pulse. In a free running configuration the output pulse builds up according to the rate equations of the laser medium and the upper state lifetime. A Q-switched pulse is produced when the cavity is "opened" as the population inversion reaches a maximum. In this instance a very large amount of gain is achieved within the laser cavity and the laser pulse builds up rapidly. With such a rapid build up an output pulse of much shorter duration than that achieved for a free running cavity is observed.

Conceptually at least, Q-switched operation may be achieved by simply placing a shutter within the laser cavity. A number of configurations have been used to produce this shuttered action. Properties that come into consideration when designing a Q-switch include the desired repetition rate of the output pulse, switching time from the

low to high Q states, amount of internal losses introduced to the cavity, simplicity in terms of the number of components required and, of course, cost. One of the first Q-switching methods employed a mechanically rotated prism within the cavity which acted to periodically misalign the cavity[14]. The limitations of such an arrangement included a high sensitivity to misalignment, switching time and the repetition rates able to be achieved. Saturable absorber dye cells have also been used[15,16]. Saturable absorbers work by using a dye which has variable transparency with intra-cavity light intensity. That is, when the intensity within the cavity reaches a threshold value, the cell becomes bleached and no further absorption takes place (the shutter is open). At the intensity values below this threshold the cell is effectively opaque and oscillation cannot occur. Use of such cells is known as passive Q-switching since no external triggering or timing circuitry is required for successful operation.

Q-switches using acousto-optic modulation have also been developed[17]. The advantage of the acousto-optic modulator is that very high repetition rates are able to be realised. Repetition rates of up to the order of ~50kHz have been achieved[8]. In this arrangement an acoustic pulse is typically applied to a quartz block. The effect of the acoustic pulse is to alter the lattice structure of the quartz and hence the refractive index. This small perturbation is enough to misalign the laser cavity as any propagating light is diffracted away from the cavity axis.

Perhaps the most common method of Q-switching utilises the Pockels cell. A Pockels cell makes use of the electro-optic effect observed in some nonlinear materials. Similar to the acousto-optic modulator, the refractive properties of the nonlinear crystal within the Pockels cell are altered upon the application of a DC voltage pulse, rather than an acoustic wave. More specifically, the electric field induced due to the application of the DC voltage introduces a birefringence within the crystal. In this state, the material provides retardation to one of the polarisation components of the propagating light. The degree of retardation is proportional to the magnitude of the applied voltage. Therefore

a Pockels cell can conveniently be made to behave as a quarter or half wave plate as needed for a given wavelength. Further components are required to complete the shutter arrangement. These generally include a polariser and a fixed quarter wave plate depending on the configuration used. Figure 2.1 shows one possible schematic of a laser cavity employing a Pockels cell Q-switch.

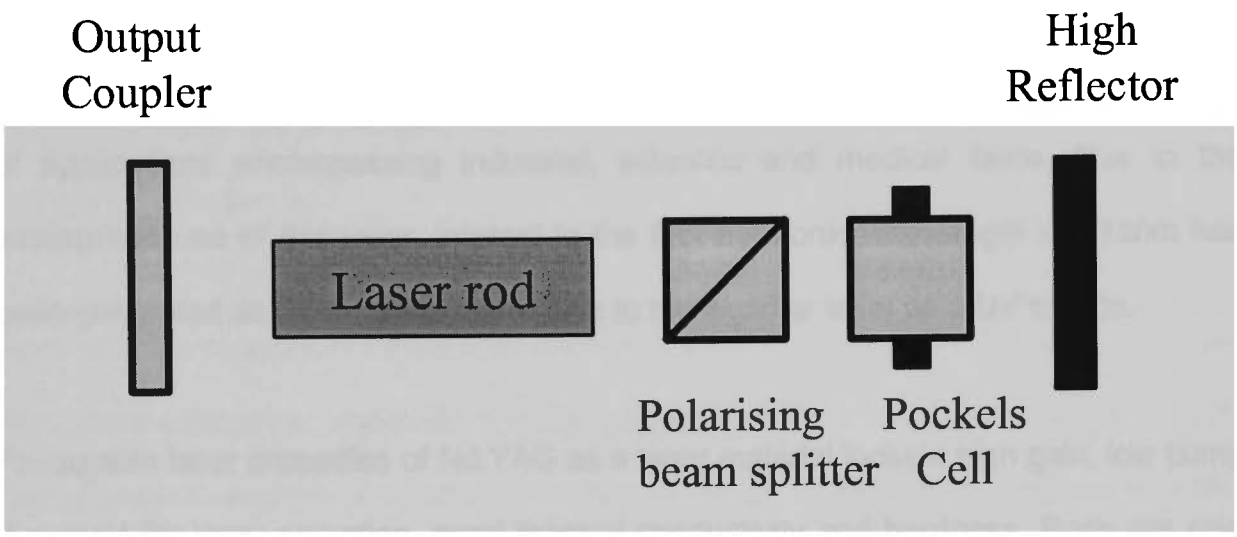

Figure 2.1. Q-switched laser cavity requiring λ/4 voltage to suppress laser action.

In this cavity, the quarter wave voltage is applied to the Pockels cell (typically several kilo-volts) to suppress laser action. This occurs since the polarisation of any light making two passes through the Pockels cell will be rotated through 90° upon returning to the polariser element. The light is then ejected from the cavity by the polarising beam splitter and optical feedback is prevented. To initiate laser output, the voltage is removed from the Pockels cell and therefore the polarisation of any light remains unaltered after passing through the Pockels cell. This configuration requires the DC voltage to be applied to the Pockels cell for the duration of the pump cycle, which may be on the order of tens to hundreds of microseconds. On the other hand, insertion of a fixed quarter wave plate between the Pockels cell and polarising element is able to circumvent this requirement. With the quarter wave plate in place, laser action is suppressed with no voltage applied to the Pockels cell. The Q-switched output pulse is initiated only when the voltage is applied. Such a configuration requires an extra

element within the cavity but greatly reduces the time high voltage is applied to the cell. This increases the life of the Pockels cell immensely and is therefore a preferred configuration.

2.2.2 The Nd:YAG Laser

As a commercial product, the Nd:YAG laser has generated much interest as a reliable solid state source of near IR radiation. Nd:YAG lasers have been used in a wide variety of applications encompassing industrial, scientific and medical fields. Due to the widespread use of this laser, interest in the fifth harmonic wavelength of 213nm has been generated as a solid state alternative to the excimer laser as a UV source.

Favourable laser properties of Nd:YAG as a laser material include high gain, low pump threshold for laser operation, good thermal conductivity and hardness. Rods are also able to be grown with a high degree of optical quality[5,8]. Dimensions of cylindrical rods have been produced up to 12mm in diameter and 150mm in length. Doping concentrations of Nd ions in the YAG host material generally range between 0.7 to 1.0% by weight. Higher doping concentrations tend to affect the optical quality of the rod and produce strain within the crystal.

The Q-switched Nd:YAG laser is able to produce pulses of large energies with a duration comparable to that of excimer lasers. Commercially, Nd:YAG lasers operating in a pulsed mode are available with output pulse energies ranging from a few millijoules to several Joules and with repetition rates up to several hundred Hertz. Rods used in a single oscillator laser system are capable of producing output pulse energies of 800mJ (PRF 10Hz)[18] or 450mJ (PRF 50Hz)[19]. Even larger pulse energies of several Joules are available with multiple rod oscillator or oscillator-amplifier configurations[20]. The amplifier stage of this configuration can also comprise multiple successive stages.

Nd:YAG represents a four level laser system. The main laser transition occurs at the infrared wavelength of 1064.1nm and the upper state fluorescence lifetime is ~230μs. Absorption bands in the infrared occur primarily around the 750 and 810nm wavelengths. These absorption bands coincide well with the output spectrum of flashlamps filled with Krypton gas and also laser diodes. Figure 2.2 shows the fluorescence spectrum of Nd:YAG over a limited wavelength range. Along with the main laser transition shown, several other nearby transitions are also possible with Nd:YAG. This is due to the manifold nature of the energy levels that make up the upper and lower laser levels.

Generally, commercial Nd:YAG lasers employ an unstable resonator design. Unstable resonators offer large fundamental mode volume, greater energy extraction and lower output beam divergence than stable resonators. An unstable resonator design was first applied to a Q-switched Nd:YAG laser in the late 1970's[21,22]. This configuration included a "hard" aperture output mirror, which resulted in an annular output beam profile in the near field.

The fabrication of output mirrors with a reflectivity having a radial dependence from the centre of the mirror substrate made the use of unstable resonators commercially viable. Variable reflectivity mirrors provide the cavity with a "soft" aperture, allowing the output beam to have a smooth gaussian profile in the near field. Furthermore, it was shown that the fundamental mode profile could be manipulated by altering the profile of the variable reflective mirror[23-26]. Additional work to improve the average output power capabilities of these resonators took the thermal lensing of Nd:YAG rods into account[27,28]. Thermal lensing is a phenomenon observed in laser rods where the refractive power of the rod changes with input pump power as this increases the temperature of the rod. The resonator cavity therefore, is usually designed for a specified range of input powers.

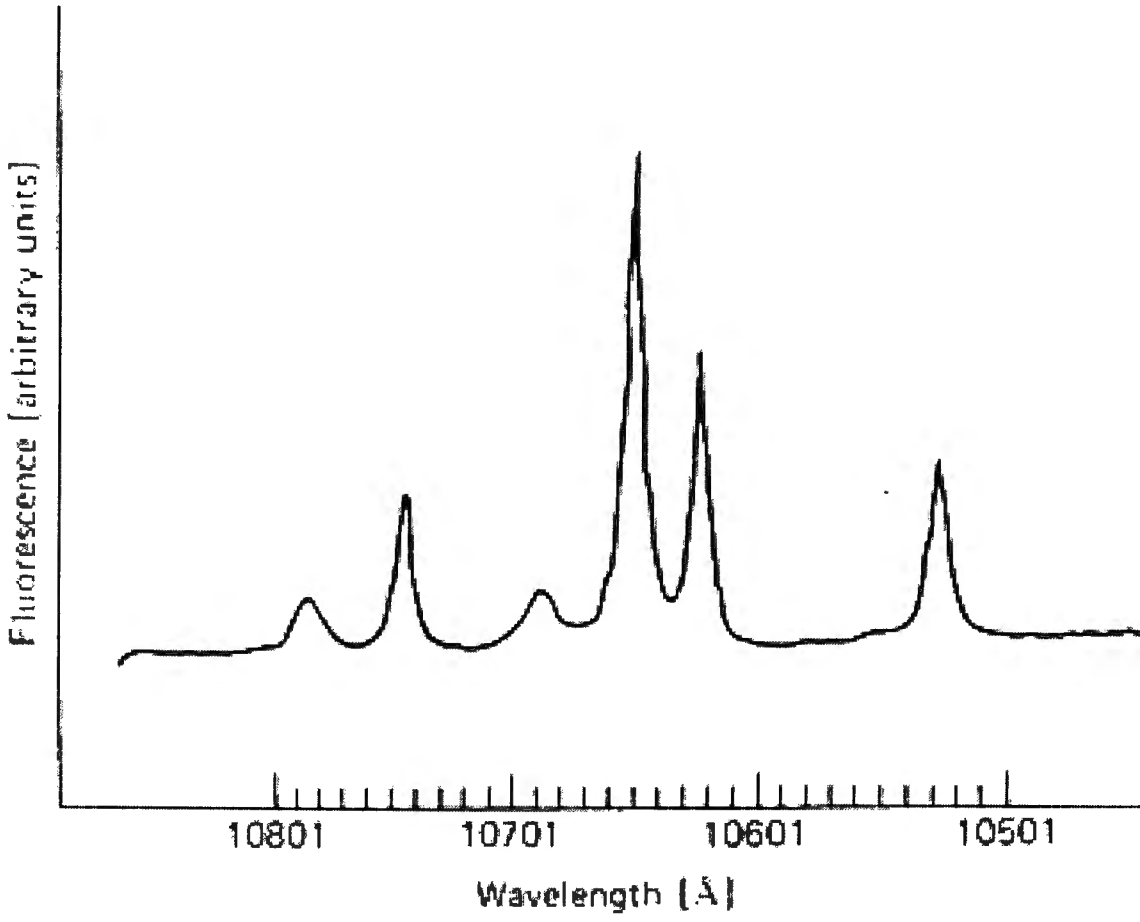

Figure 2.2. Fluorescence spectrum of Nd:YAG. Main laser transition occurs at 10641 Angstroms. (Koechner[8])

Another important advantage of the improved output beam profile from unstable resonators using variable reflectivity mirrors was the affect this had on harmonic generation. The conversion efficiency of the second harmonic generation process was increased to 60% with an unstable resonator compared with 44% for a stable resonator configuration. These experiments were done using a CD*A crystal with a type 1 interaction[29]. The process of harmonic generation is described in greater detail in section 2.3 below.

2.2.3 The Ti:Sapphire Laser

Solid state lasers incorporating Ti^{3+} ions in a sapphire host have attracted a great deal of interest since laser action was first reported in this medium in 1982[30]. The extremely

broad tunability of the laser output wavelength, which extends from 670nm to 1070nm, is responsible for generating the interest surrounding this laser source. Other desirable properties of Ti:sapphire as a laser medium include high thermal conductivity and mechanical sturdiness. The laser output is linearly polarised due to the birefringence of the material and the peak of the gain linewidth occurs at a wavelength of ~790nm.

In determining the optical quality of the laser rod, a dimensionless quantity known as the figure of merit (FOM) is often cited. This is defined as the ratio of the absorption coefficient at a given pump wavelength to that for a given laser wavelength. The wavelengths are generally selected to coincide with the central portion of the respective bandwidths. Not surprisingly, laser rods with high FOM values (several hundred) have been shown to improve slope efficiency and reduce the laser threshold[31-33].

Ti:sapphire lasers have become commercially available[34] operating in the cw mode and being pumped by Ar:ion or frequency doubled Nd:YAG, YLF and vanadate lasers. The output wavelength of these pump laser sources occurs within the 480-550nm range which corresponds to the region of greatest absorption for Ti:sapphire. The absorption and fluorescence spectrums for each direction of polarisation with respect to the optical axis of the material are displayed in Figure 2.3. The broad output linewidth of Ti:sapphire lasers has also meant that ultrashort pulses of a few femtoseconds duration can be produced when operated in a mode locked configuration[35-39]. This is due to the relationship known as the time-bandwidth product which is a constant that depends on the pulse shape[13]. Therefore, a broad spectral bandwidth makes possible the generation of short duration pulses; provided the pulse can be made to propagate free of chirp.

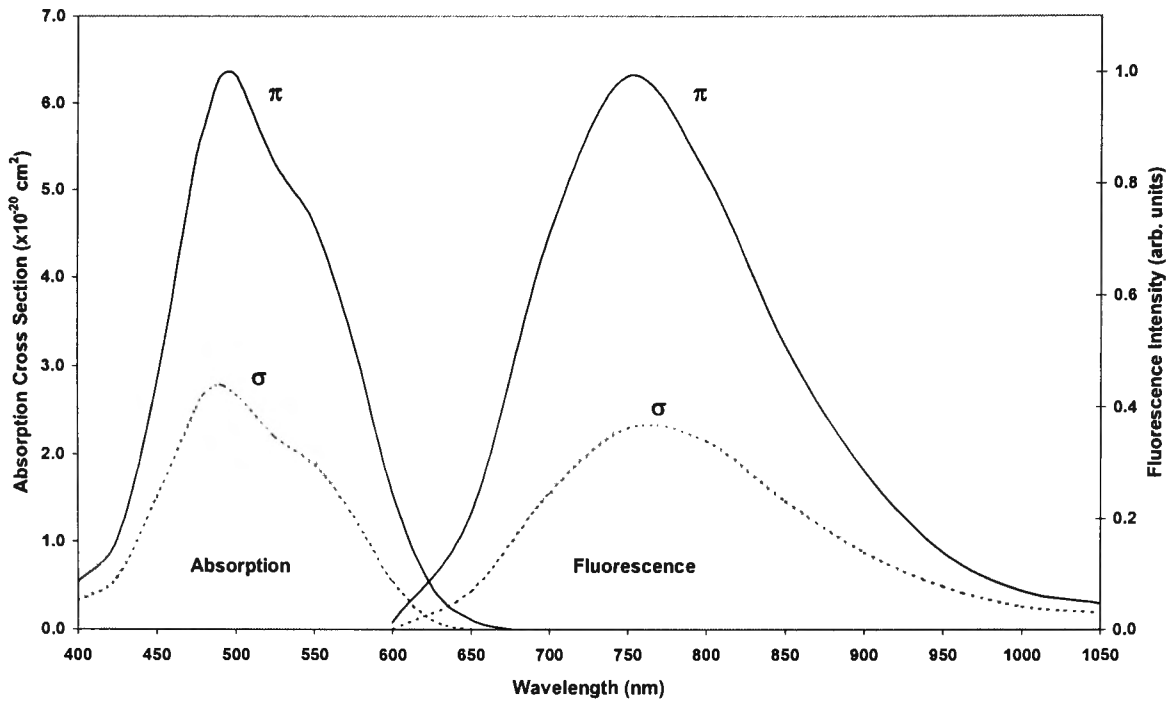

Figure 2.3. Fluorescence and absorption spectrum of Ti:sapphire for both orientations of polarisation. (Moulton[40])

Pulsed operation of the Ti:sapphire laser in the nanosecond regime has been achieved using the techniques of gain switching and flashlamp pumping. In gain switching, the laser is pumped by another pulsed laser with a duration a number of orders of magnitude shorter than the upper state lifetime of the sapphire rod. This results in a rapid population inversion occurring in the laser material and a single nanosecond pulse is output. Frequency doubled Q-switched Nd:YAG lasers have been employed as pump sources for gain switched Ti:sapphire lasers[41-43] with pulse durations as short as 10ns.

Flashlamp pumping is more difficult owing to the short upper state lifetime of Ti:sapphire (3.2μs) and the requirement for efficient pumping, which demands that the pump pulse be of similar order duration. Also, the upper state lifetime is temperature dependent[44] (Figure 2.4) and decreases rapidly in the 200-500K temperature range. At temperatures below 200K, the lifetime is constant at 3.85μs. This temperature

dependence gives increased importance to the cooling of the laser rod when operated in a repetitively pulsed mode[45].

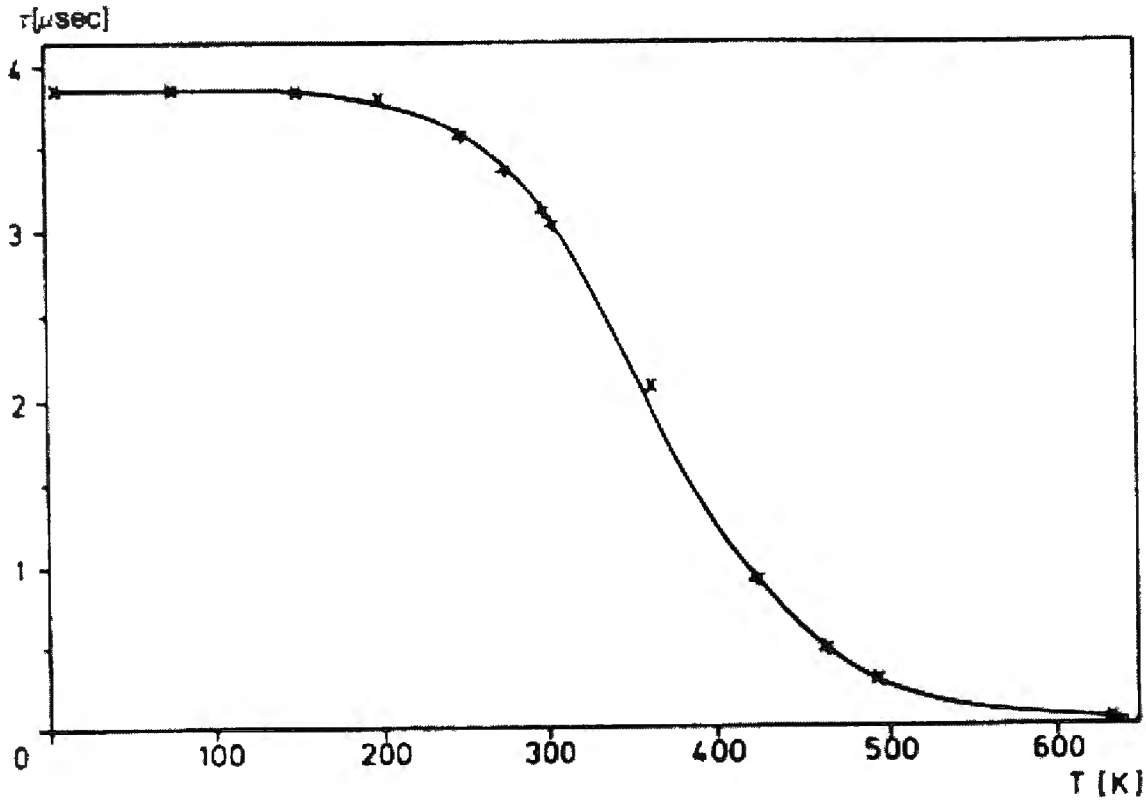

Figure 2.4. Temperature dependence of the upper state lifetime of Ti:sapphire. (Albers *et al.*[44]).

This problem of requiring short pump pulse duration is further accentuated by the shift in the flashlamp output spectrum towards the UV for short pulse operation due to an increased current density within the flashlamp[12]. This is illustrated in Figure 2.5 which shows the output spectrum of a Xenon gas filled flashlamp for two current density values. The spectral shift towards shorter wavelengths is quite evident for the larger current density value. With this spectral shift, less optical pump power is available at the optimum absorption band for Ti:sapphire as seen in Figure 2.3 above. In addition to reducing the efficiency of the laser, the laser rod is susceptible to degradation due to the formation of absorption bands resulting from exposure to an increased amount of UV radiation[46,47].

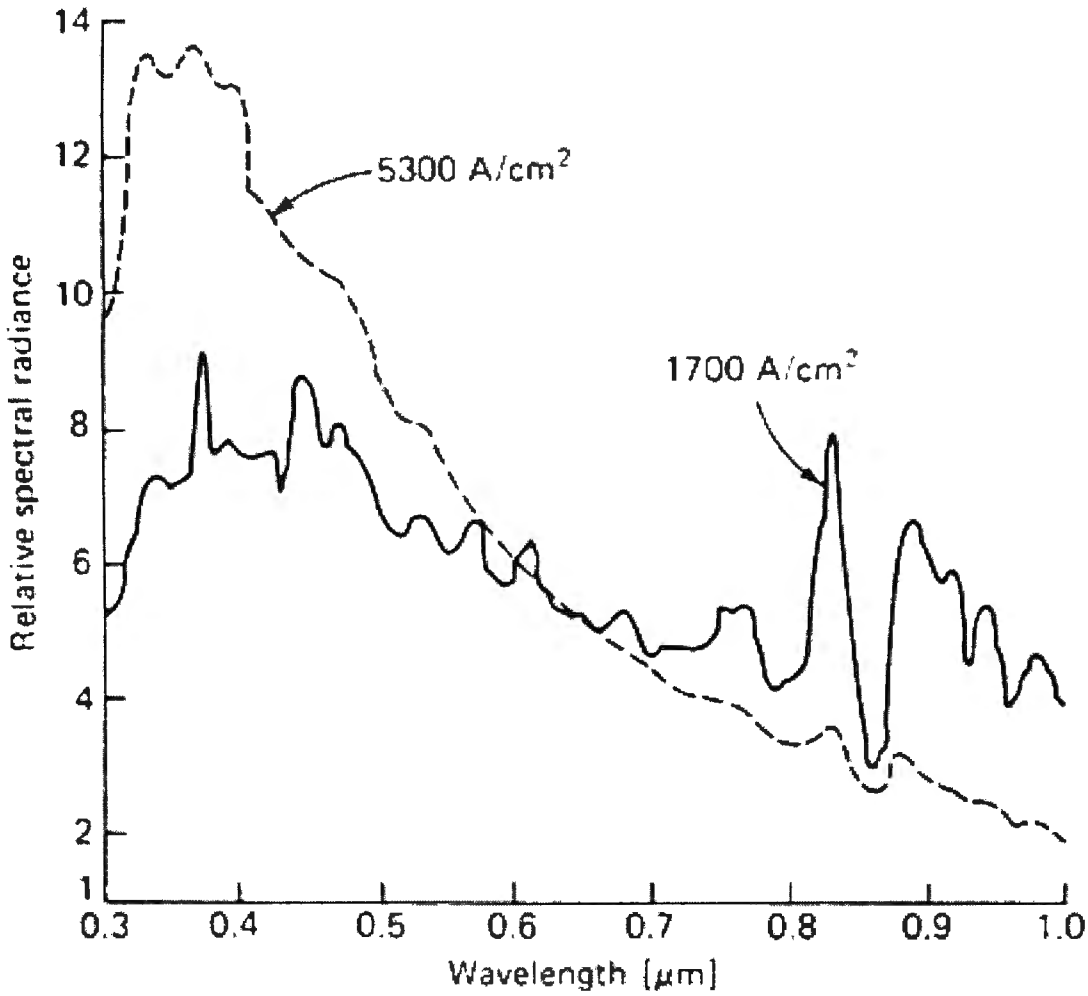

Figure 2.5. Xenon gas filled flashlamp output spectrum for two current densities. Gas fill pressure was 300 Torr. (Koechner[8]).

Despite these problems, flashlamp pumping was reported at almost the same time by Esterowitz *et al.*[48] and Sevast'yanov *et al.*[49] in 1984. Subsequent work concentrated on employing a fluorescent converter dye solution which acted to convert near UV light of the flashlamp output spectrum into the blue-green absorption band of Ti:sapphire[50]. These studies all had low pulse energies and low slope efficiencies of less than 0.5%. Brown and Fisher[51] achieved a large pulse energy of 6.5J, however this required 1200J of input energy, also corresponding to an efficiency of ~0.5%. Large improvements were made in the laser slope efficiency by using flashlamps having an envelope constructed of cerium doped quartz and improved close-coupled pump chamber design. Doping of the flashlamp envelope with cerium acts to filter UV spectral components of the flashlamp emission in order to inhibit the formation of unwanted

absorption bands within the laser rod[45-47]. Without the use of a fluorescent converter dye pulse energies over 4J were realised[45], with an improved slope efficiency of 2.25%. While the advantage of flashlamp pumping is evident through output pulse energies in excess of that achievable through gain switching, it should be noted that the multi-Joule outputs were observed in a free running cavity. Therefore, the pulse duration was between 5-10μs. Also, the temporal profile of an output pulse from a free running cavity is often irregular. In order to achieve nanosecond pulse durations using flashlamp pumping, Q-switching is often employed, which has the effect of limiting the output pulse energy[52] but increasing the peak power.

As discussed, most studies involving flashlamp pumping of Ti:sapphire have operated the laser in a free running mode producing pulse durations of several micro-seconds. Q-switching using a Pockels cell has been demonstrated by several authors[53,54], with Lithium Niobate[55] and KD*P[31,56-58] crystals being employed within the cell. The use of Lithium Niobate crystals achieved limited success due to degradation of the crystal[59]. Using a KD*P crystal based Pockels cell, Titterton and Stokoe[57] reported a Q-switched output pulse energy of 550mJ with a duration of 20ns and PRF of 5Hz. This output was achieved for a flashlamp pump energy of 170J and using a laser rod with an FOM of 300.

2.3 Nonlinear Optics

In general, solid state lasers have a fundamental output wavelength in the infra-red region of the EM spectrum. This is certainly the case with Nd:YAG (1064nm) and Ti:sapphire (~800nm) lasers. In order to broaden the output wavelength range of these lasers into the UV, a method must be used to increase the fundamental output frequencies, e.g by multiplication. Multiplication of the fundamental output frequency of a laser is termed harmonic generation.

Harmonic generation can be explained using the harmonic oscillator model of conventional light propagation through a dielectric medium. When the strength or amplitude of the incident electric field of frequency ω becomes large, additional components or side bands are generated with frequency[60] 2ω. It should be remembered however, that the refractive index through most dielectric media is a function of wavelength. Therefore, the refractive index of the material (and hence the phase velocity) at the fundamental will differ from that of the harmonic frequency. Consequently, as the two waves propagate through the material the harmonic will fall out of phase with the fundamental. At some distance the phase mismatch reaches $\pi/2$ and the amount of harmonic power generated up to this point is a maximum. The distance over which this occurs is termed the coherence length and typically has a value of several microns[61]. Further propagation of the waves results in harmonic power being converted back into the fundamental wave with complete reconversion occurring after a distance through the material of two coherence lengths.

This limitation could be overcome if conditions for propagation of the two frequencies (fundamental and harmonic) were made to be the same. That is, each frequency is able to propagate with the same phase velocity. Such conditions are able to be achieved in a class of dielectric materials referred to as nonlinear crystals. Nonlinear crystals lack a centre of symmetry and therefore exhibit anisotropy. A very useful property of an anisotropic material is birefringence. This is the characteristic of having a different refractive index depending on the polarisation and direction of the propagating wave. A wave polarised perpendicularly to the plane containing the *k* vector and the optic axis is called an ordinary wave (o-wave) and exhibits the same refractive index n^o, regardless of the direction of propagation. In contrast, a wave polarised within this plane is called an extraordinary wave (e-wave) and is characterised by a changing refractive index with direction[62]. The direction for which the refractive index of the o and e-waves are equal defines the direction of the optic axis within the material. The refractive index of the e-wave varies between values n^o along the optic axis and n^e in a

direction 90° to the optic axis. Crystals with one optic axis and $n^e - n^o < 0$ are known as negative uniaxial crystals whereas if $n^e - n^o > 0$ the crystals are positive uniaxial. A crystal having two optic axes is biaxial. The majority of nonlinear crystals used for harmonic conversion are negative uniaxial. Exceptions to this include the biaxial crystals LBO and KTP which are also in common use.

2.3.1 Phase Matching

In terms of conservation of energy, two photons at the fundamental frequency or wavelength are required to produce one photon at the harmonic wavelength. This may be expressed as:

$$\frac{1}{\lambda_1} + \frac{1}{\lambda_2} = \frac{1}{\lambda_3} \qquad \textbf{Equation 2.1}$$

Where λ_n represents the wavelengths of the fundamental and harmonic waves.

In the case of second harmonic generation, $\lambda_1 = \lambda_2$, and $\lambda_3 = \lambda_1/2$ is the generated harmonic wavelength. This equation also suggests that it is possible to generate odd harmonic wavelengths where $\lambda_1 \neq \lambda_2$. This is called sum frequency generation. Indeed, second harmonic generation can be thought of as a special case of sum frequency generation where the two input wavelengths are equal.

Conservation of momentum in the harmonic process requires that[63]

$$\Delta k = \tilde{k}_1 + \tilde{k}_2 - \tilde{k}_3 = 0 \qquad \textbf{Equation. 2.2}$$

where Δk represents the phase mismatch of the interacting wavelengths and k_n, represents the wave vectors.

The situation of harmonic generation described above in section 2.3 applies to the case where $\Delta k \neq 0$. As mentioned, in this instance harmonic conversion occurs over the

coherence distance of the material. Only if the phase mismatch can be made to be close to zero can a significant amount of harmonic conversion take place. For the phase matched case, equation 2.2 may be restated in terms of refractive index and wavelength since $k = 2\pi n/\lambda$, resulting in:

$$\frac{n_1}{\lambda_1} + \frac{n_2}{\lambda_2} = \frac{n_3}{\lambda_3} \qquad \textbf{Equation 2.3}$$

Two types of phase matching interactions are possible. If the polarisations of the input waves are the same, the interaction is termed Type 1 phase matching, while the phase matching is known as Type 2 if the input polarisations are orthogonal. For Type 1 SHG in a negative uniaxial crystal the input beams will be o-waves and the harmonic will be an e-wave.

In this case, equation 2.3 reduces to :

$$n_1^o(\lambda) = n_3^e(\lambda, \theta) \qquad \textbf{Equation 2.4}$$

which is shown graphically in figure 2.6 below that depicts a cross section of the index surface within a nonlinear crystal.

Figure 2.6 also illustrates why the input beams for a type 1 interaction must be ordinary in a negative uniaxial crystal. There is no point of intersection between the e-wave index at the fundamental wavelength (n_1^e) and the o-wave index at the harmonic wavelength (n_2^0), therefore phase matching cannot occur.

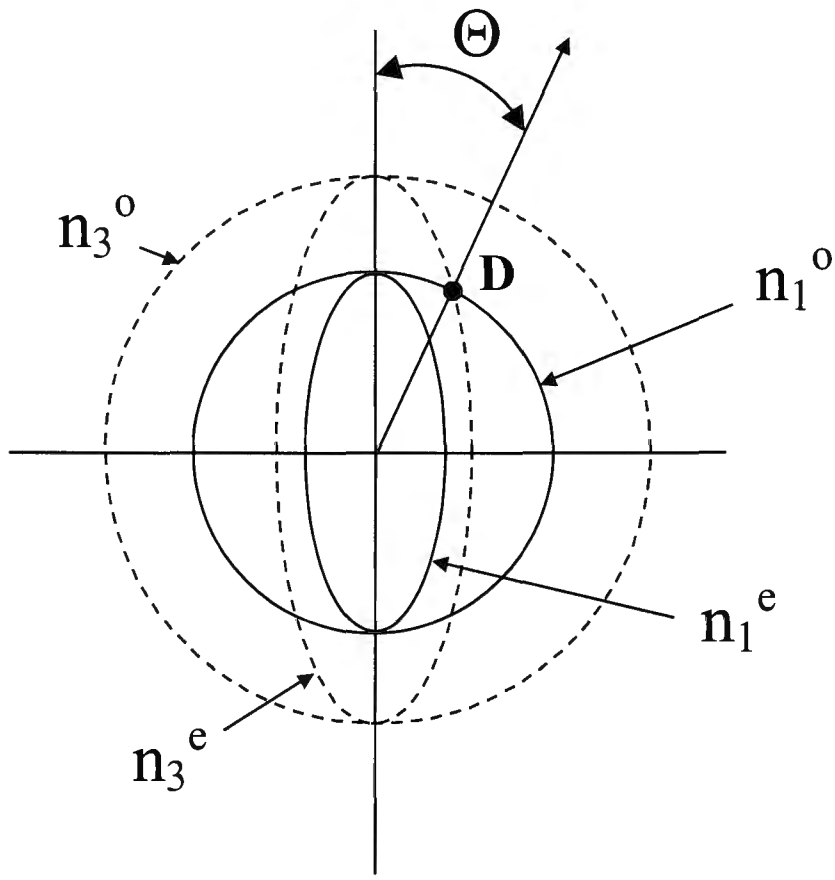

Figure 2.6. Indicatrix showing refractive index behaviour of ordinary and extraordinary waves at two harmonic wavelengths in a negative uniaxial crystal. D indicates the phase matching point for a type 1 interaction. Θ is the phase matching angle, and describes the direction of the input beam with respect to the optic axis (vertical axis) to achieve phase matching.(Koechner[8])

As mentioned, for type 2 phase matching and SHG, the polarisations of the input beams are orthogonal. Therefore, an o-wave and an e-wave at the fundamental wavelength will combine to generate an e-wave at the harmonic wavelength. Again using equation 2.3, this can be stated as:

$$\frac{n_1^o(\lambda) + n_1^e(\lambda, \theta)}{2} = n_3^e(\lambda, \theta) \qquad \textbf{Equation 2.5}$$

In this overview, the discussion of phase matching has been restricted to second harmonic generation in a negative uniaxial crystal. This has been done for the sake of

simplicity although the principles can equally be applied to positive uniaxial crystals and the case of sum frequency generation. While the refractive index surfaces for biaxial crystals are more complex, the phase matching conditions are often able to be reduced to the uniaxial case if phase matching occurs in one of the principal planes of the crystal. Finally, the two types of phase matching described apply when the phase matching direction occurs at some intermediate angle between 0 and 90°. At such angles the harmonic conversion efficiency becomes limited by other crystal properties such as walk off and angular acceptance. These and other properties are described in more detail in the following section.

2.3.2 Properties of nonlinear crystals

A number of crystal and laser properties combine to have an effect on the conversion efficiency of a harmonic generation process. Equation 2.6 shows the small signal approximation dependence of the harmonic power generated for a number of parameters[61]. In this relation, l refers to the crystal length, d_{eff} is the nonlinear coefficient, A is the cross sectional area of the fundamental beam and Δk is as previously defined. The nonlinear coefficient (d_{eff}) may loosely be described as being related to the susceptibility of a crystal to produce harmonic radiation. Its value is dependent upon crystal symmetry, direction of propagation and the interaction type.

$$P(2\omega) \propto l^2 \frac{d_{eff}^2}{A} \frac{\sin^2(\Delta kl/2)}{(\Delta kl/2)^2} \qquad \textbf{Equation 2.6}$$

From equation 2.6, a crystal should primarily have a large nonlinear co-efficient[8] to ensure high conversion efficiency. A small fundamental beam cross section and long crystal length would also be desirable. In practical terms however, other parameters are equally important. A number of parameters may act to dephase the harmonic

generation process by affecting the refractive indices of the crystal creating a phase mismatch and non-zero value of Δk (refer to equations 2.2 and 2.3).

In a birefringent material, angular misalignment, spectral deviation of the fundamental beam and crystal temperature are all parameters that can affect the refractive index. The acceptance bandwidths or tolerances of each of these parameters may be referred to as the amount of deviation permitted to reduce the conversion efficiency by 50% using the sinc^2 function of equation 2.6. Angular tolerance can be exceeded through beam divergence or crystal misalignment. It follows that a crystal exhibiting a large angular acceptance will be less sensitive to these effects. Spectral acceptance is generally less of a problem when dealing with laser beams, which usually have well defined wavelengths. A nonlinear crystal with indexes of refraction susceptible to change with temperature may require active temperature stabilisation to avoid any drift in the conversion efficiency.

Another parameter of practical importance is known as walk off. This is a result of when phase matching is achieved in a birefringent crystal, the direction of power flow of an o and e wave occurs at a small angle. The distance at which the two beams become completely separated is known as the interaction length. The interaction length places a limit on the useful crystal length that may be employed for efficient conversion. Small birefringence within the crystal resulting in a small walk off angle improves the spatial beam profile of the harmonic wave and increases the effective interaction length. This has increased importance when small beam diameters are used.

Aside from introducing practical limits on a crystal as a candidate for use as a harmonic converter, the parameters discussed can be used to advantage. The temperature dependence of LBO for example allows the phase matching angle for some interactions to be "shifted" to occur at 90°. At this phase matching angle, walk off is

eliminated and the angular acceptance is greatly increased. Phase matching under these conditions is often termed non-critical phase matching.

Finally, the damage threshold of the crystal should be considered to ensure the crystal is able to withstand exposure to high levels of intensity. A crystal exhibiting a low damage threshold can prove impractical for long term use despite having other favourable properties for a given interaction. Lithium niobate is an example of a crystal having a large nonlinear coefficient for generating the second harmonic wavelength of an Nd:YAG laser but low damage threshold. The low damage threshold resulted in the crystal not being adopted in widespread use for this interaction.

2.3.3 Crystals

Conversion from the IR to the UV cannot be achieved with a single crystal stage. Typically, the fourth or fifth harmonic wavelength is required of the IR fundamental wave and therefore two or three crystal stages are used. Generation of these higher harmonics permits a number of possible configurations that may be used to produce the desired UV wavelength. With optical losses occurring at each conversion stage in the form of reflection losses and sometimes low conversion efficiencies, optimum choice of wave interaction and crystal type is critical in order to maximise the final output energy.

In the case of the Nd:YAG laser at a wavelength of 1064nm, three crystals are used to produce a fifth harmonic (213nm) wave. One method of achieving this is by producing the second (532nm) and fourth (266nm) harmonics with successive crystal stages before mixing the fundamental with the fourth harmonic at the final crystal stage to produce the fifth harmonic. The fundamental wave for this final interaction is preferably supplied from the unconverted portion of 1064nm light from the initial conversion stage. Alternatively, the second and third (355nm) harmonics may be generated before mixing

the second with the third harmonic to achieve fifth harmonic output. In this instance, the second crystal also consists of a mixing stage; that of the fundamental with the second harmonic.

Crystals employed for SHG of the Nd:YAG laser include CD*A[64], CDA[65],CBO[66], BBO[67], LBO[68], KTP[69], KDP[70], KD*P[71], Lithium Niobate[72], Lithium Iodate[73], CLBO[74], SBBO[75], KBBF[76], RDA[77], and RDP[78]. Commercially, KD*P is the most widely used frequency doubling crystal. Despite low conversion efficiency due to a low d_{eff}, KD*P exhibits low walk off and is able to be temperature stabilised[79]. LBO, KTP and BBO give greater conversion efficiency. LBO is a biaxial nonlinear crystal[68] with a large damage threshold and angular acceptance for SHG of the Nd:YAG laser. It can be temperature tuned to achieve non-critical phase matching[80,81], however the d_{eff} means this crystal is better suited to type 2 SHG[82]. KTP provides a very large d_{eff} for SHG but is also better suited for type 2 interaction[83]. Also, KTP suffers from degradation due to a process known as grey tracking. Considerable effort has recently gone into solving this problem using different fabrication techniques[84-86]. BBO combines high damage threshold with large d_{eff} for type 1 SHG. Difficulties associated with this crystal include large walk off angle and small angular acceptance. The small angular acceptance means that the crystal is susceptible to angular misalignment.

The number of crystals available for generation of the fourth and fifth harmonic wavelengths of the Nd:YAG laser is greatly reduced due to the transmission requirements in the UV. KDP and KD*P have been used for generating the fourth harmonic wavelength with limited success[87]. Observed conversion efficiencies have been low due to a phenomenon known as two photon absorption within the crystal that produces absorbing defects within the material[88]. The biaxial crystal KB5 has also been used for fifth harmonic generation[89]. Fifth harmonic generation using the organic crystal urea was reported by Kato[90]. Organic crystals are limited for practical use due to hygroscopy and extreme softness[62]. In addition to SHG, BBO is also suitable for both

fourth and fifth harmonic generation[91]. As noted for SHG, the conversion efficiency is again limited by large walk off angles and small angular acceptance. Of the available crystals for these interactions however, BBO has proved to be the best choice for practical use.

The problems mentioned for using BBO to generate the fifth harmonic wavelength have restricted the overall conversion efficiency to only a few percent[92]. In 1995 Mori et al[3] reported on the crystal cesium lithium borate (CLBO) for providing improved properties for generating the fourth and fifth harmonic wavelengths of Nd:YAG lasers. A number of properties for these interactions for both BBO and CLBO are shown in Table 2.2.

Harmonic	**Fourth (266nm)**		**Fifth (213nm)**	
Crystal	**CLBO**	**BBO**	**CLBO**	**BBO**
PM Angle (degs)	61.6	47.5	64.8	51.1
d_{eff} (pm/V)	0.84	1.32	0.87	1.26
Walk Off (degs)	1.83	4.80	1.69	5.34
Angular Acceptance (mr-cm)	0.49	0.17	0.42	0.11
Spectral Acceptance (nm-cm)	0.13	0.07	0.16	0.08
Temperature Acceptance (°C-cm)	8.3	4.5	5.1	3.1

Table 2.2. Crystals properties of CLBO and BBO for type 1 fourth and fifth harmonic generation of an Nd:YAG laser[93,94].

As can be seen from the table, BBO has a larger d_{eff} for both interactions. CLBO however, offers almost a factor of 3 lower walk off angle and much larger angular acceptance. The spectral and temperature bandwidths are also larger in CLBO. The favourable properties of CLBO for fifth harmonic generation combine to realise an overall conversion efficiency of 10.4%[93]. This is the highest reported overall conversion efficiency for fifth harmonic generation of an Nd:YAG laser. Unfortunately, CLBO suffered from hygroscopy after just a few days of operation in a humid environment[95].

This problem was overcome however, by maintaining the crystal at an elevated temperature of more than 140°C [96,97].

Generation into the UV with Ti:sapphire lasers is achieved with the fourth harmonic wavelength. This can be accomplished with two crystal stages incorporating successive frequency doubling. Alternatively, as for fifth harmonic generation of the Nd:YAG laser, three crystals can be used. In this case, the first crystal generates the second harmonic. The next stage mixes the fundamental and second harmonic wavelengths to generate the third harmonic wavelength. Finally, the fundamental is mixed with the third harmonic to generate the fourth harmonic wavelength. Interestingly, a three crystal scheme uses the fundamental wavelength in each stage.

BBO, LBO and Lithium Iodate represent the most efficient choices for SHG of Ti:sapphire lasers[98]. KDP[99] and CLBO[100] have also been investigated for this interaction. Despite a large d_{eff}, Lithium Iodate has a very large walk off angle which limits its potential for use if higher harmonics are required. BBO too, is subject to a large walk off angle and has a d_{eff} approximately half that of Lithium Iodate. A study comparing the SHG conversion efficiency using LBO and Lithium Iodate found that, despite having a lower d_{eff} value than Lithium Iodate, LBO was able to generate SHG radiation with the greatest efficiency[101]. This was attributed to the small walk off angle and large angular acceptance of LBO for this interaction. Temperature tuned phase matching has also been demonstrated in LBO over a fundamental wavelength range of 740 – 900nm[102].

Fourth harmonic wavelengths below 204.8nm cannot be generated with a two crystal scheme[103,104]. Therefore, if shorter wavelengths are required, a three crystal scheme must be used. Wavelengths in the range 190 – 205nm have been produced with this type of scheme by a number of investigators[99,105-108]. Recently, CLBO has also been used in various frequency mixing arrangements to achieve wavelengths in the deep

UV. This has required however, mixing wavelengths from more than one laser source[109-111]. Harmonic generation in this wavelength region has generally been applied to ultrashort pulse lasers and consequently pulse energies are usually in the micro-joule range.

The 204.8nm wavelength limit for frequency doubling mentioned above can only be provided by BBO. The frequency doubling cut off wavelength for other available crystals such as LBO (277nm), CLBO (236.7nm) and KDP (258.5nm) does not extend into this range. This lower wavelength limit in BBO represents room temperature operation. It has been demonstrated that cooling the crystal to 89K can extend the frequency doubled wavelength to 203.1nm[112].

One problem with using BBO for fourth harmonic generation of Ti:sapphire lasers is that as the lower wavelength limit is approached, the d_{eff} tends towards zero. Increasing the wavelength to yield greater conversion efficiency by increasing the d_{eff} also increases the requirement of the fundamental wavelength. For example, fourth harmonic generation at a wavelength of 220nm requires a fundamental wavelength of 880nm, which is moving away from the optimal bandwidth of operation for Ti:sapphire lasers.

2.4 Mechanisms of Corneal Ablation

A number of laser devices have been shown to be suitable for applications in ophthalmology that require tissue ablation. Desirable properties for ablation include high precision and control over the amount of tissue removed in conjunction with low levels of damage to surrounding tissue. In particular for corneal ablation, the excimer gas laser has been most successful. In recent years, ultrashort pulse lasers have also been shown to be suitable for corneal ablation. The suitability of each of these laser

types has led to a number of investigations to gain an understanding of the mechanism responsible for the observed effects.

Two parameters play a critical role in achieving ablation in a material. First, the wavelength of the radiation affects the ablation mechanism due to varying absorption within the material. This is evidenced by the differing nature and amount of any co-lateral damage observed around the ablation site using wavelengths in the UV, visible and IR. Secondly, the power density of the laser pulse, which relates to the fluence and the time dependence of the applied laser energy, governs the rate at which energy is absorbed. This is seen in the efficacy of using pulsed lasers to ablate material rather than continuous or very long pulse systems.

2.4.1 Corneal Absorption and Ablation in the UV.

An early model of the ablation mechanism was developed based on the exponential absorption of the laser radiation through corneal tissue[113]. Using a form of the Beer-Lambert law of attenuation, the ablation depth achieved with each pulse was given by the equation:

$$d = \frac{1}{\alpha} \ln \left(\frac{F}{F_T} \right) \qquad \textbf{Equation 2.7}$$

where d (cm) is the ablation depth per pulse, α (cm^{-1}) is the absorption coefficient for corneal tissue, F (mJ/cm^2) is the laser fluence of the impinging pulse and F_T (mJ/cm^2) is the threshold fluence for ablation.

Equation 2.7 suggests that a log-linear plot of ablation depth and fluence should yield a linear relationship with a gradient equal to $1/\alpha$. Experimental results revealed that the linear relationship between ablation depth and the logarithm of fluence is only valid over a limited range of fluence values[114-116] (Refer also to Figure 2.8 on page 45).

Moreover, in this range the gradient was found to disagree with that predicted by the equation based on previously published values of the absorption coefficient.

An early study by Puliafito *et al.*[117] measured the absorption coefficient of bovine cornea at the excimer laser wavelengths of 193 and 248nm. Measurements were obtained by monitoring the transmission through corneal sections of 32μm thickness. The calculated value of the absorption coefficient was 2700 and 210cm^{-1} for 193 and 248nm respectively.

Lembares *et al*[118] measured the corneal absorption of ultraviolet wavelengths between 190 and 350nm in 23 porcine corneal samples and 11 human corneal samples with a dual-beam UV-visible-IR spectrophotometer. Absorbance as a function of wavelength is shown in figure 2.7 for human cornea between the wavelengths of 190 and 260nm. The inset of figure 2.7 shows the full spectrum measured between 190 and 350nm. From the results, Lembares identified three distinct regions of interest between 190 and 260nm with boundaries at 220 and 240nm. The three regions are comprised of a weak absorbing segment between 260 and 240nm, a steeply increasing segment between 240 and 220nm followed by a high absorption segment for wavelengths below 220nm. For human cornea, a value for the absorption coefficient was given as 2340 and 2316cm^{-1} for 193 and 213nm respectively. In the high absorption segment (190 to 220nm) the absorption curve exhibits a gradient close to zero. Therefore, in this wavelength range, maximal local absorption would be expected to be observed rather than any extended tissue effects through the cornea.

The results obtained by Lembares were in agreement with those of Puliafito to within 15% for the 193nm wavelength. However, using these values to perform theoretical calculations of the ablation rate using Beer's law (equation 2.7) produces an etch rate of ~5μm/pulse for a laser fluence of 170mJ/cm^2 and threshold fluence of 50mJ/cm^2. The threshold fluence value is typical of that determined by other investigators ablating

corneal tissue[117,119-121]. This value of ablation rate is an order of magnitude larger than that determined experimentally for similar fluence values.

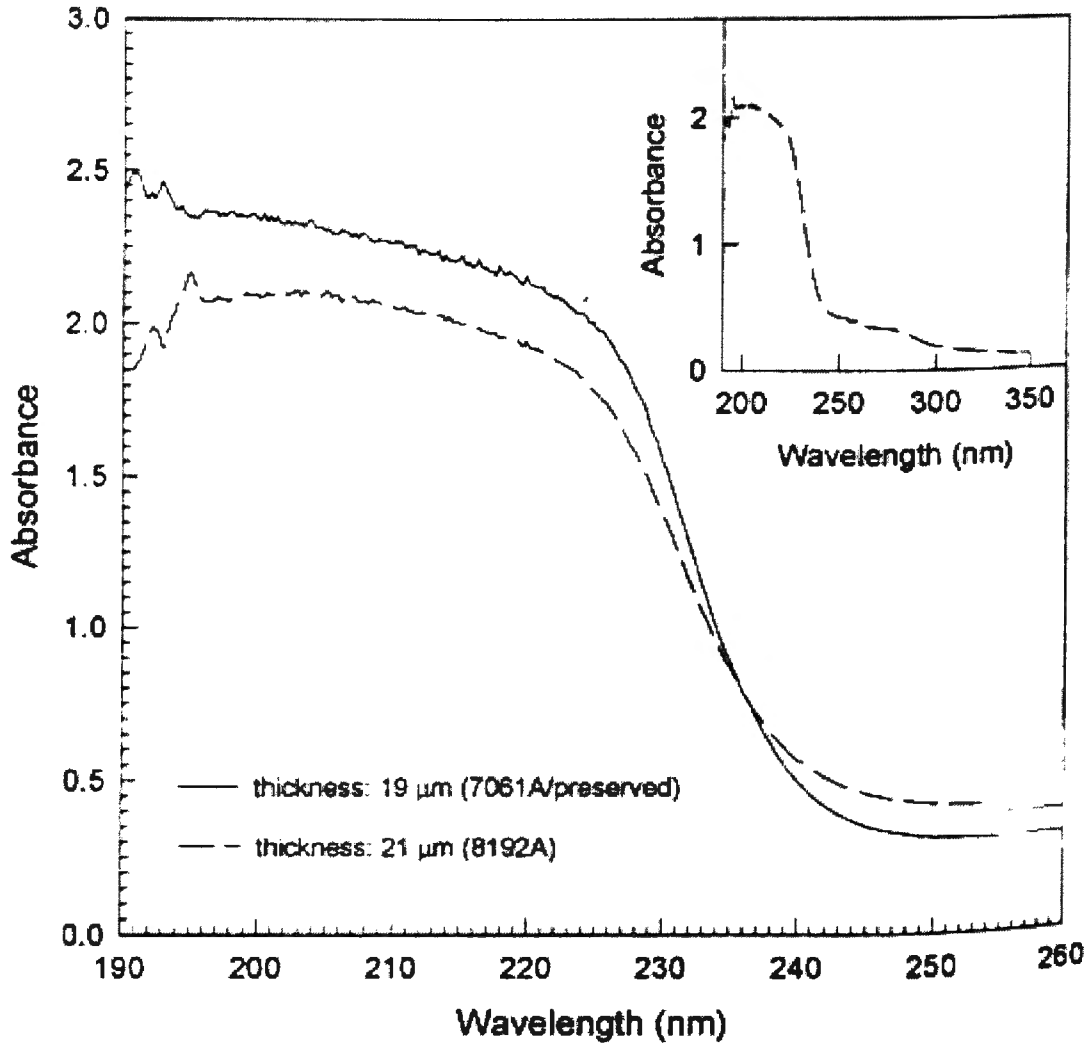

Figure 2.7 The dependence of absorbance on the wavelength for two human corneal samples between 190 and 260nm. The dependence of absorbance on the wavelength for one human corneal sample between 190 and 350nm. (inset) (Lembares[118])

This discrepancy was addressed in a study by Pettit and Ediger[122] who investigated the absorption coefficient in corneal tissue at the two discrete wavelengths of 193 and 213nm. The technique employed Fresnel reflection theory to calculate the complex refractive index of corneal tissue. The study produced results for the absorption coefficient that were approximately an order of magnitude larger (39,900cm^{-1} at 193nm

and 21,400cm^{-1} at 213nm) than the published values of Lembares and Puliafito. It was postulated that the previous low values for the absorption coefficient were a result of transmission errors occurring due to the difficulties of consistently sectioning tissue samples to tens of microns in thickness. Also, the values provided a good approximation of the ablation rate when used in conjunction with Beer's law against the experimental data. Further work by Yablon *et al*[123] established an absorption coefficient at 193nm in bovine tissue of 19,400cm^{-1}. This value is of the same order as the results obtained by Pettit and Ediger. Absorption coefficient results for the studies discussed are shown in tabular form in table 2.3.

	Corneal absorption coefficient α (cm^{-1})		
Investigator	**193nm**	**213nm**	**Tissue**
Puliafito[117] 1985	2700		Human, Bovine
Pettit[122] 1996	39,900	21,400	Bovine
Lembares[118] 1997	2340	2316	Human
Yablon[123] 1999	19,400		Bovine

Table 2.3. Corneal absorption coefficient results for 193 and 213nm of various investigators.

Ablation with UV wavelengths produced from excimer lasers is characterised by an absence of charring and minimal collateral tissue damage adjacent to the ablation site. The low level of charring or heating effects led to the belief that ablation occurred through a combination of photochemical and photothermal processes. At UV wavelengths the photochemical interaction is thought to dominate. This process was given the term ablative photodecomposition[113]. Early work characterised the process in terms of the threshold and rate of ablation for various polymer materials and species of corneal tissue[119,124,125]. This involved finding the amount of energy required to remove a known volume of tissue for a range of fluence values.

The photochemical interaction is based on the cleavage of intra-molecular bonds within the stroma. Evidence that this interaction is a photochemical one lies with the high photon energy of 6.4eV for the excimer laser wavelength of 193nm. Similarly, the photon energy of the 213nm wavelength is 5.8eV. Both these energies are well above the typical molecular bond energy (~3.5eV) found in the cornea[117]. In addition to this, it has been found that the ablation threshold is independent of the laser pulse rate at the 193nm wavelength[119]. This suggests the absence of any thermal influence in the interaction. If a significant thermal component were present the ablation rate would vary with pulse rate, as there would be residual heating of the tissue from previous laser pulses to the next. This point was quantified by Krueger *et al* [119] who investigated the effect on the ablation threshold for excimer laser wavelengths of 193, 248, 308 and 351nm. The fluence threshold for ablation was obtained for each of these wavelengths and at different pulse rates. It was found that with increasing wavelength the ablation threshold increased for a fixed pulse rate. A plausible explanation for this is the increased transmittance of the cornea at longer wavelengths. However, as the pulse rate was increased the threshold at the longer wavelengths was lowered. This suggests the presence of a thermal component in the interaction due to the increased pulse rate, but only at the longer wavelengths.

The model of ablative photodecomposition involves three stages[113]. Initially, absorption of the incoming laser radiation takes place, which is then followed by the breaking of bonds within the volume of tissue exposed to the radiation. Finally, ablation occurs with ejection of tissue fragments due to excitation from excess photon energy and an increase in the volume of the fragments. Work by Sutcliffe and Srinivasan[126] identified two problems with this model which also incorporated equation 2.7. Firstly, that the onset of ablation occurs only after the laser pulse has completely traversed the material. Secondly, that the equation ignores the time dependence of the pulse and the rate at which energy is delivered to the tissue. The first point is illustrated in photoacoustic studies that indicate the onset of ablation occurs within 4-6ns of the start

of the laser pulse[127,128]. The second point is more intuitive if a continuous laser source operating at a similar value of power density is considered. Also, studies involving shorter pulse durations have demonstrated a reduction of the threshold fluence for ablation[129].

The problems identified by Sutcliffe and Srinivasan led to the development of a dynamic model that incorporated the time dependence of the laser pulse and defined more rigidly the conditions for ablation. The model proposed that at low levels of absorbed photon density, any broken bonds within the material would simply recombine through relaxation processes and no ablation would occur. However, when a critical density of broken bonds per unit time is achieved, recombination reaches a steady state and further absorption results in the fragmentation process. This idea was further illustrated through the observation of an increase in the ablation rate of a polymer in the pulse duration range of 40 to 100ns, using an excimer wavelength of 248nm [130].

Another important aspect in gaining an understanding of the ablation process can be obtained by examining the ejected products from the bulk material[131-133] and the effects, if any, of the formation of shock waves following the incidence of a laser pulse. Also, by examining these phenomena, an idea of the time frame over which ablation occurs can be found. One method of doing this is through time resolved imaging of the ablation plume. This technique involves illuminating the ablation plume across the same plane as the material surface and taking a series of photographs to observe the plume formation[134-138]. The results showed that the ablation plume first appears after approximately 60ns and material is observed to be ejected for up to 20μs, roughly 1000 times the duration of the impinging laser pulse. This method also revealed that the velocity of the ejected products occurred at super sonic speeds (>600ms^{-1}) and deceleration is rapid, slowing to 10's of metres per second in just a few microseconds. With such high ejection velocities, a recoil effect, which manifests as a surface wave on

the material can be expected. The amplitude of this surface wave could have undesirable repercussions with the potential to tear or damage underlying layers of the material[138].

2.4.2 Ablation in the visible-near IR.

For wavelengths in the visible to near IR (up to 1300nm), corneal and other ocular tissue is essentially transparent with linear absorption reaching a minimum in this region. Therefore, the mechanism of tissue removal at these wavelengths must involve a nonlinear process of absorption. For incident irradiance levels of extremely high values (GW/cm^2) the material can become strongly absorbing if free electrons can be produced with a large enough density to form a plasma. When this occurs the structure of the material is altered irreversibly[139] in a process known as optical breakdown. The threshold for optical breakdown is generally achieved by focusing the incident laser pulse into a small volume, while the value of this threshold in a given material is also a function of pulse duration. Since the optical breakdown threshold occurs in a focal volume, material disruption is therefore able to take place beneath the surface of transparent media. The use of absorptive wavelengths makes possible surface ablation only. This property has been utilised for some time in ophthalmic applications such as performing lens capsulotomies.

The mechanism for optical breakdown can be regarded as a result of two main processes[140]. Electron ionisation creating a plasma within the material, followed by a rapid expansion of the plasma through heating causing both shock and acoustic waves that mechanically disrupt adjacent tissue causing cavitation[141]. For a perfectly transparent material, bound electrons require more energy to become ionised than is available in a photon from the incident radiation. However, if a few free electrons are present in a material then these electrons can gain energy from the laser pulse and upon colliding with a bound electron can impart enough energy to ionise this second

electron. This process then repeats at an exponential rate in what is called avalanche ionisation. Alternatively, free electrons can be directly produced from a bound state by multiphoton absorption. The process of electron ionisation and the subsequent plasma formation have important implications on the ablative behaviour for pulses of varying duration.

At longer pulse durations from the nanosecond to the picosecond regime, multiphoton absorption is less likely to occur and plasma formation is largely due to avalanche ionisation. Since this process requires the presence of free electrons to seed further ionisation the occurrence of optical breakdown is a statistical function[139]. Within this duration range the breakdown threshold is observed to have a square root dependence on the pulse duration[142-144]. For shorter pulses reaching into the femtosecond regime, initial electron ionisation is almost exclusively due to multiphoton absorption. Therefore, the optical breakdown threshold can be more sharply defined[139,145], although reducing the pulse duration below a few hundred femtoseconds produces no further reduction in the ablation threshold fluence[144].

The last decade has seen a number of investigations conducted into performing intra-stromal ablation based on the optical breakdown process. Advantages of this were thought to include a reduction of the energy requirement for ablation through the use of a shorter duration pulse and higher pulse repetition rate. This could lead to a reduction of the depth observed for co-lateral damage that was shown to vary as the cube root of the pulse energy used[146,147]. Initially, results from intrastromal ablation were varied. More recent efforts have refined the technique to include the removal of a lenticule to affect a change in the refractive power of the cornea[141,148]. The lenticule is created intrastromally and removed in a fashion similar to keratomileusis.

An optimal pulse repetition rate was identified as being between 1 to 5 kHz depending on the energy used. A repetition rate in this range allows for the stabilisation of the size

of the cavitation bubble resulting from a pulse before the next pulse is delivered[149]. This requirement is a result of the precise nature of the positioning of the laser pulses in creating a layer within the stroma[150].

2.4.3 Ablation in the mid-IR

The mid-IR spectrum extends for wavelengths of approximately 1.3μm to over 3μm. The 3μm wavelength represents an absorption peak for water. Compared to the UV, the absorption coefficient of water is five orders of magnitude larger[151] at 3μm. Ablation in this wavelength region occurs via photothermal interactions.

Ablation is initiated through vaporisation of water within the tissue substrate. As the water absorbs the incoming photons, the temperature increases which in turn leads to an expansion of the material. The subsequent increase in pressure resulting from rapid expansion culminates in an explosive ejection of the material fragments. This type of ablation has also been referred to as thermal decomposition[152].

The actual nature of any observed thermal effects are dependent upon a number of other laser parameters such as the pulse duration, repetition rate and fluence. Recent work using a laser wavelength of 2.94μm has postulated a different thermal ablation mechanism; primarily based upon the pulse duration but also combined with the use of an optimal fluence value. This mechanism has been termed photospallation[153,154]. These studies found that by using pulse durations in the nanosecond regime, ablation could be achieved with a collateral damage zone similar to that observed for ablation with UV pulses from excimer lasers. Ablation using pulse durations of several microseconds produced damage zones of unacceptably large extent for corneal ablation.

In summary, for each wavelength domain a different mechanism of ablation is evident. In the UV, the model is that of a photochemical process directly breaking stromal bonds while in the visible to near IR, plasma mediated ablation is prevalent. Finally, as the wavelength is increased into the mid IR, ablation is achieved by either photothermal means or photospallation.

2.4.4 Methods of Ablation Measurements

To remove corneal tissue in a predictable fashion a detailed knowledge of the amount of tissue removed with each laser pulse is required. Therefore, a need exists to be able to accurately measure the ablation behaviour of a laser beam. The parameters of importance in quantifying this behaviour are the laser fluence used and the resulting ablation rate or etch depth. Accurate quantification can prove a difficult task, taking into account the nature of the tissue involved and the depths required to be measured, which are of the order of tens of microns.

Measurement of the laser fluence also can be prone to large errors. While laser pulse energy can generally be measured with high precision and accuracy, the beam area often cannot. Focusing of the beam with a lens requires an estimation of the resulting laser spot size, which is a function of the lens focal distance, initial beam diameter and the energy distribution of the beam. If lens focusing is not required, an aperture or mask may be put into the beam to produce a desired ablation geometry to aid in measurement, such as a slit. An advantage of using an aperture is that the central portion of the beam profile can be selected, giving a more even energy distribution.

The ablation rate is defined as the etch depth per pulse and can be calculated by either counting the number of pulses required to ablate a known thickness of material or by measuring the depth of ablation achieved following exposure to a preset number of

pulses. By repeating this process for a range of fluence values, the variation of ablation rate with laser fluence can be obtained.

The ablation of a known thickness of corneal tissue carries the requirement of initially measuring the sample thickness. For corneal tissue this can be achieved by using a slit lamp or ultrasonic pachymetry[125,155-158]. The number of pulses required to perforate the cornea can then be counted and the ablation rate calculated. Corneal perforation is generally detected through the observance of aqueous expression from the target area. The accuracy of this technique is dependent upon the corneal perforation occurring over the same thickness of tissue obtained from the pachymetric measurement.

Ablations involving corneal tissue from enucleated eyes should be analysed immediately following exposure to obtain best results. This problem can be overcome somewhat by a chemical fixing process for histological analysis. Preparation of ablated tissue samples in this manner allows the samples to be examined using light or electron microscopy[115,120,129,159-161]. With this method the cut depth is expressed as a percentage of the total corneal thickness. Histologic methods also provide for additional data to be obtained from a given ablation. Thermal damage zones adjacent to the cut region can be assessed as well as the ultrastructural quality of the ablation zone. A disadvantage of histologic methods is the potential for further tissue deformation, such as shrinkage, during the fixing process and the introduction of processing artefacts[162]. Also, the method does not account for any hydration issues related to the tissue in question. This is also the case for the perforation technique discussed above.

Most techniques of analysis using microscopy employ a chemical fixing process. A study by Bachmann *et al*[163] proposed an alternative preparation to chemical fixing. This involved making a silicon mould or cast of the ablated surface. The nontoxic material was shown to be flexible and able to maintain shape once the cast was set. This required approximately 30 minutes at room temperature but could be reduced to 5

minutes if placed in a heated environment of 37°C. Once prepared, the moulds were sectioned and the depth of ablation was determined using light microscopy. The moulding of the ablation was accurate to 0.25μm and the material was able to be measured repeatably and stored for later use. A possible disadvantage of this method is that the casts are unable to provide any additional data in terms of thermal damage and cellular information.

A study by Dougherty *et al*[164] aimed to address the issue of corneal hydration and the effect this has on the ablation rate. The study identified that ablated material comprised both a dry component and a hydrated component of tissue. Also, that the amount of dry component material removed was the dominant factor in minimising the error in the final refractive outcome for a given treatment. Dry component ablation rate was measured with units of $\mu g/cm^2$/pulse. This was obtained by dividing the dry component mass removed by the number of pulses and the area of the ablation. To calculate the dry component mass removed, knowledge of the hydration of the corneal sample was required. Hydration was determined for each sample using a published value for the density of dry corneal tissue and the density of the sample. An assumption was made that the sample volume remained constant when water was added to the tissue. The study concluded that performing ablations with superhydrated tissue resulted in undercorrection while ablations with dehydrated tissue precipitated overcorrection. Therefore, ablations performed at a level of physiological hydration produce the best results. An advantage of this method was that a depth measurement of the tissue was not required to obtain the ablation rate. It did however, require a great deal of care in measurement of tissue mass and ensuring that sample hydration was maintained during laser exposure.

An in vivo method for determining ablation rate was undertaken by Huebscher *et al*[165] and involved the use of Scheimpflug videography. This technique used an image of the corneal surface to calculate the radius of curvature. The refractive power of the anterior corneal surface was then determined using the relation:

$$D = (1.337 - 1)/R \qquad \textbf{Equation 2.8}$$

where R is the radius of curvature in metres, D gives the refractive power in dioptres and the constant 1.337 is the approximate refractive index of the corneal tear film. By finding the radius of curvature both pre- and post-operatively, the change in dioptric power was obtained. Next, the central depth of the ablation was evaluated using the obtained change in dioptric power. Finally, the ablation rate was calculated by dividing the central depth by the number of laser pulses applied to the central region.

One limitation of this method is the required assumption which is made for the value of the refractive index of the cornea. Other work indicates that a slightly larger value of refractive index could be used for the stroma[166]. Also, the level of corneal hydration during treatment and the effect this may have on the final curvature of the corneal surface needs to be taken into account.

Often, initial laser ablation trials are carried out on a synthetic polymer such as PMMA. PMMA offers the advantage of having similar ablation characteristics to corneal tissue while being easier to work with. It can also be stored for measurement at another time. Owing to the different nature and ease of use of PMMA compared with corneal tissue, different methods for measuring the ablation depth have been applied to this material.

Perhaps the simplest method of measuring ablation depth of PMMA after exposure to a preset number of pulses uses a light microscope to focus on the top and bottom of the ablated region[116,167]. By noting the distance the focal point of the microscope objective

lens is shifted in moving from the top to the bottom of the cut, the depth of ablation is obtained. The resolution of the depth measurement using this method is determined by the power or focal length of the microscope objective used.

Caughey *et al*[167] used a diamond tipped stylus to take a contour of the ablated zone. This was applied to cuts of several microns depth. For shallower cuts, an optical profilometer device was used. This interference based device is capable of resolution on the order of an Angstrom and was applied to cuts exhibiting depths of less than 2 microns. These shallow cuts were formed from exposure to only one or two laser pulses.

It is difficult to quantify the efficacy of one method of measurement over another. A balance is required between the practical simplicity of the method and the accuracy of the results. The aim of any ablation rate study is to characterise the ablation rate behaviour with incident laser fluence. For corneal tissue, the simplest method appears to be the perforation method described. This only serves to produce an ablation rate for a given fluence for a single depth or pulse number. A more comprehensive approach to obtaining the ablation rate may be to first plot ablation depth against pulse number for a given fluence. The gradient of this plot then gives the ablation rate for that fluence value. By repeating this process for a range of fluence values, the characteristic curve of ablation rate versus fluence can be constructed. This does however, require a greatly increased number of cuts and depth measurements. Also, an accurate and reliable method of depth measurement is needed. For corneal tissue, this can prove problematic. From the methods described in this section, this approach is probably best suited to measurements of PMMA.

2.5 Ablation rate results in cornea and polymer material

2.5.1 Ablation of corneal tissue

As discussed in the previous section, the early model of ablation relied largely upon the Beer-Lambert law of attenuation. At the 193nm excimer laser wavelength, numerous investigations have focused on characterising the ablation rate behaviour with laser fluence in corneal tissue[115,116,125,157,158,161]. The results of these investigations are displayed in Figure 2.8. and show an adherence to the Beer-Lambert law (linear region) over a limited range of fluence values extending from approximately 150 to 700mJ/cm^2. For fluence values larger than 700mJ/cm^2, no significant increase in the ablation rate was observed. For lower fluence values (< 150mJ/cm^2) the gradient of the curve was also observed to taper off. Therefore, the overall shape of the ablation rate curve was described as sigmoidal.

A linear fit to the data from all investigators was applied for the experimental points within the range of fluence values between 150 and 700mJ/cm^2. This linear trend line is also shown in Figure 2.8. The dashed line shown in the figure is a theoretical ablation rate curve obtained using the Beer-Lambert law incorporating the measured value of the corneal absorption coefficient[117] of 2700cm^{-1} at a wavelength of 193nm. The discrepancy between the gradient of this curve and that of the linear trend line can easily be seen. The gradient of the linear trend line suggests an absorption coefficient of 17,650cm^{-1} for corneal tissue when calculated using the Beer-Lambert law. This value is of the same order as the value measured directly by Pettit[122] and Yablon[123].

Fluence values of clinical relevance encompass a range from 80 to 300mJ/cm^2. In particular, a fluence range of 160 to 250mJ/cm^2 is predominantly used in commercial excimer lasers for refractive surgery (Table 2.4). From the linear fit of the collective data in Figure 2.8, a nominal ablation rate of 0.16 to 0.42μm/pulse is predicted for this range of fluence values.

The most efficient fluence for ablation has also been found to occur within the range of fluence values used commercially for excimer lasers. Ablation efficiency is defined as the mass of material removed per unit of input laser energy[121]. Krueger and Trokel[125] quantified the most efficient fluence for ablation at the 193nm wavelength using bovine corneas. The study first obtained the ablation rate over a wide range of fluence values. The most efficient fluence was found by recording the amount of radiant exposure required to remove a depth of 100μm of tissue. The study revealed the most efficient fluence for ablation was approximately 200mJ/cm^2.

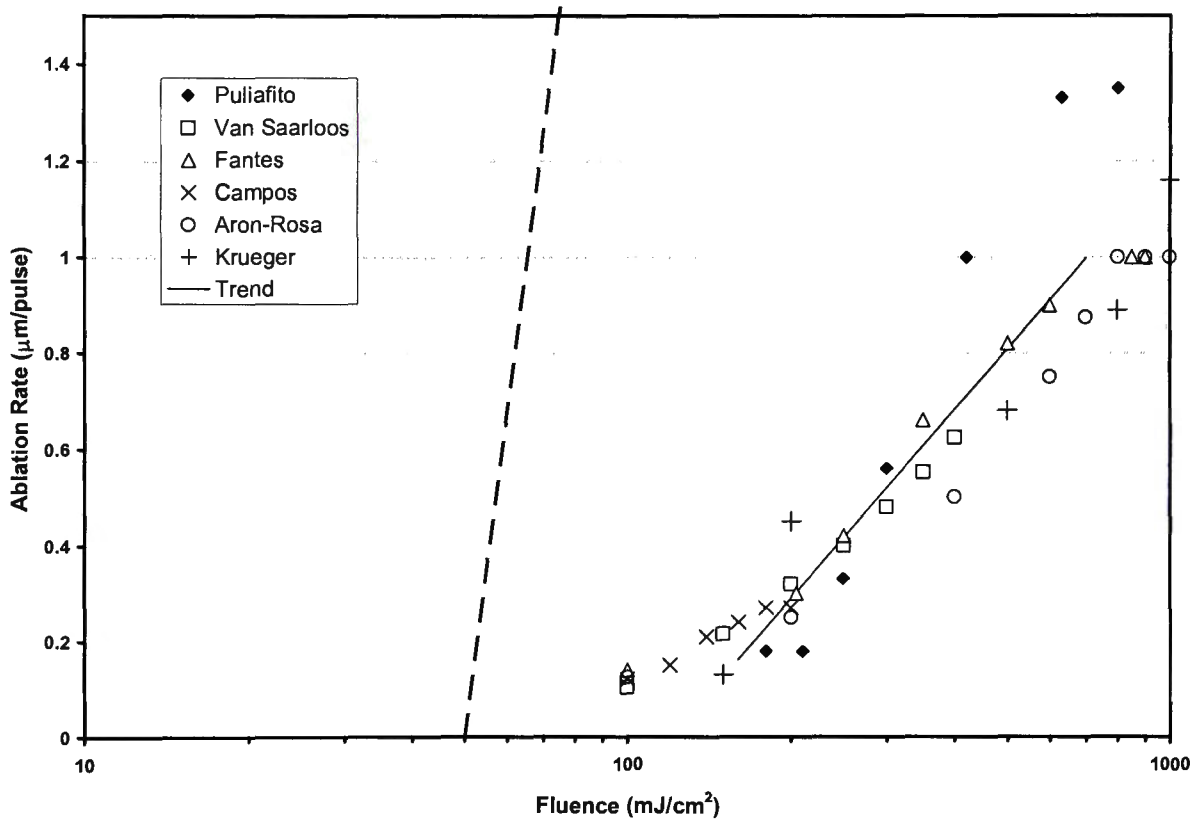

Figure 2.8. Semi-logarithmic plot of ablation rate results in corneal tissue using 193nm wavelength by various investigators.[115,116,125,157,158,161] The dashed line shows the ablation behaviour obtained using the Beer-Lambert law with the early measured value of the absorption coefficient (2700cm^{-1}).

Laser	Fluence (mJ/cm^2)
Bausch & Lomb Technolas 217	120
LadarVision	180-240
LaserSight LSX	80-100
Meditec Mel70	200
Nidek EC5000	130
Schwind Esiris	250-300
Visx Star	160
Wavelight Allegretto	195

Table 2.4. List of fluence values used by various commercial excimer based (193nm) refractive laser systems.

In contrast to the volume of literature available involving ablation at the 193nm wavelength, there are very few publications that relate ablation rate with the solid state laser wavelength of 213nm. Only Shen[156] and Caughey[167] have investigated the ablation rate of corneal tissue for multiple points of the laser fluence. The ablation rate results of these investigations were not consistent with each other. Caughey obtained ablation rates of 0.4, 0.6 and 0.9μm/pulse for fluence values of 200, 420 and 640mJ/cm^2 respectively. The authors did note that these values should be accepted with caution, as the results were estimates from sectioned specimens used for histology. Results of Shen are shown in Table 2.5 below. Another study involving corneal tissue that obtained the ablation rate for a single fluence value was performed by Gailitis *et al*[155] (0.23μm/pulse at 1300mJ/cm^2). For the large value of fluence used, the ablation rate appears to be below the expected value.

Fluence (mJ/cm^2)	Ablation rate (μm/pulse)
98	0.11
188	0.34
304	0.96
353	1.18
507	1.49

Table 2.5. Ablation rate results for corneal tissue using a laser wavelength of 213nm. Data obtained from Shen et al.[156]

2.5.2 Ablation of polymer material

As discussed in section 2.4.4, PMMA provides a convenient working sample when characterising the ablation behaviour of an UV laser. For the excimer laser (193nm), PMMA was identified as providing a useful indicator to the ablation of corneal tissue due to the similar chromophores found in cornea and PMMA. Also, the polymer, PHEMA was investigated for ablation rate behaviour in this project. PHEMA is a hydrophilic polymer that forms a hydrogel when hydrated and has been used in a number of biomedical applications in ophthalmology[168]. The ability of PHEMA to absorb water creates the potential to investigate the affect hydration has on ablation rate. This could provide insight for ablation of corneal tissue as examining such affects using corneas is much more difficult.

The basic chemical structure of both PMMA and PHEMA is shown in Figure 2.9. Also, some selected bond energies are given in Table 2.6 along with the optical wavelengths for photons corresponding to the relevant bond energy. This reveals that the single carbon-oxygen or carbon-carbon bonds would require a laser wavelength of less than 344nm to induce a bond breaking event in a material containing these bonds. In terms of bond energy therefore, the excimer (193nm) and solid state laser (213nm) wavelengths have more than sufficient photon energy to achieve this.

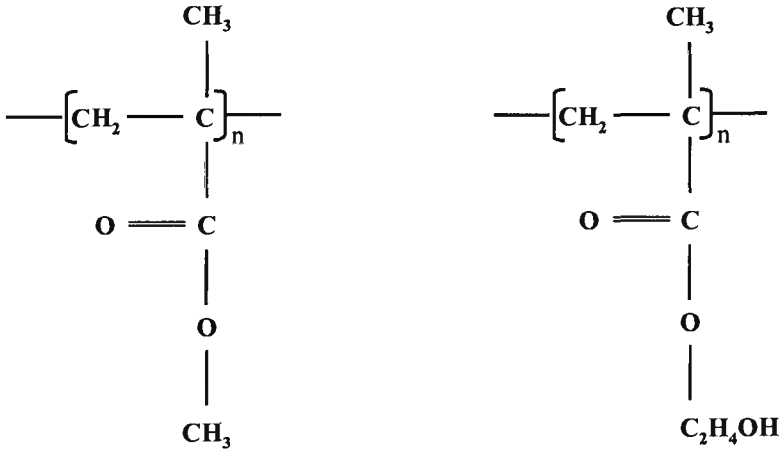

PMMA PHEMA

Figure 2.9. Chemical structure of PMMA and PHEMA[169,170].

Bond	Energy (eV)	Wavelength (nm)
C = O	7.1	175
C – O	3.6	344
C – C	3.6	344

Table. 2.6. Bond energies found in PMMA. Wavelength values for photons carrying an equivalent amount of energy are also shown. (Niemz[152])

The results of several investigations into the ablation behaviour of PMMA using a wavelength of 193nm are shown in Figure 2.10. Fuxbruner *et al.*[171] determined the linear region of the semi-logarithmic plot of etch depth occurred for a fluence range of 100-200mJ/cm^2. As mentioned above in section 2.5.1 this fluence range falls within that employed clinically. The ablation rates obtained in this region varied from 0.21 to 0.31μm/pulse (Fuxbruner), 0.09 to 0.27μm/pulse (Srinivasan *et al*[172]) and 0.02 to 0.18μm/pulse (van Saarloos *et al*[173]). The ablation rates obtained by Fuxbruner and Srinivasan at a fluence of 200mJ/cm^2 agree to within 6% of the ablation rate for corneal tissue using the combined data of figure 2.8. From the slope of the ablation rate data, predicted absorption coefficients for PMMA were ~65,000cm^{-1} (Fuxbruner), ~38,000cm^{-1} (Srinivasan) and ~44,000cm^{-1} (van Saarloos). As was the case for corneal tissue ablation, the predicted absorption coefficients for PMMA were an order of magnitude larger than the measured values available from the literature[174]. For PMMA at a wavelength of 193nm, a local minimum is observed in the absorption spectrum having a value of ~3000cm^{-1}.

The relative lack of consistency in the slopes of the ablation rate data observed from Figure 2.10 compared with the combined data for cornea from Figure 2.8 suggests that PMMA may not be an accurate indicator for modelling the ablation behaviour in cornea. Although the ablation rates of Fuxbruner and Srinivasan had a similar value for a

fluence of 200mJ/cm^2, the rates at other values of fluence do not continue to correlate. A possible explanation for the discrepancy observed in the respective curve gradients might be attributed to the amount of impurities introduced into the polymer at the manufacturing stage[173].

Results of PMMA ablation rates using the 213nm wavelength are shown in Figure 2.11. Unlike the results shown in Figure 2.10, these results displayed far greater consistency in terms of both gradient values and ablation rates. The combined data of this plot showed the ablation rate varied from 0.24 to 0.41μm/pulse for fluence values of 160 and 250mJ/cm^2 respectively. It is difficult to make a meaningful comparison for this wavelength between the ablation rates of PMMA and cornea due to the lack of data available for corneal tissue. Comparison with data at the 193nm wavelength for PMMA showed agreement with the ablation rate to within 10% for a fluence of 200mJ/cm^2. The slope of the data at 213nm, also was within the range observed for 193nm from the investigators featured.

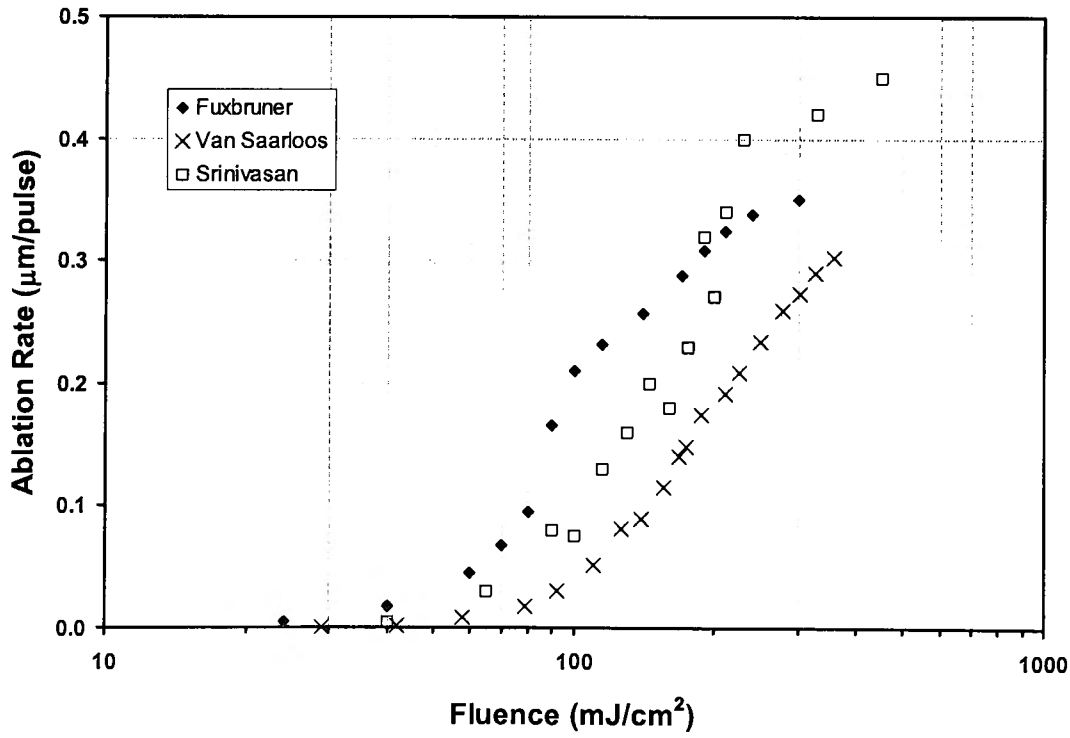

Figure 2.10. Semi-logarithmic plot of ablation rate results in PMMA using 193nm wavelength by various investigators.[171-173]

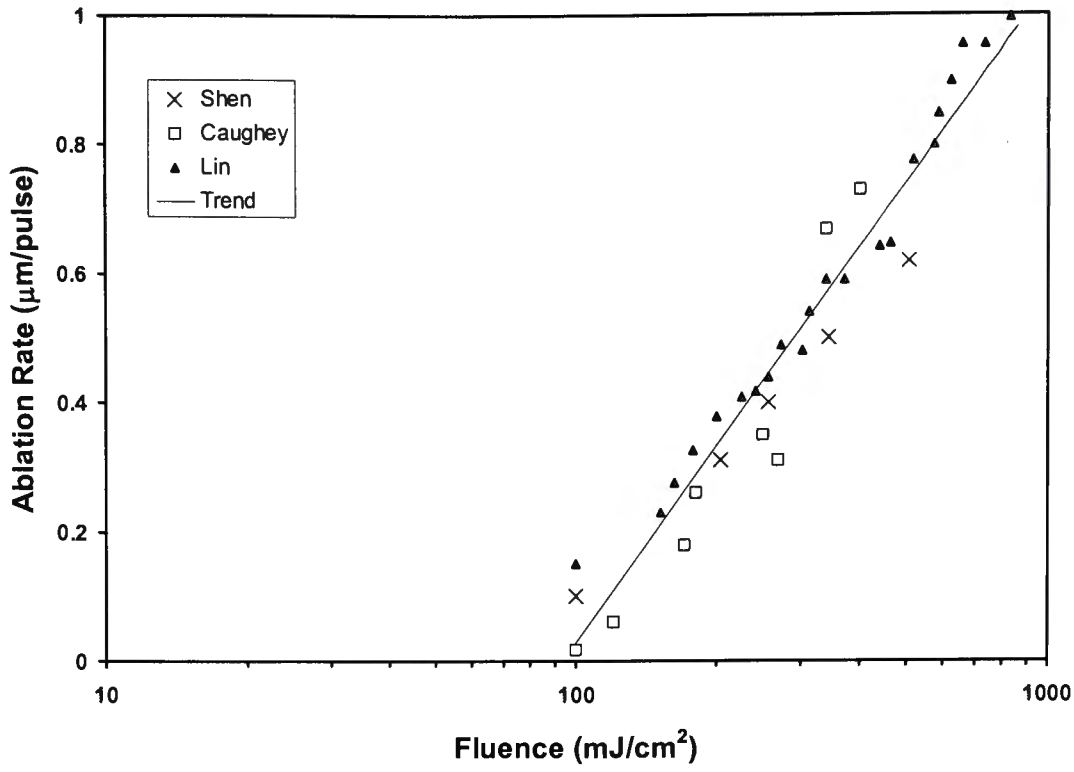

Figure 2.11. Semi-logarithmic plot of ablation rate results in PMMA using 213nm wavelength by various investigators.[156,167,175]

Very few studies have investigated the ablation of PHEMA using UV lasers. Chirila and Van Saarloos[176] were the first to characterise the ablation rate behaviour of this polymer. They reported an ablation rate of 0.08μm/pulse for a fluence value of 170mJ/cm^2. For all fluence values investigated, the ablation rate was lower than observed for PMMA. The excimer laser wavelengths of 193, 222 and 308nm were used in a later study by Costela et al.[177]. Their work used a wide range of fluence values extending to several Joules per square centimetre. At both 193 and 222nm, the ablation rate of PHEMA was observed to be lower than that of PMMA.

All previous studies that have investigated the ablation properties of the 213nm solid state laser wavelength have been constrained to the use of low output pulse energies[155,167,175,178-180]. These studies were restricted to using small beam diameters of 0.5mm or less to achieve a fluence value above the ablation threshold. A likely explanation for this low pulse energy lies in the nonlinear optical crystal configuration

used to generate the 213nm wavelength. The studies mentioned all employed BBO crystals to generate the fourth and fifth harmonic wavelengths of the Nd:YAG laser. As discussed in section 2.3.3, this places large restrictions on the overall conversion efficiency attainable.

2.6 Transmission of light through solution

A laser pulse incident on corneal tissue generally will have to propagate through gases and fluids before the onset of ablation can occur. Both of these mediums will therefore attenuate the pulse energy to some degree. The effect of gases in the form of an ablation plume from a previous pulse can be minimised through careful placement of each successive pulse within the ablation zone. The presence of any surface fluids on the cornea however, will result in some attenuation of the pulse. This point can in fact be used to advantage through the use of absorbing solutions as masking agents on the corneal surface[181,182]. This allows selective ablation of corneal irregularities in surgical procedures such as phototherapeutic keratectomy. With these points in mind, it is pertinent to briefly review the way in which light is attenuated through aqueous media.

The original form of the Lambert law of attenuation was first postulated in 1760 when Johan Lambert found that light transmission through a material depended upon the thickness of the material[183]. Also, that the ratio of the transmitted to incident light intensities is independent of the incident light intensity. In terms of radiant intensities this may be expressed as:

$$I_T = I_I e^{-\alpha d} \qquad \textbf{Equation 2.9}$$

where I_T and I_I are the transmitted and incident intensities respectively, α is the absorption coefficient and d is the sample thickness.

Equation 2.9 is essentially a restatement of equation 2.7 from page 30, only in exponential form and in terms of radiant intensity rather than fluence. The absorption coefficient generally has units of cm^{-1} and is a measure of the portion of incident energy absorbed per unit length of material[184]. The thickness of material whereby 63.2% of incident energy is absorbed is termed the penetration or skin depth and is a property of the material under investigation for a particular wavelength[185]. Penetration depth is defined by equating $d = 1/\alpha$ from equation 2.9.

Almost a century after Lambert formulated his original law, Beer conducted a review of this work and the relation became known as the Beer-Lambert law of attenuation with general form:

$$A = \log\left(\frac{I_I}{I_T}\right) \qquad \textbf{Equation 2.10}$$

which defines the absorbance, A of a material.

Application of equation 2.10 to a solution of a substance in a non-absorbing solvent yields the absorbance being proportional to the concentration. Thus:

$$A = \varepsilon d C \qquad \textbf{Equation 2.11}$$

Where C, the concentration in moles per litre and ε is the molar absorptivity with units of litres per mole per centimetre.

Chapter 3

3. Development of Pulsed Laser Sources

3.1 Introduction

The ablation rate and transmission studies performed in this project required the use of laser pulses having wavelengths in the deep UV. As such solid state lasers are not commercially available, it was necessary to first develop the laser sources required to produce these wavelengths with the appropriate pulse duration in the nanosecond regime. This chapter outlines the construction and characterisation of these laser sources.

Two lasers were developed based on different solid state materials. Discussed first is an Nd:YAG laser that was modified through the use of nonlinear optical crystals. The crystals provided the means by which the fifth harmonic wavelength of 213nm was generated. In the first section of the chapter, the characteristic behaviour of the output energy and the temporal profile of the pulse are discussed. This provided an overview of the laser performance for operation at the fundamental output wavelength. Following this, a description of the scheme of nonlinear crystals used for the harmonic generation is presented. The experimental results obtained for the harmonic wavelengths produced are discussed in terms of the overall conversion efficiency and the optimal fluence value for operation at the fundamental wavelength.

The second laser discussed is a Ti:sapphire based system (sections 3.3 and 3.4). Sapphire lasers provide the potential for broad wavelength tunability unavailable from Nd:YAG lasers. Like the Nd:YAG laser, this was pumped with flashlamps. However, the system was constructed in-house due to a lack of commercial availability of this

type of laser. These sections commence with a description of the custom built flashlamp charging circuit and outlines the electronic pulse forming network used. Next, the laser characterisation is described, which includes the experimental results obtained for the output pulse energy. The output energy is discussed in terms of input pump energy and the fundamental wavelength range achieved through tuning of the cavity. Results are provided for free running and Q-switched modes of operation.

The final section of the chapter is devoted to the scheme investigated for producing the fourth harmonic wavelength of the Ti:sapphire laser, including a brief discussion on the restrictions placed on the crystals used for fourth harmonic generation.

3.2 Nd:YAG Laser Characterisation

Before investigating the use of nonlinear crystals with the Nd:YAG laser, the device was characterised in terms of output energy and temporal profile. In addition to revealing the overall performance of the device, characterisation assisted in the optimisation of the harmonic generation.

The Nd:YAG laser used was a commercial device (Continuum Surelite II, Santa Clara, California) capable of producing ~370mJ of output energy in a Q-switched pulse at a wavelength of 1064nm and specified duration of ~7ns. The pulse repetition rate was 20Hz and the beam diameter 5.5mm. Output pulse energy was obtained by first measuring the average output power using a 10-P-V2-SH Ophir power detector (Ophir Optronics, Israel) and then calculating the energy per pulse. The temporal profiles were measured using a DET210 photodetector (Thorlabs, U.S.A) positioned to detect diffusely reflected energy. The resulting profile was captured using a storage oscilloscope.

One method of actively varying the output energy involved adjusting the Q-switch delay. Figure 3.1 shows the Nd:YAG laser energy as a function of Q-switch delay over a range of 170 – 320μs. A maximum output energy of 374mJ per pulse was obtained for a Q-switch delay of 180μs. As can be seen from the figure, further reduction of the Q-switch delay resulted in a decrease of the output pulse energy. As the Q-switch delay was increased, laser output was also reduced as more of the stored energy within the laser rod dissipated through spontaneous emission. Referring to Figure 3.1, it is obvious that if the Q-switch delay was further increased no laser output would be observed.

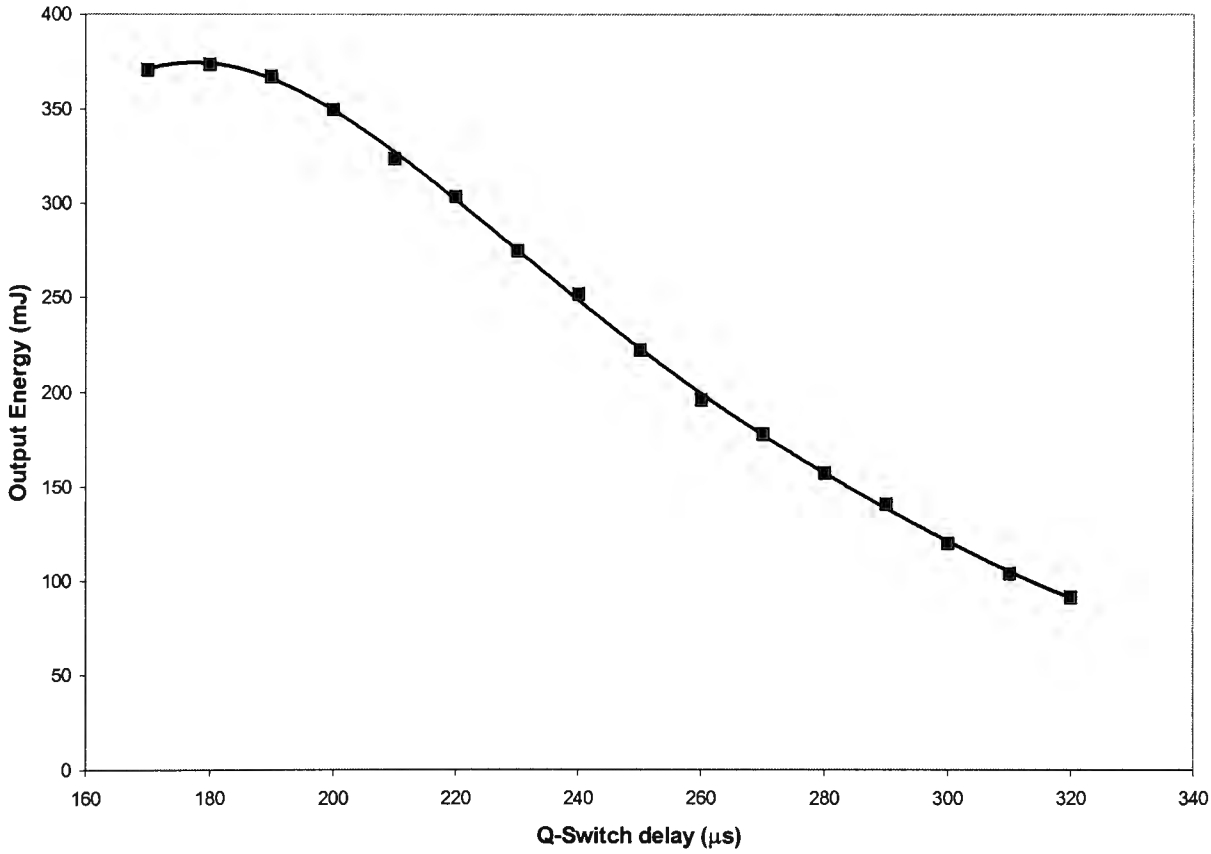

Figure 3.1. Nd:YAG laser output pulse energy at 1064nm with Q-switch delay. Laser repetition rate was 20Hz. Laser head serial number 3935-2A.

One consequence of varying the Q-switch delay of the laser is the effect this had on the temporal profile of the output pulses. Oscilloscope traces were obtained for Q-switch delay values of 190, 250 and 320μs. Figure 3.2a shows the temporal pulse profile at a Q-switch delay of 190μs. From the trace it can be seen that the pulse had a

gaussian envelope with a FWHM duration of ~9ns. Similarly, Figure 3.2b shows the pulse profile for a Q-switch delay of 320μs. This trace reveals that the FWHM value of the pulse had been broadened to ~17ns. This result was not unexpected when considering the laser Q-switching time. For the 320μs delay, the relative population of the upper laser level would be expected to be less than that for the more optimal 190μs delay. This would have the effect of reducing the small signal gain of the laser rod. Consequently, the pulse build up time within the laser cavity should increase, resulting in an output pulse of increased duration.

The change in the pulse duration and energy also affected the peak and average powers of the laser. At the maximum energy of 374mJ, the average power of the laser was 7.5W and the pulse peak power, 42MW. In contrast, operating at a Q-switch delay of 320μs, the pulse energy was 92mJ. The average power in this case was 1.8W and the peak power was 5.4MW. The reduction in the pulse peak power was accentuated by the factor of two in broadening of the pulse duration.

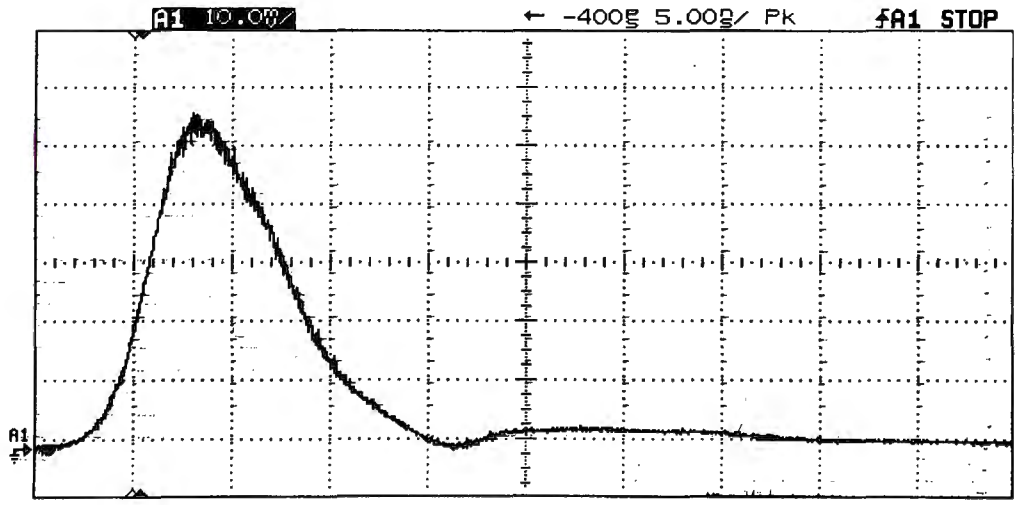

Figure 3.2a. Temporal profile of Nd:YAG laser output pulse with Q-switch delay of 190μs. Time scale: 5 ns.

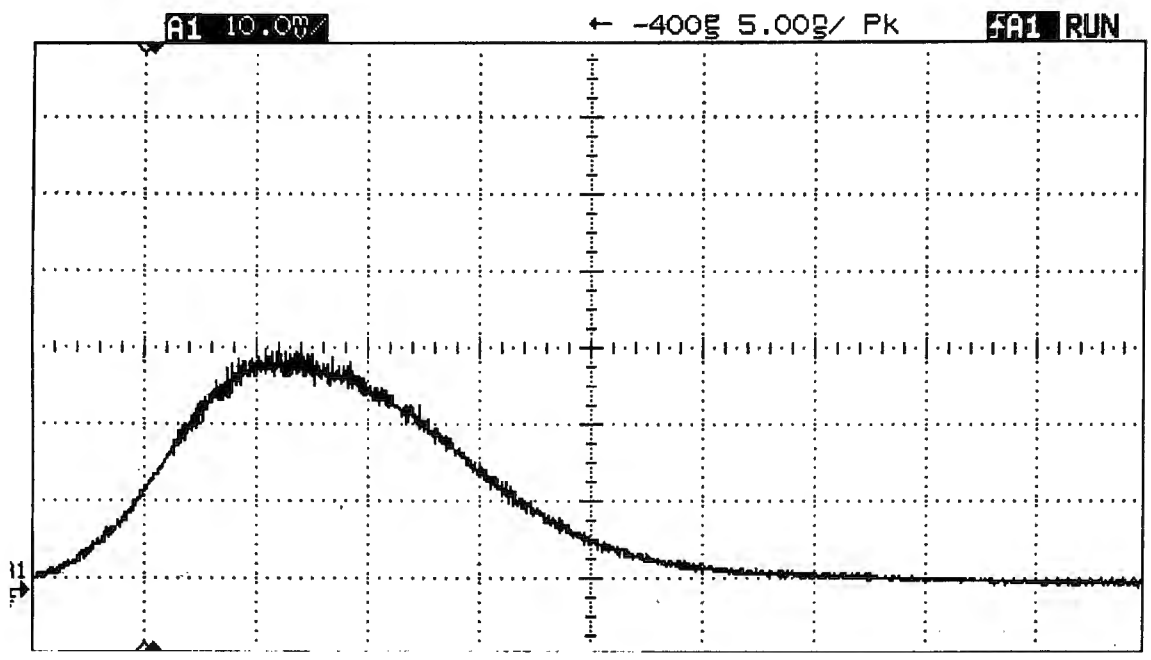

Figure 3.2b. Temporal profile of Nd:YAG laser output pulse with Q-switch delay of 320μs. Time scale: 5 ns.

3.2.1 Harmonic Generation

In order to generate the fifth harmonic wavelength of the Nd:YAG laser, three nonlinear crystals were employed. The second harmonic (532nm) was generated using a BBO crystal (Casix Inc. Fuzhou, China) and the fourth (266nm) and fifth harmonics (213nm) were generated using CLBO crystals (Crystal Associates Inc. New Jersey, USA.). To avoid hygroscopic effects, particularly in CLBO, the crystals were maintained at a temperature of 80°C. This was achieved using a Peltier heater arrangement within each crystal mounting[186].

Figure 3.3 provides a schematic overview of the conversion scheme used incorporating the three crystal stages. Each stage used a type 1 interaction, that is, that the polarisation of each generated wavelength was in a plane perpendicular to that of the input wavelength(s). This method made optimum use of the linearly polarised input of

the Q-switched pulse from the Nd:YAG laser. The various orientations of the polarisation for each wavelength are also shown in figure 3.3. For clarity, only the polarisations of the input and generated wavelengths are shown for each conversion stage. The inset of the figure displays the wavelengths and orientation of the polarisation vectors contained within the final output beam.

Table 3.1 shows some of the pertinent crystal parameters associated with each interaction. The values given in the table for angular acceptance refer to the angles obtained from calculations based on the specific crystal lengths used in this particular scheme. Other parameters such as phase matching angle, d_{eff} and walk off angle were obtained from the literature[3,93]. The relatively long length of BBO in the scheme resulted in that crystal having the smallest acceptance angle. As a consequence, the SHG of the 1064nm wavelength was the most sensitive to angular misalignment.

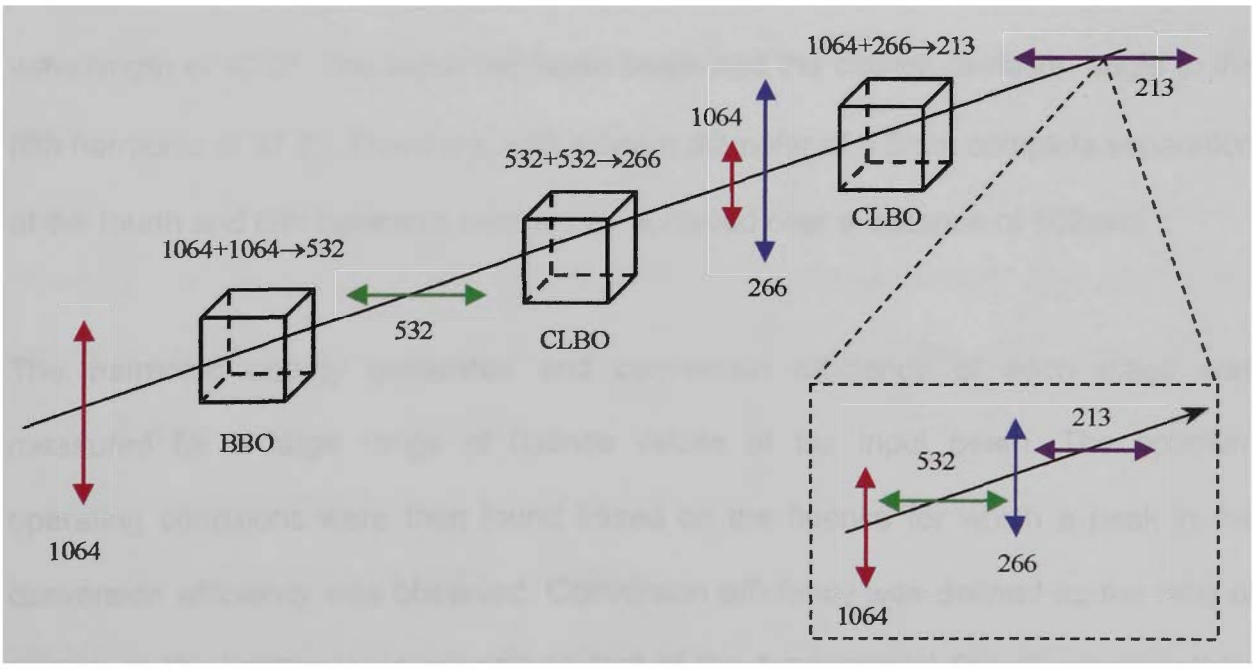

Figure 3.3. Harmonic conversion scheme for generating the fifth harmonic wavelength (213nm) of an Nd:YAG laser. Polarisation vectors of each wavelength in the output beam are also shown (inset).

Crystal	BBO	CLBO	CLBO
Interaction	1064+1064→532	532+532→266	1064+266→213
Polarisation	ooe	ooe	ooe
PM Angle (degs)	22.8	61.5	64.8
d_{eff} (pm/V)	2.1	1.0	1.2
Length (mm)	7	5	3
Walk off (degs)	3.2	1.9	1.9
Angular Acceptance (mrads)	0.73	0.95	1.22

Table 3.1. Crystal parameters for the fifth harmonic conversion scheme employed.

Following the final crystal in the scheme, the four resulting wavelengths propagate in a collinear fashion. The wavelengths were spatially separated using an equilateral prism made from UV grade fused silica (not shown in figure 3.3). For this prism, an incident angle of 50° was required to achieve the minimum beam deviation angle for the 213nm wavelength of 40.3°. The fourth harmonic beam had the closest deviation angle to the fifth harmonic of 37.2°. Therefore, with a beam diameter of 5.5mm complete separation of the fourth and fifth harmonic beams was achieved over a distance of 102mm.

The harmonic energy generated and conversion efficiency of each stage was measured for a large range of fluence values of the input beam. The optimum operating conditions were then found based on the fluence for which a peak in the conversion efficiency was observed. Conversion efficiency was defined as the ratio of energy at the harmonic wavelength to that of the fundamental (input) wavelength(s) (expressed as a percentage). Characteristic curves of each harmonic wavelength were plotted as a function of the fluence of the input wavelength. Considering that the fluence of the input beam is a function of both the beam diameter used and the pulse

energy, the corresponding input pulse energy is displayed on the secondary x- axis of the characteristic plots.

The characteristic plot for second harmonic generation is shown in figure 3.4. As may be expected, the amount of harmonic energy produced was found to be an almost linear function with increasing input fluence across the full range of values investigated. At lower fluence values (<1000mJ/cm^2) harmonic generation was completely linear with input fluence. These points were used to extrapolate the plot to gain an estimate of the threshold fluence for second harmonic generation. This was found to occur for an input fluence of ~190mJ/cm^2 (45mJ). At larger fluence values, the harmonic energy began to deviate from the linear trend, due to the onset of saturation of the conversion process.

On the other hand, at lower fluence values, the conversion efficiency was observed to increase with a decreasing gradient in a sigmoidal fashion. At an input fluence of ~950mJ/cm^2 a plateau region occurred corresponding to the maximum conversion efficiency of almost 51%. As the input fluence increased further (>1400mJ/cm^2) the conversion efficiency began to drop away as the energy generated deviated from linearity.

Operation at the optimal fluence of 950mJ/cm^2 with a 5.5mm diameter beam corresponded to an input pulse energy of 225mJ. Based on this data, operating the Nd:YAG laser at the maximum output pulse energy of 370mJ would require a beam diameter of approximately 7mm to achieve the optimal input fluence incident upon the crystal. This would allow a maximum energy of ~188mJ to be realised at the second harmonic wavelength.

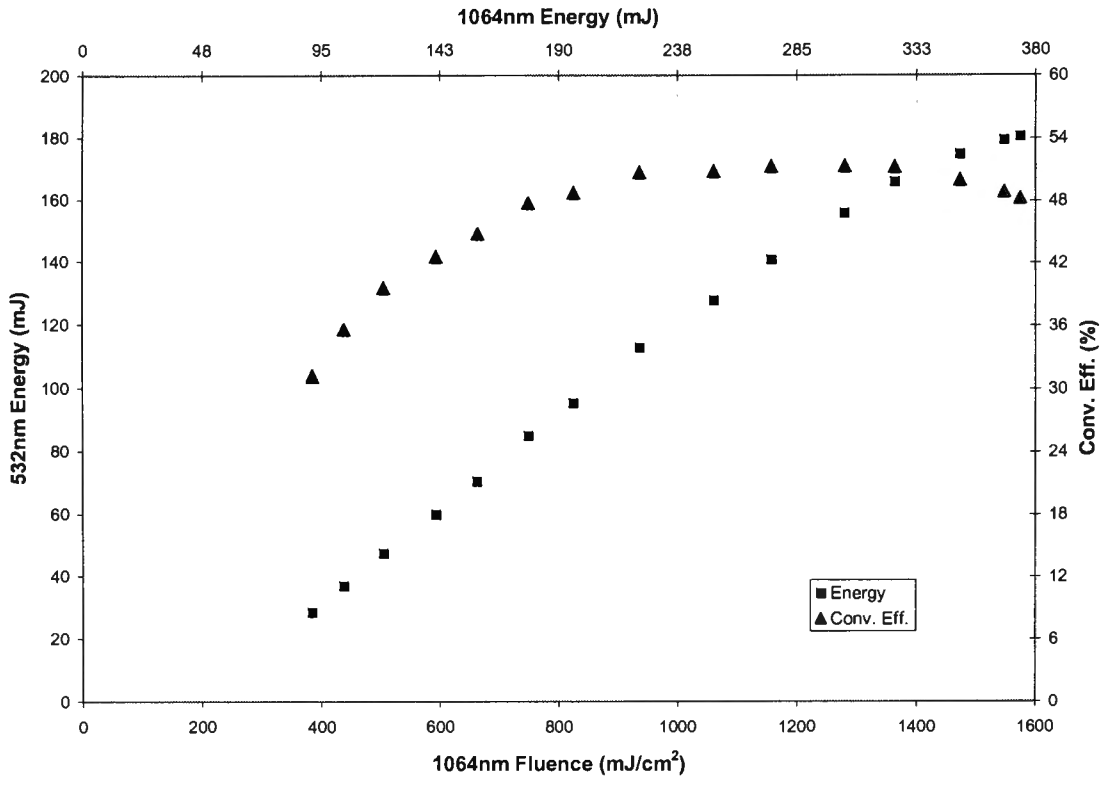

Figure 3.4. Second harmonic energy and conversion efficiency. Crystal type and dimensions: BBO, 8x8x7mm.

Figure 3.5 shows the fourth harmonic energy generated and conversion efficiency for 532nm input fluence. The trends of both functions are similar to those observed for the second harmonic generation (figure 3.4). The linearity of the 266nm energy however, was maintained over the investigated range of input fluence values. This suggests that the maximum 532nm fluence of 730mJ/cm^2 was below that required for any saturating effects to occur. Extrapolation of the fourth harmonic energy generation yielded a threshold input fluence of 60mJ/cm^2. A plateau in the conversion efficiency occurred at an input fluence of ~500mJ/cm^2. The conversion efficiency at this point was 48.6%. Application of the same analysis as that for the second harmonic data reveals that a beam diameter of 6.7mm should be used to allow the maximum available input energy to be applied at the optimal fluence value.

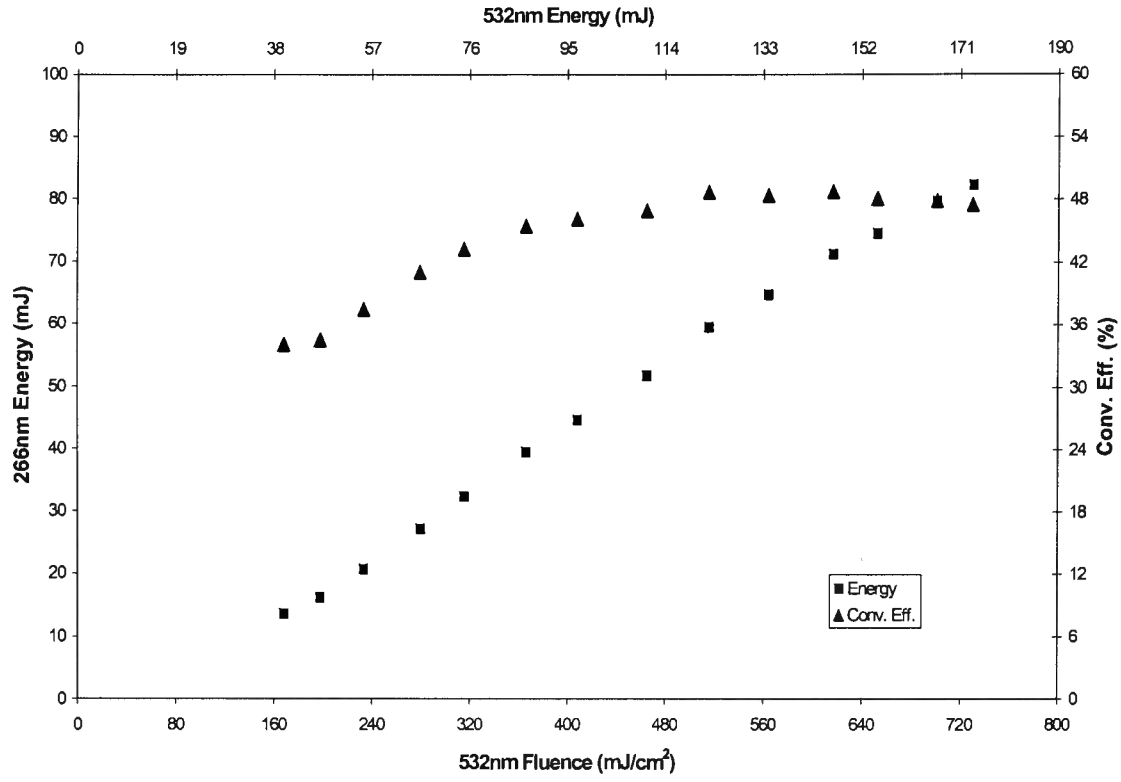

Figure 3.5. Fourth harmonic energy and conversion efficiency. Crystal type and dimensions: CLBO, 8x8x5mm.

Data obtained for the fifth harmonic wavelength is shown in figure 3.6. The interaction involved in generating the 213nm wavelength was one of sum frequency generation and incorporated the mixture of both the 1064 and 266nm wavelengths. The energy generated at the fifth harmonic was plotted against the initial input fluence values of the fundamental (1064nm) wavelength. This was done since plotting generated energy and conversion efficiency against just one of the input wavelengths would not prove meaningful because the relative energies of the two wavelengths are not independent. Also, the conversion efficiency figures shown represent the total or overall conversion of 1064nm input to 213nm output across the three crystal stages used.

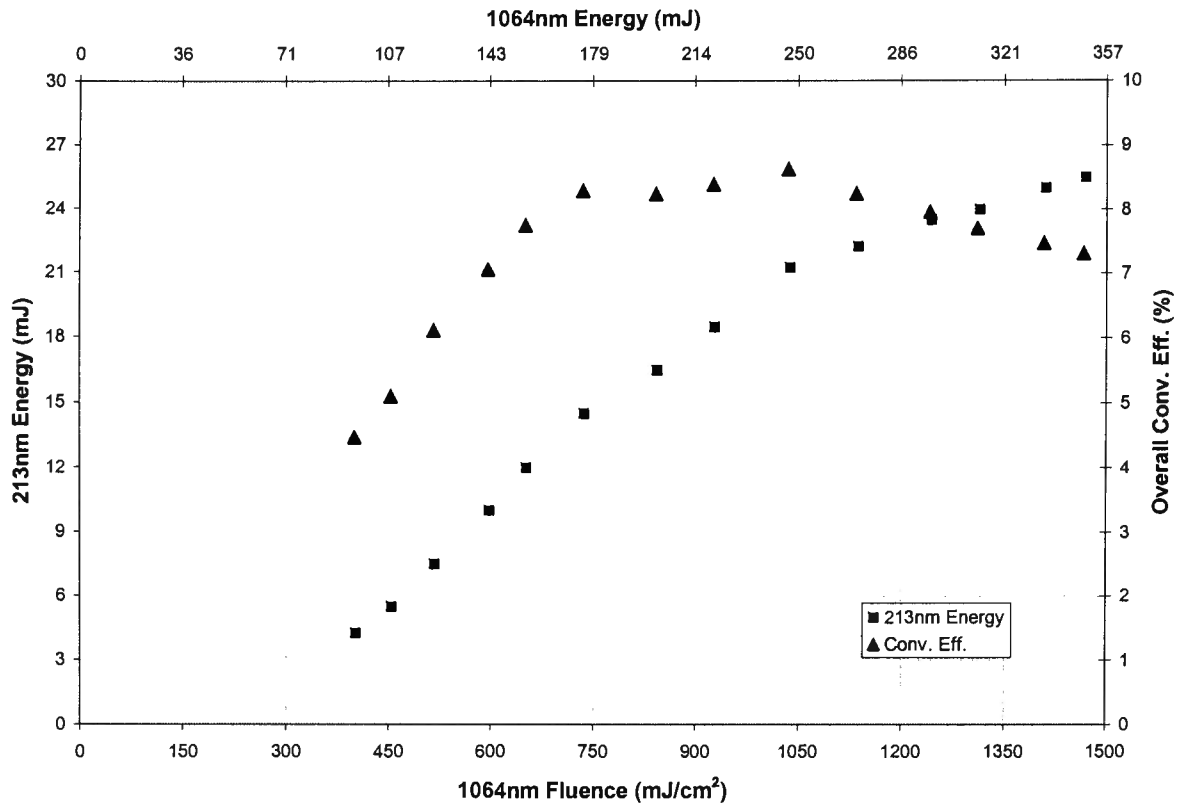

Figure 3.6. Fifth harmonic energy and overall conversion efficiency versus input 1064nm fluence and energy. Crystal type and dimensions: CLBO, 8x8x3mm.

A discontinuity in the linear gradient of the 213nm energy plot can be seen at a 1064nm fluence of 1040mJ/cm^2. At input fluence values greater than this the fifth harmonic energy appeared to be saturating. This point of discontinuity in the energy gradient also coincided with a steady reduction of the conversion efficiency. The maximum overall conversion efficiency obtained was 8.6% at a 1064nm input fluence of ~1000mJ/cm^2. Conversion efficiencies of greater than 8% were observed for an input fluence range of ~750 to 1150mJ/cm^2. Again extrapolating from the lower fluence (<1040mJ/cm^2) linear section of the 213nm energy plot a threshold input fluence of ~230mJ/cm^2 was obtained for harmonic generation. Also, using the input fluence of 750mJ/cm^2 for the point where the conversion efficiency enters a plateau region, an optimal beam diameter of 6.7mm could be inferred.

Figures 3.7 and 3.8 show the collective results for all harmonic wavelengths. The energy plot of figure 3.7 gives an indication of the overall performance of the three harmonic conversion stages of the system with 1064nm input. Likewise, figure 3.8 displays the relative conversion efficiencies for each stage. Note that the conversion efficiency for the 266nm wavelength had a plateau of approximately 24%. This is because the efficiency in this case is calculated against 1064nm input energy. In contrast, the efficiency values displayed in figure 3.5 were calculated using 532nm input energy as the fundamental wavelength. From figure 3.8 one can see the optimal fluence of the 1064nm beam occurred around 1000mJ/cm^2. Therefore, operation of the Nd:YAG laser at maximum pulse energy would require a beam diameter of 6.8mm. This would potentially yield 31mJ of 213nm output for 370mJ input energy at 1064nm.

The data presented in figures 3.4 to 3.8 was collected using the Nd:YAG laser with a repetition rate of 20Hz. The experiments were repeated at an Nd:YAG laser repetition rate of 2Hz to investigate if thermal loading of the nonlinear crystals due to incident average power affected the harmonic energy generated. The results showed no effect on either the amount of harmonic energy able to be generated or the conversion efficiency. Therefore, the data has not been presented.

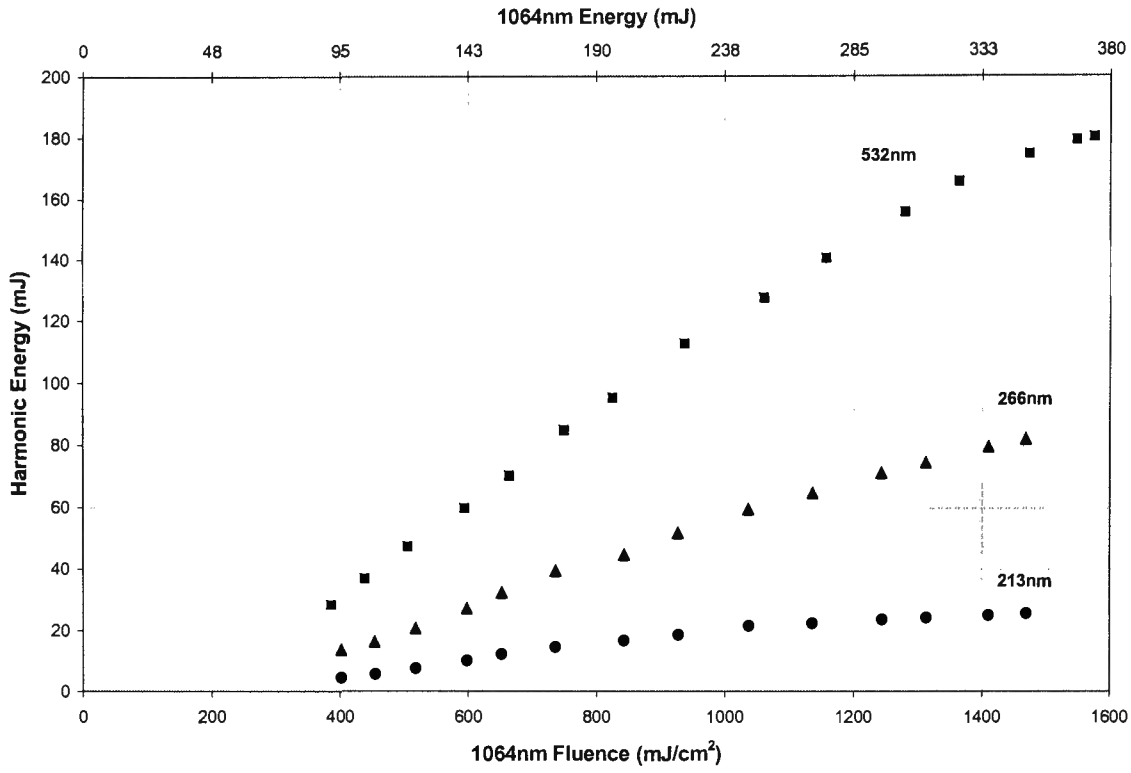

Figure 3.7. Second, fourth and fifth harmonic energy versus input 1064nm fluence and energy.

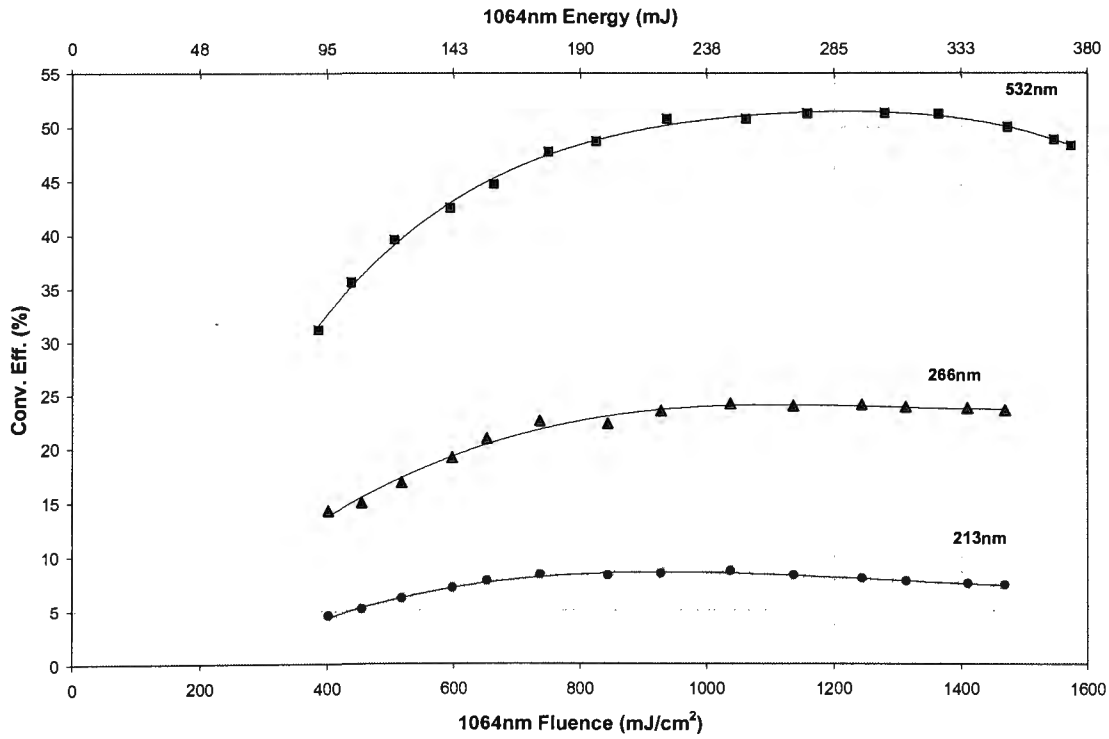

Figure 3.8. Second, fourth and fifth harmonic conversion efficiency versus input 1064nm fluence and energy.

The best reported overall conversion efficiency for the fifth harmonic wavelength is 10.4% by Yap *et al*[93]. This was achieved with a 1064nm input fluence of 1950mJ/cm^2, which is approximately a factor of 2 larger than the optimal input fluence observed in this work. The data presented by Yap *et al* however, showed a plateau in the overall conversion efficiency of over 10% occurred for a 1064nm fluence of ~1200mJ/cm^2. It is worthy to note that similar values of conversion efficiency have been achieved with the system described in this thesis. This generally occurred when new crystals were installed and the Nd:YAG laser was optimised in terms of beam divergence and spatial beam profile. The data presented in figures 3.4 to 3.8 represents more typical operating parameters achieved over an extended period of time.

The lower value of optimal input fluence observed here compared with that achieved by Yap *et al* may be attributed to a number of factors. For example, the CLBO crystals used by Yap *et al* were not temperature stabilised. Later work revealed that CLBO is highly hygroscopic and requires constant temperature control to avoid variation in the refractive index values throughout the material[96]. Crystal quality, along with laser parameters also play a role in the overall conversion efficiency.

3.3 Ti:Sapphire Laser Construction

The construction of the flashlamp pumped Ti:sapphire laser comprised two major facets. The high voltage flashlamp pumping circuit was first established. Secondly, the actual laser cavity was designed and built. Following this the laser was characterised and optimised.

The flashlamp driving circuit used in the laser construction was similar in design to that put forward by Hoffstadt[45], which used a thyratron switch to discharge a high voltage capacitor. The capacitor was charged to a positive voltage to drive four flashlamps in series. The circuit used for this project employed a spark gap switch to discharge a

capacitor charged to a negative voltage to drive two flashlamps in series. The circuit is shown below in Figure 3.9.

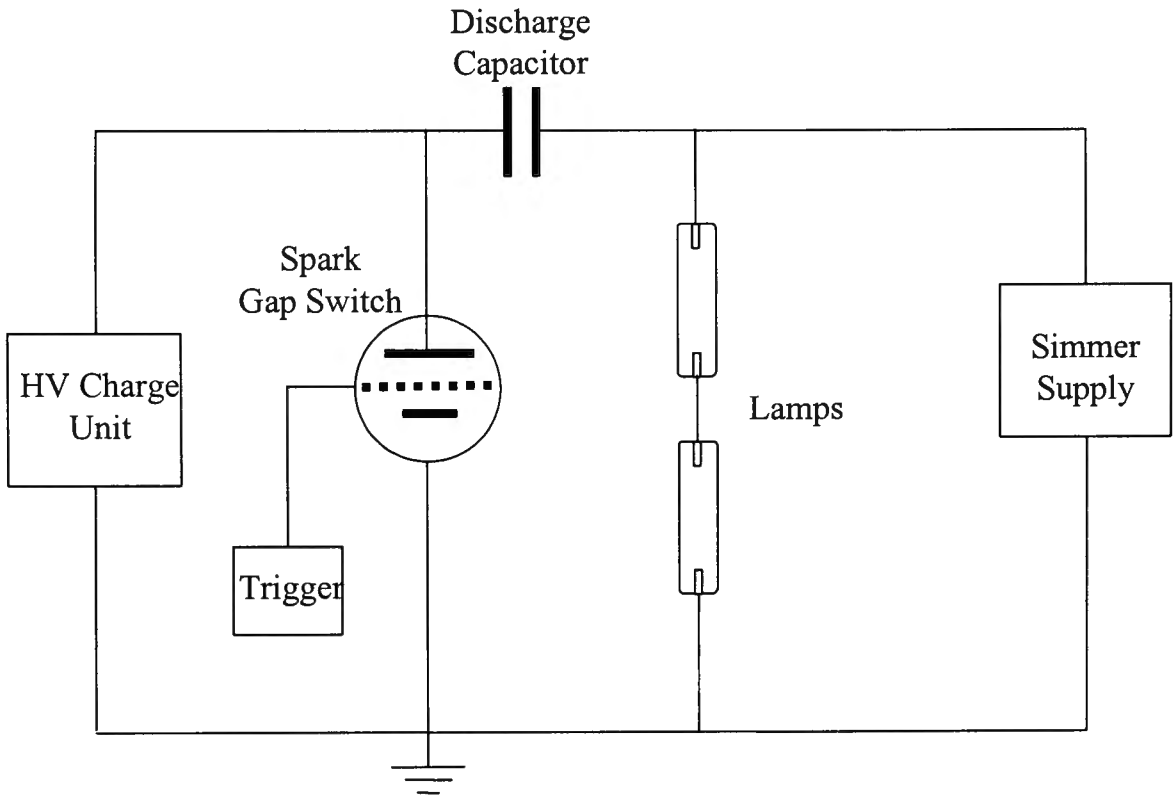

Figure 3.9. Flashlamp circuit configuration and components.

HV Charge Unit	Kaiser -15 kV, 1.5 kJ/s
Spark Gap	EG&G ~8 kV triggering threshold
Discharge Capacitor	Main Discharge Capacitor (oil filled) 1 μF
Lamps	Kigre K309 Series Xenon Filled Flashlamps (500 Torr) 4mm bore, 6mm OD, 5.5" arclength, 45.6 Impedance parameter

Referring to Figure 3.9, the spark gap was triggered to initiate an energy discharge, resulting in the negative side of the capacitor being "pulled' up to ground. Consequently, a positive voltage discharge was initiated through the lamps. The main discharge capacitor was able to be charged to a maximum of –15kV providing up to 112J of electrical energy. This configuration produced the basis of the pulse forming network. Most pulse forming networks employ an inductor to create a conventional LRC circuit.; the value of the inductance being chosen to achieve a desired discharge

pulse length. The pulse length ideally should match the upper state lifetime of the laser rod being pumped. Ti:sapphire, having a short upper state lifetime of ~3μs, introduced the requirement to minimise the circuit inductance. The circuit inductance was therefore supplied from the natural inductance of the circuit leads and for design purposes was estimated to be[12] approximately 1μH.

The temporal pulse shape of the discharge was measured using an oscilloscope and a high voltage circuit probe for various values of the capacitor charge voltage. The circuit probe was placed across the flashlamps to observe the oscilloscope trace. The discharge voltage pulse duration was found to be independent of charge voltage between 10 and 14kV, and had a value of ~3μs. Oscilloscope traces of the discharge waveform are shown in Figure 3.10a,b for charge voltages of 10 and 14kV. The trace of the 10kV discharge exhibited a degree of circuit ringing where the voltage polarity was reversed in the flashlamps, 6 – 10μs after triggering.

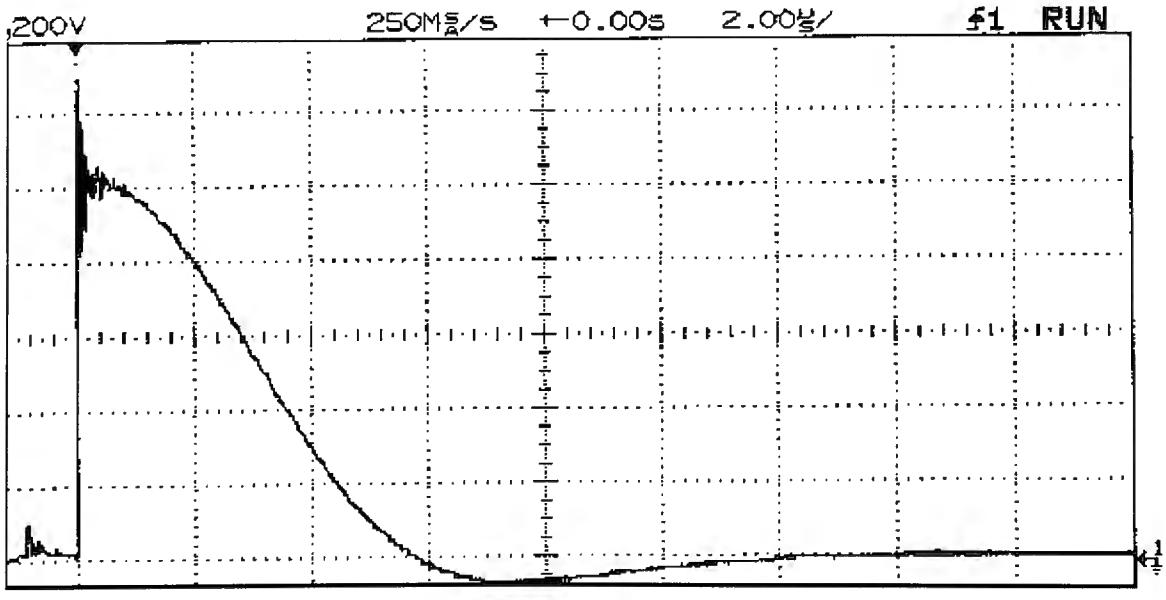

Figure 3.10a. Discharge pulse waveform for charging voltage of 10kV. Voltage scale: 2 kV/Div. Time scale 2 μs.

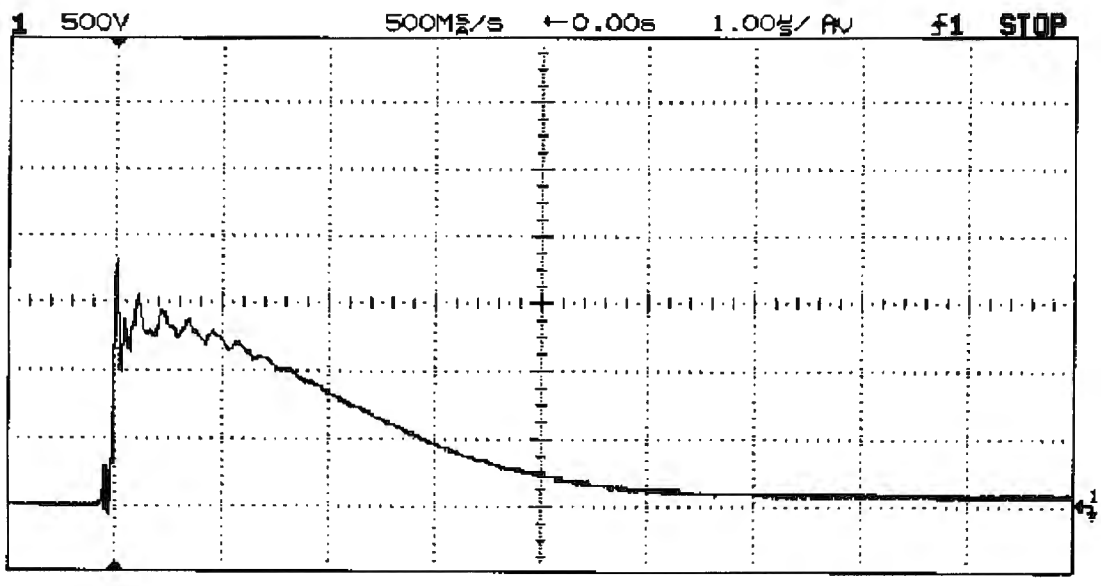

Figure 3.10b. Discharge pulse waveform for charge voltage of 14kV. Voltage scale: 5 kV/Div. Time scale: 1 μs.

The performance of the high voltage charging unit was also investigated. Figure 3.11 shows the negative voltage waveform across the main capacitor for two charging cycles. The figure reveals that the capacitor was charged linearly up to the set voltage of –12kV. The charging period required for this voltage was 60ms. The charge unit was rated to charge up to a maximum rate of 1.5kJ/s. At 12kV, 72J of electrical energy was stored within the capacitor. Therefore a maximum repetition rate of 20Hz could theoretically be achieved. However, based on the observed charging time of 60ms, a rate of 17Hz would be achieved in practice. This indicates that the charging unit was operating slightly below specifications.

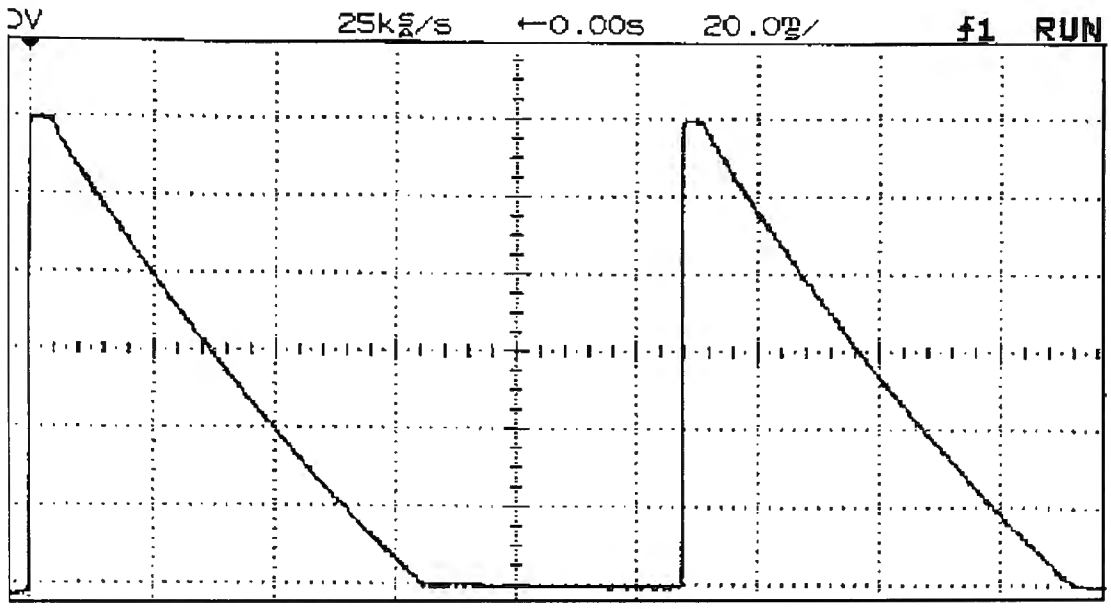

Figure 3.11. Capacitor charging waveform. Charge voltage was –12kV. Voltage scale: 2 kV/Div. Time scale: 20 ms.

Although the voltage waveform of the discharge through the flashlamps was on the order of 3-4μs, for comparison the form and duration of the optical pulse output by the flashlamps was also investigated. This is shown in figure 3.12. The waveform was obtained by placing a diode detector (DET210, Thorlabs, USA) in close proximity to the flashlamps contained in the pump chamber. The duration of this waveform was approximately 13μs FWHM, a factor of four longer than the upper state lifetime of the sapphire rod of ~3.2μs. Although it should be noted that the wavelength spectrum of this pulse was not monitored, an optical pump pulse of this duration would be expected to be non-optimal.

The output spectrum of a flashlamp is affected by the output pulse duration and discharge voltage. Both these factors affect the current density within the flashlamp and consequently the output wavelength spectrum. This point was discussed in more detail in section 2.2.3. In our case of having a pulse duration in the micro-second region, the output spectrum would be expected to be shifted towards the ultraviolet.

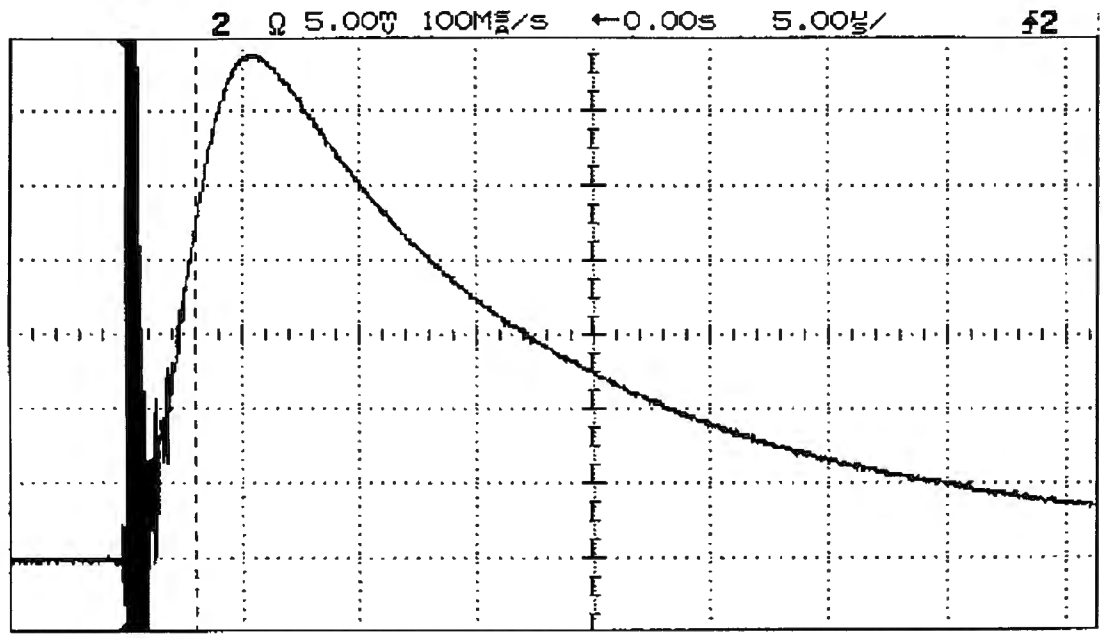

Figure 3.12. Temporal profile of the optical output pulse delivered from the circuit flashlamps. Discharge voltage was 11kV.

3.4 Ti:Sapphire Laser Characterisation

3.4.1 Laser Cavity

The basic cavity design is shown schematically in figure 3.13. This figure includes all the intra-cavity components used for Q-switching and wavelength tuning of the laser. Figure 3.14 displays a photograph of the actual laser cavity. The combination of the quarter wave plate and polarising element meant the cavity suppressed laser oscillation without any voltage being applied to the Pockels cell. During operation, the output wavelength was tuned by adjusting the output coupler mirror through the horizontal plane (plane of the page).

The laser output was characterised for three different flat output coupling mirrors and will be discussed in the following section. The high reflecting rear mirror was a flat mirror with a BBHR coating for a central wavelength of 850nm. The fused silica prism provided tunability of the output wavelength and had an apex angle of 68°. The cylindrical sapphire laser rod was manufactured with dimensions of 5mm diameter and

150mm length and was doped with 0.15% titanium ions (Union Carbide). The flat cut ends were AR coated for 800nm and the barrel was ground finished. The rod had a figure of merit of 214.

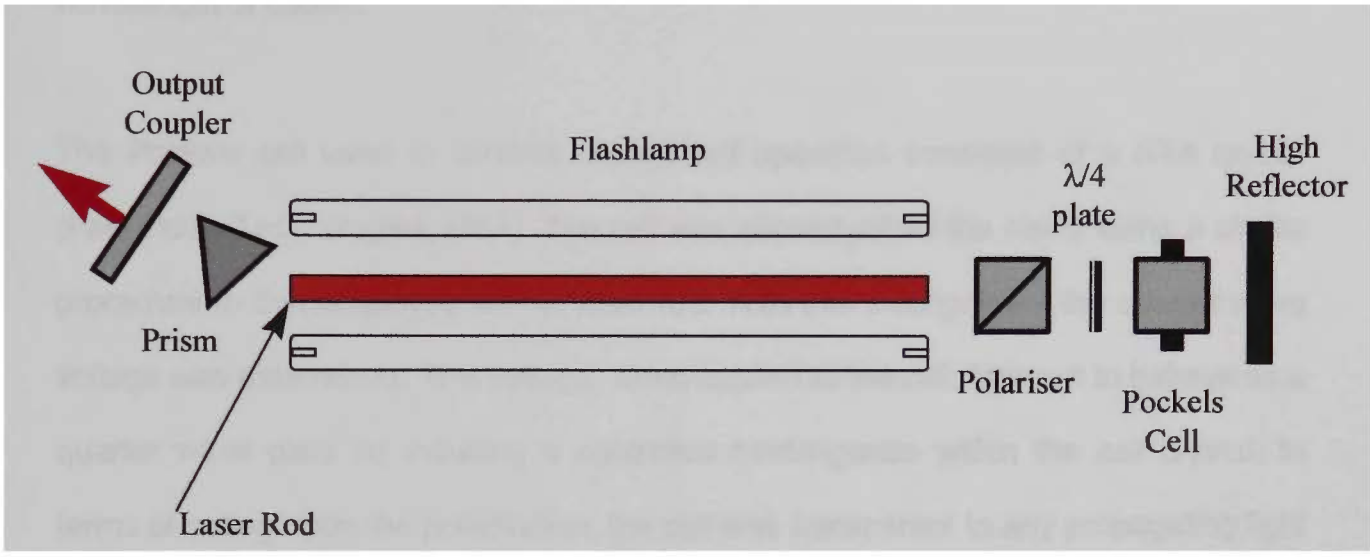

Figure 3.13. Optical laser cavity schematic for flashlamp pumped Ti:sapphire laser.

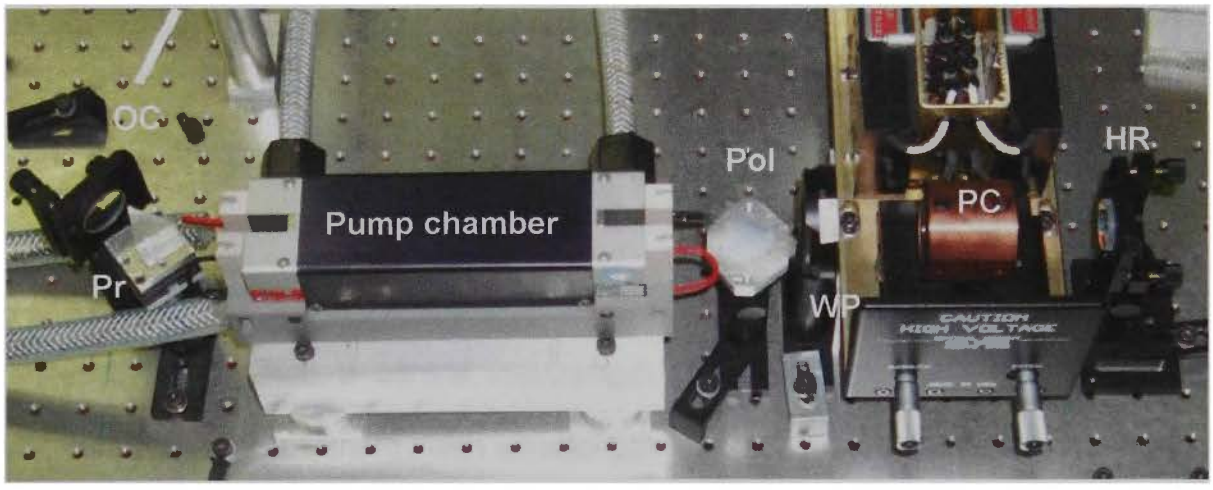

Figure 3.14. Photograph showing Ti:sapphire laser cavity. Labelled components include the output coupler (OC), tuning prism (Pr), flashlamp pump chamber, polariser (Pol), quarter wave plate (WP), Pockels cell (PC) and high reflector (HR).

As a material, sapphire exhibits natural birefringence. The peak stimulated emission cross section occurs for polarised light parallel to the optic axis[8]. Therefore the rod needed to be aligned within the pump chamber such that the laser output would be

horizontally polarised (in the plane of the page in figure 3.13). This was achieved by placing the rod between two crossed polarisers and passing a cw laser beam through it. The rod was then rotated about the axis of beam propagation until the required orientation was found. The cw laser source used for this alignment procedure had a wavelength of 800nm.

The Pockels cell used to achieve Q-switched operation consisted of a RTA crystal (Fast Pulse Technologies, USA). The cell was aligned within the cavity using a similar procedure to that employed for the laser rod. With this arrangement the quarter wave voltage was determined. This voltage, when applied to the cell, forces it to behave as a quarter wave plate by inducing a controlled birefringence within the cell crystal. In terms of acting upon the polarisation, the cell was transparent to any propagating light when no voltage was applied and the cell was in correct alignment. A quarter wave voltage of 4.2kV was obtained for a wavelength of 800nm.

3.4.2 Output Energy

Laser output was characterised for three different output coupler mirrors. The mirrors tested had reflectivities of 30, 50 and 70%. The broad band reflection coatings had a central wavelength of 850nm for the 30 and 70% reflectivity mirrors, while the 50% reflectivity mirror had a central wavelength of 780nm. Figure 3.15 shows the Q-switched output pulse energy with wavelength for each of the mirrors tested. All mirrors showed a maximum output energy for a wavelength of ~800nm. This wavelength is at the peak of the sapphire gain curve. The 30% reflectivity mirror exhibited the lowest output energy and least tuning range of all the mirrors. This suggests that the laser cavity was over coupled for this mirror reflectivity. The maximum output energy was the same for the other two higher reflectivity mirrors. It could be that a difference in the maximum output energies was not observed due to a reduction of reflectivity at this wavelength of the 70% reflectivity mirror. The 50% reflectivity mirror with a central

wavelength of 780nm was able to tune to the lowest wavelength of 740nm. At the longer wavelength end, the 70% reflectivity mirror maintained the most output energy up to a wavelength of 880nm. This wavelength is only 30nm from the central wavelength of 850nm. No output energy could be detected for wavelengths beyond 880nm.

In free running mode the output energy was plotted against input pump energy (figure 3.16) for two different pump chambers. The input energy was varied by adjusting the capacitor discharge voltage. The pump chambers were supplied by two manufacturers, Kigre (SC, U.S.A) and Kentek (NH, U.S.A). The output wavelength was kept constant at 800nm for these experiments. The data was obtained using the 50% output coupler in a cavity containing the tuning prism as the only intra-cavity component. This mirror was chosen as no difference was displayed between the 50% and 70% mirrors for a wavelength of 800nm. The results showed the pump chamber supplied by Kigre gave superior performance than when the Kentek chamber was used. The slope efficiency was 0.38% for the Kigre chamber and 0.32% for Kentek.

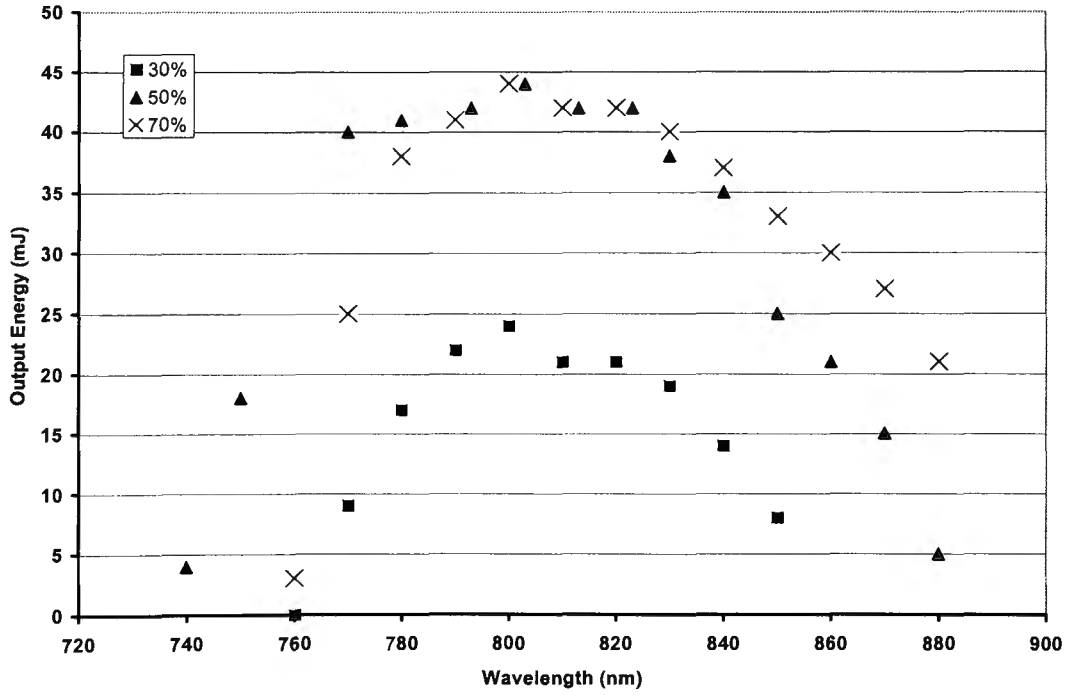

Figure 3.15. Ti:sapphire Q-switched pulse energy for various output couplers. Flashlamp input energy was 60J corresponding to a capacitor charge voltage of 11kV.

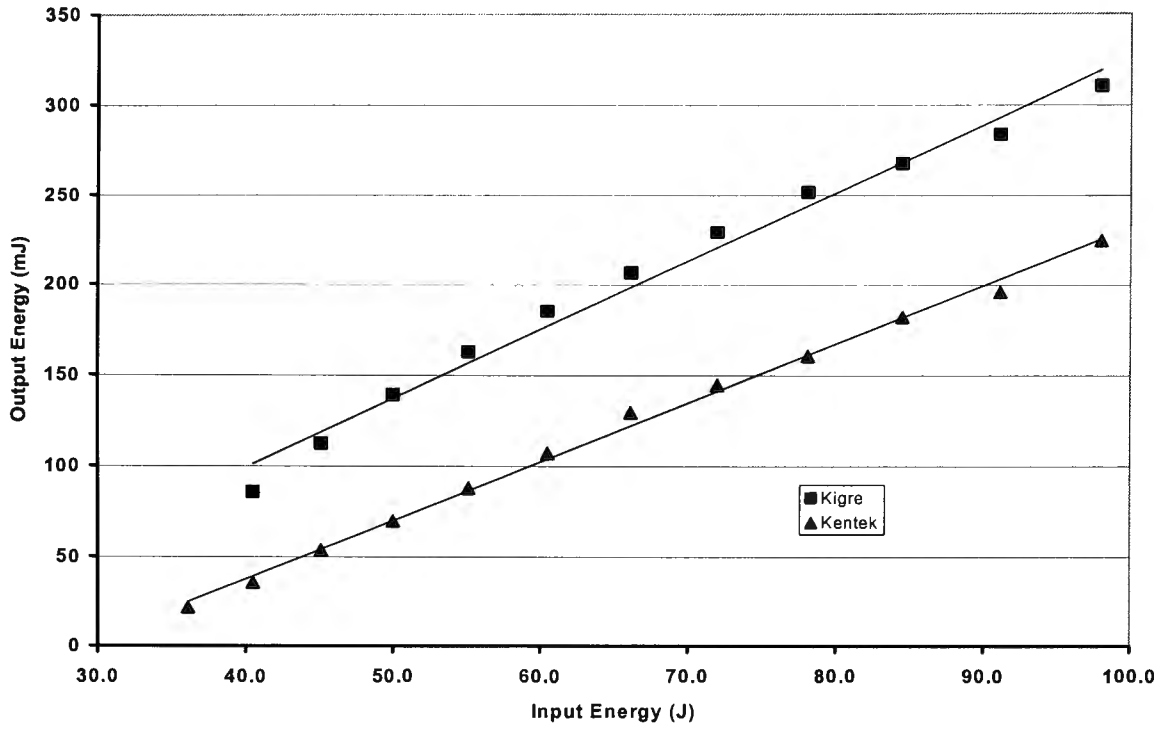

Figure 3.16. Free running output pulse energy using pump chambers from two manufacturers. Output wavelength was 800nm. Slope efficiency: 0.38% (Kigre), 0.32% (Kentek).

Free running pulsed operation realised greater energy per pulse than that obtained from Q-switched operation. The temporal profile however, observed from these two regimes was vastly different. In free running mode the pulse envelope had several spikes and a duration of 5μs. For a maximum pulse energy of 310mJ the peak power was ~60kW. Figure 3.17a shows the temporal pulse profile in the free running mode. The Q-switched pulse envelope is shown in figure 3.17b as channel 1 of the oscilloscope trace. This displays a more regular profile, taking on a gaussian form. Also shown in this figure is the high voltage switching of the Pockels cell (channel 2). The quarter wave voltage was applied for ~1.1μs. The Q-switched pulse displayed a duration of ~200ns, which for a pulse energy of 40mJ, corresponded to a peak power of 200kW.

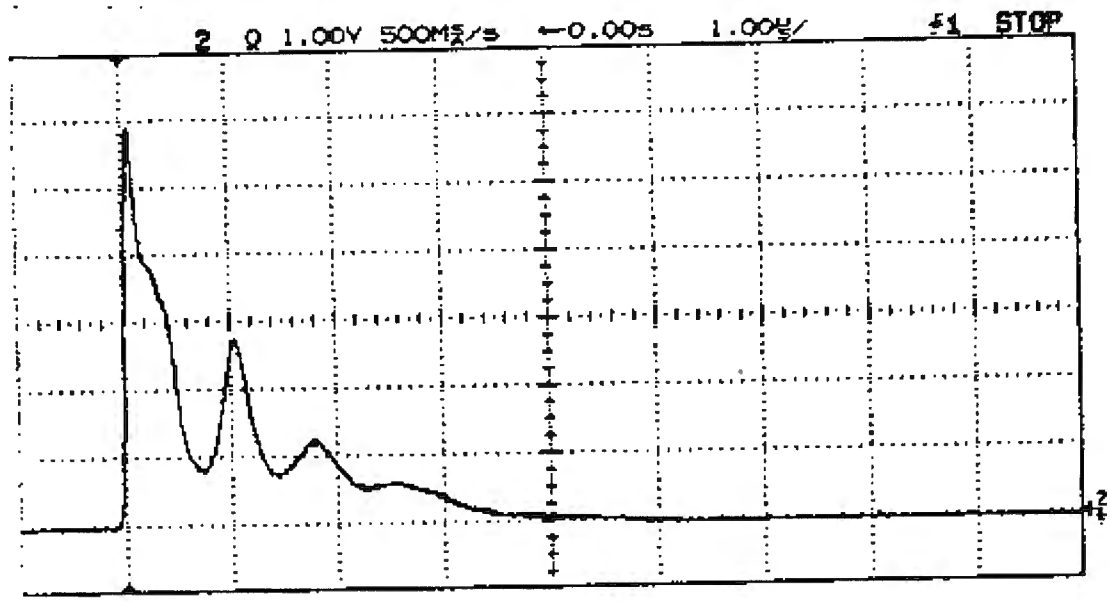

Figure 3.17a. Example of a free running pulse profile. Time scale: 1 µs.

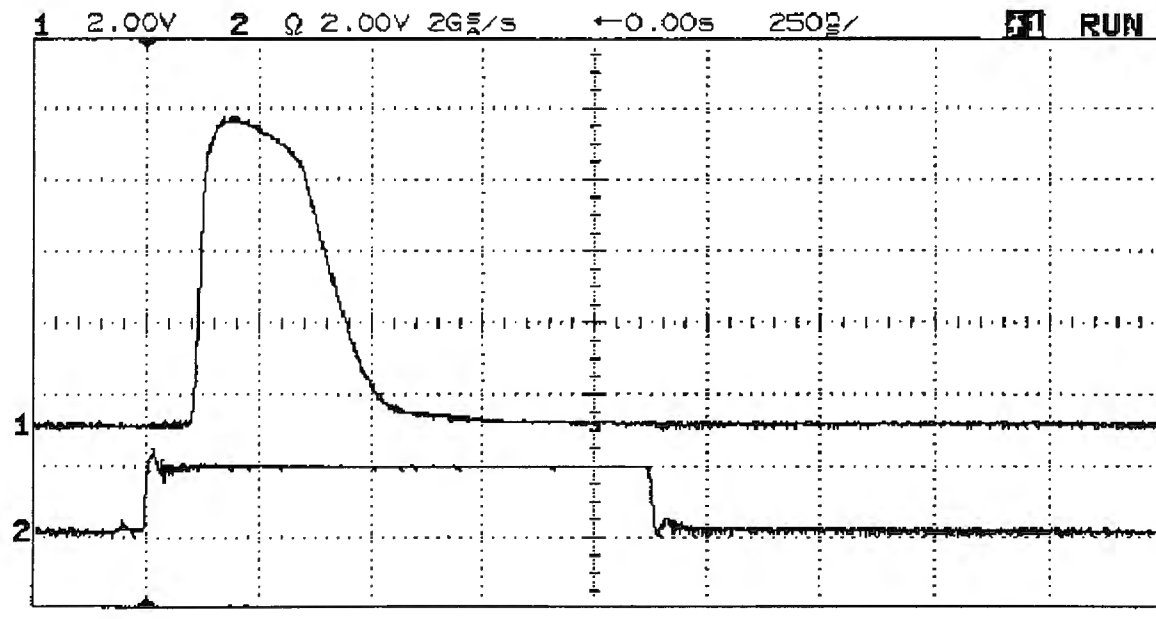

Figure 3.17b. Temporal profile of Q-switched output pulse (channel 1). Pockels cell switching time also shown (channel 2). Time scale: 250 ns.

3.4.3 Harmonic Generation

Due to the wide tunability of the Ti:sapphire laser, harmonic generation is possible over a relatively broad range of wavelengths. A tunable range for the fundamental wavelength of 100nm translates to a 25nm spectral range at the fourth harmonic wavelength. Therefore, to generate wavelengths between 205 and 230nm, the Ti:sapphire laser is required to be tuned between wavelengths of 820 and 920nm.

Fourth harmonic generation was achieved using two nonlinear crystal stages, shown schematically in figure 3.18. The figure depicts the conversion of the 850nm wavelength to 213nm. This was chosen due to the similarity with the fifth harmonic wavelength of the Nd:YAG laser discussed in the preceding sections. In a similar fashion to figure 3.3, the relative polarisations of all wavelengths present in the final beam are also shown. The resulting beam of this configuration contained three wavelengths that were then spatially separated using a prism of the type used in the Nd:YAG laser experiments.

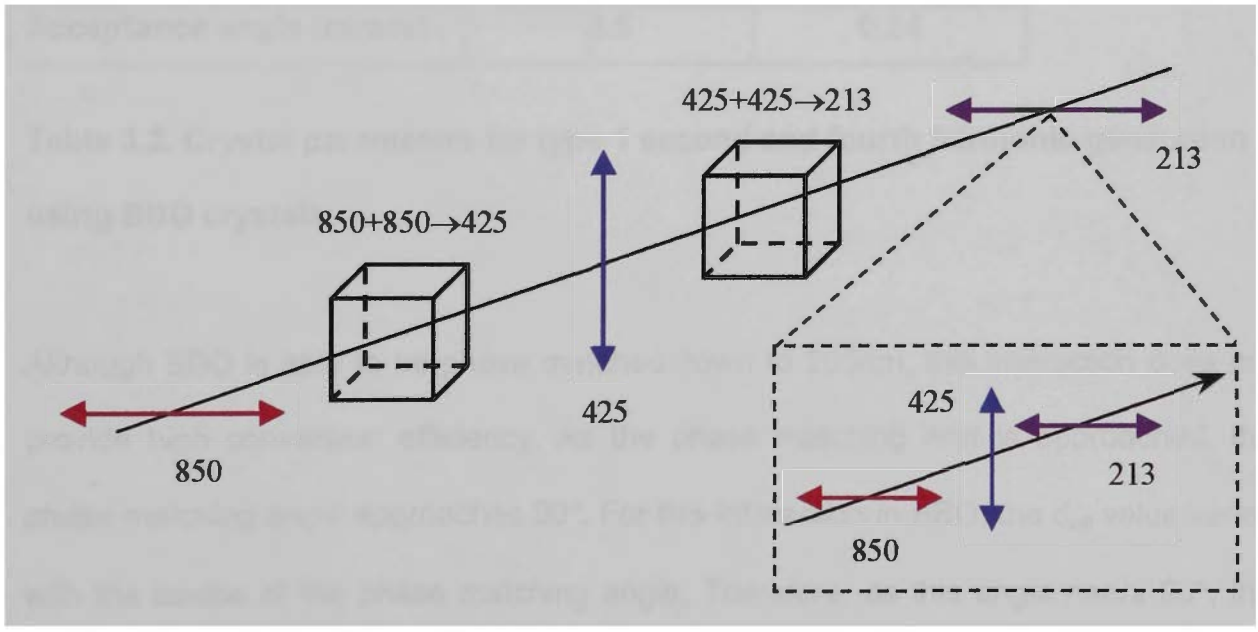

Figure 3.18. Two stage configuration for fourth harmonic generation of a Ti:sapphire laser. Polarisation vectors of each wavelength in the output beam are also shown (inset).

Although several nonlinear crystals exist which are capable of producing the second harmonic wavelength, only BBO was tested for this interaction, due to favourable characteristics such as a high d_{eff} value. Table 3.2 shows various crystal parameters of BBO for type 1 frequency doubling and quadrupling of 850nm light. The table reveals that BBO has a greatly reduced d_{eff} value for generating the fourth harmonic wavelength. A smaller walk off angle is also preferred when higher harmonics are to be generated in subsequent crystal stages[101]. Carrying out phase matching calculations based on crystal dispersion relations, it became evident that to produce the fourth harmonic using frequency doubling, BBO emerged as the only practical candidate.

Crystal	**BBO**	**BBO**
Interaction	850+850->425	425+425->212.5
Polarisation	ooe	ooe
PM Angle (degs)	27.5	73.0
d_{eff} (pm/V)	2.04	0.93
Length (mm)	10	10
Walk off (degs)	3.7	3.0
Acceptance angle (mrads)	3.5	0.24

Table 3.2. Crystal parameters for type 1 second and fourth harmonic generation using BBO crystals.

Although BBO is able to be phase matched down to 205nm, this interaction does not provide high conversion efficiency. As the phase matching limit is approached, the phase matching angle approaches 90°. For this interaction in BBO, the d_{eff} value varies with the cosine of the phase matching angle. Therefore, as this angle nears 90°, the value of the d_{eff} vanishes. In this wavelength range the phase matching angle is also a steeply varying function. With this in mind, more than one BBO crystal for the second stage with different cutting angles would be required to cover a fourth harmonic wavelength range of 210-220nm. This corresponds to a fundamental wavelength range of 840-880nm.

A plot of the output energy and conversion efficiency obtained for various second harmonic wavelengths is shown respectively in figures 3.19 and 3.20.

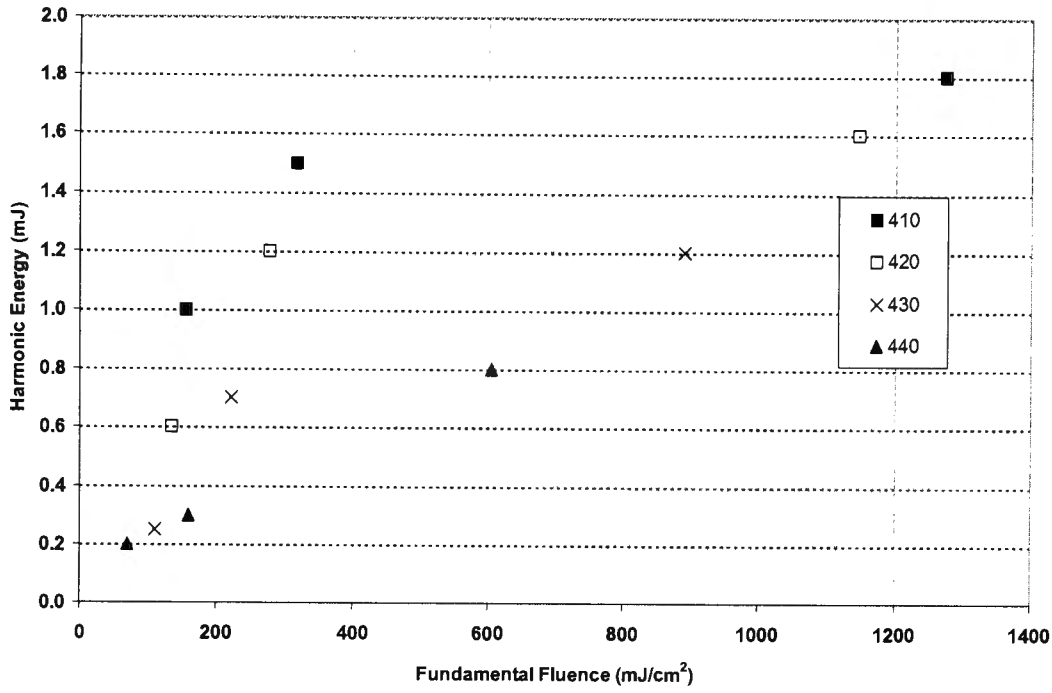

Figure 3.19. Second harmonic energy versus fundamental fluence for various wavelengths of the Ti:sapphire laser.

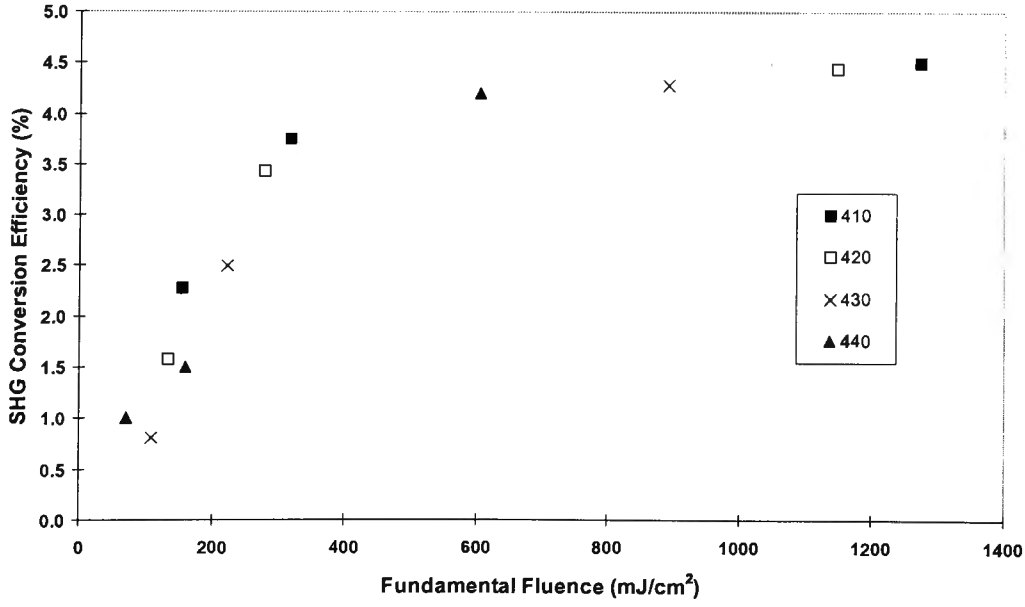

Figure 3.20. Second harmonic conversion efficiency versus fundamental fluence for various harmonic wavelengths.

The energy plot of figure 3.19 shows no real correlation to linearity for fluence values below approximately 300mJ/cm^2. For fluence values greater than 600mJ/cm^2, the data exhibited greater linearity for the four wavelengths measured. The low energies obtained for the second harmonic wavelengths restricted the conversion efficiency to a maximum of approximately 4.5% (figure 3.20). The maximum values occurred for harmonic wavelengths of 410 and 420nm for which the greatest fluence of the fundamental wavelength was achieved. Similar fundamental fluence values were not measured for all wavelengths because of the different amount of input energy involved. The fluence of the fundamental beam was varied by magnifying the beam to different diameters using a Galilean telescope comprising two lenses such that beam collimation was maintained for both the input and output beams.

The second harmonic conversion efficiency achieved meant that insufficient radiation could be generated at the fourth harmonic wavelength to be detected using the available power detector. All measurements were obtained using a Newport power meter (model 1825-C; Newport, Santa Ana, CA) with a detector (model 818T-10; Newport) to measure average power.

A number of problems contributed to the disappointing results obtained for generating the fourth harmonic wavelength of the flashlamp pumped Ti:sapphire laser. As a laser medium, Ti:sapphire achieves optimal operation in terms of output pulse energy for wavelengths around 800nm. Unfortunately, for fourth harmonic generation using two frequency doubling stages, this corresponds to a region of vanishing returns. Therefore, by increasing the fourth harmonic wavelength to improve conversion efficiency, a less favourable fundamental wavelength is required. This point is exacerbated by the fact that the ends of the laser rod used were coated for operation at wavelengths of around 800nm. Another factor that may have contributed to the low fundamental energy achieved could be the quality of the laser rod. The rod FOM of 214

is below what is currently available. Rod FOM values of up to 800 can be obtained from some manufacturers.

Generation of the fourth harmonic wavelength using three crystal stages may prove to be more efficacious than the scheme used in this project. This would involve the addition of the third harmonic and fundamental wavelengths at the final crystal stage. A scheme of this type also reduces the lower wavelength limit in the UV. For example, it is possible to generate a fourth harmonic wavelength of 195nm, which would require a fundamental wavelength of 780nm. As discussed, this wavelength allows for optimal operation of the Ti:sapphire laser. Also, for BBO the final addition stage does not have a diminishing susceptibility. Investigations employing this kind of scheme have been carried out using short pulse, mode locked Ti:sapphire lasers[99,105-108]. Further studies of this nature with a high energy, low repetition rate Q-switched laser would be quite interesting and may provide more meaningful results than those obtained here.

Chapter 4

4. Ablation Results for PMMA and PHEMA

4.1 Introduction

PMMA is an acrylic polymer formed by addition polymerization, which has been used in numerous biomedical applications including orthopaedics, dentistry and ophthalmology. In the field of laser vision correction it has commonly been used to calibrate lasers, and has become an industry standard indicator of ablation rate behaviour for corneal tissue using UV lasers. More recently, other materials and techniques have also been used for laser calibration. The ExACT™ test plate comprises a thin micron layer of foil covering a multilayered polymer adherent to a test plastic. Another similar material employs a predetermined amount of white glue adhering foil to a red PMMA sample. Both of these test plates are used for qualitative and quantitative tests of the laser fluence and homogeneity[187]. Despite this, it was still very useful to characterise this material for ablation at 213nm to establish the efficacy of this wavelength.

Another acrylic polymer is PHEMA, which unlike PMMA forms into a hydrogel when hydrated. A hydrogel is defined as any material that can absorb greater than 30% of its own weight in water[170]. At saturation, PHEMA can absorb approximately 38% by weight of water. In terms of biomedical applications in ophthalmology, PHEMA has been used as a material for intraocular lenses[188], soft contact lenses[189] and artificial cornea[190,191]. In the dehydrated state PHEMA is hard and brittle similar to PMMA and becomes soft upon hydration.

PHEMA presented an interesting material for investigation in an ablation study due to the hydrophilic nature of this polymer. Observed differences in the ablation rate between hydrated and dehydrated PHEMA could provide insight into the effect of hydration on ablation rate in corneal tissue. Although corneal hydration has been shown to affect the ablation rate at the 193nm wavelength, similar effects have not been quantified for 213nm.

4.2 Materials and Methods

Ablations were performed on PMMA and PHEMA samples using a prototype version of a refractive solid state laser. The output wavelength of the laser was 213nm and was produced from the fifth harmonic output of an Nd:YAG laser as discussed in chapter 3. The delivery of the laser employed beam smoothing in the form of image rotation. The image rotation was provided from an axially rotating dove prism arrangement. PMMA samples were obtained from in-house stocks (Q-Vis, Perth, W.A) and the PHEMA samples were supplied by the Biomaterials and Polymer Research Department of the Lions Eye Institute, Perth, Australia.

The laser pulse delivered to the target sample had a diameter of 1.0mm, which was set using an adjustable iris controlled through the system software. By varying the system magnification the energy transmitted through the iris could be manipulated. In this way, the fluence value of the laser was varied. For PMMA ablations were carried out using fluence values of 80, 125, 135, 170, 215, 220 and 335mJ/cm^2. Eight fluence values were used for the PHEMA ablations ranging between 75 and 380mJ/cm^2. PHEMA ablations were conducted on both dehydrated and hydrated samples. The samples were immersed in distilled water for 1 week, to ensure hydration to an equilibrium.

The number of laser pulses delivered to each sample was varied between 200 and 1000 pulses in increments of 200. The ablation depth of each cut was then plotted

against pulse number and the gradient of this plot was used to obtain the ablation rate for each value of fluence. Next, a plot of ablation rate versus fluence was produced to give the ablation rate behaviour of each material.

Ablation depth was measured using a light microscope and focusing firstly on a region of the sample outside but adjacent to the ablated area. Microscope focus was then shifted to a point at the base or bottom of the cut. Ablation depth was therefore deemed to be the distance of the microscope focal shift in moving from the top to the bottom of the cut. These measurements were completed using a 40X microscope objective, which determined the resolution of the measurements. The ablation depths of hydrated PHEMA were measured while the samples were still in the hydrogel form.

4.3 Results

For each fluence value investigated, a linear relationship between ablation depth and pulse number was observed. Figure 4.1 displays a plot of the ablation depth versus pulse number for a fluence value of 170mJ/cm^2 in PMMA. The plot of this fluence is shown due to the clinical relevance of this value. Plots of the other fluence values investigated displayed similar characteristics. The data exhibited an excellent correlation to a linear fit (R^2 = 0.99) and the standard error in the gradient (ablation rate) was within 0.3%.

Figure 4.2 is a semi-logarithmic plot of ablation rate with laser fluence for PMMA. The plot reveals that the ablation rate varied from 0.11μm/pulse at a fluence of 80mJ/cm^2 to 0.40μm/pulse at 335mJ/cm^2. For the range of fluence values investigated, the ablation rate data exhibited a strong coherence to the Beer-Lambert law of attenuation. This is illustrated by the best fit trend line also shown in the plot. An estimate of the threshold fluence for ablation was obtained by extrapolating the trend line to the horizontal axis of the plot. This yielded a threshold fluence for ablation of approximately 50mJ/cm^2.

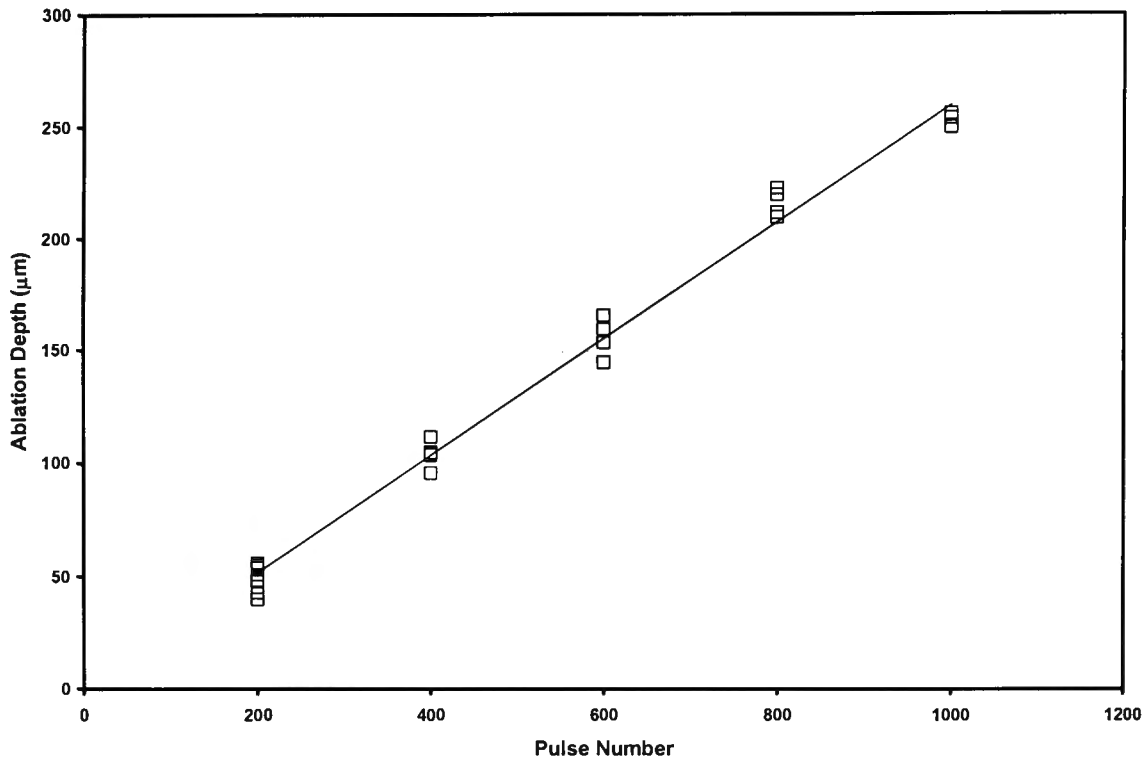

Figure 4.1. Plot of ablation depth as a function of pulse number in PMMA produced using a laser fluence of 170mJ/cm^2. The linear fit of the data yielded a gradient of 0.26μm/pulse.

Figure 4.3 displays the ablation rate results for PHEMA. Both the hydrated and dehydrated samples showed a similar ablation threshold fluence of approximately 60mJ/cm^2. However, the trend lines of each data series revealed the ablation rate of wet PHEMA was approximately 45% higher than the rates obtained for the dry PHEMA samples. This trend was consistent once the fluence was increased beyond 100mJ/cm^2. Both data sets also showed less agreement with the Beer-Lambert model of ablation. Using equation 2.7 of section 2.4.1, calculation of the absorption coefficient for each material yielded values of ~48,000 cm^{-1} (PMMA), ~46,000cm^{-1} (dry PHEMA) and ~31,000cm^{-1} (wet PHEMA).

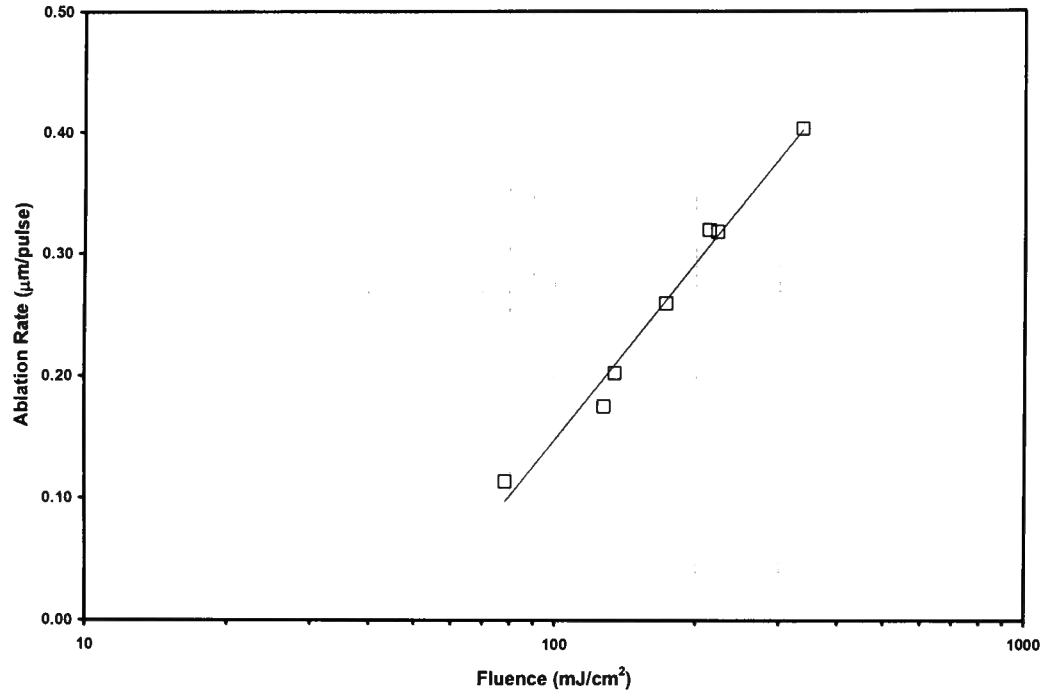

Figure 4.2. Ablation rate versus logarithm of fluence for PMMA.

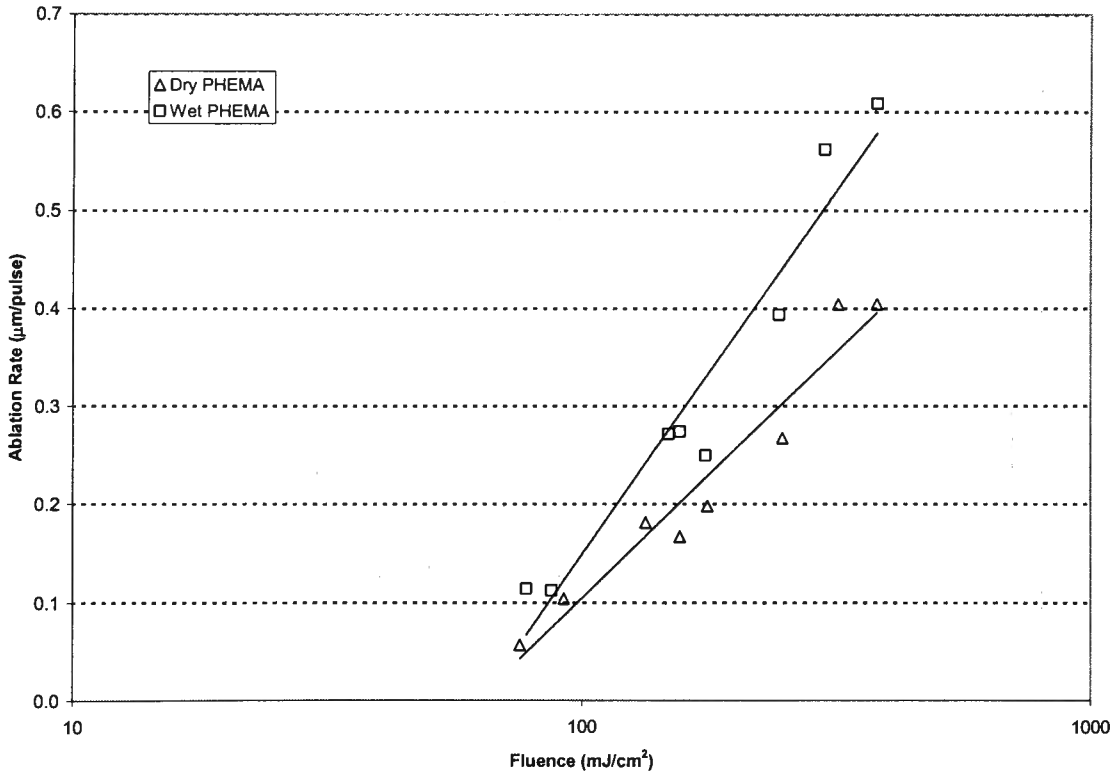

Figure 4.3. Ablation rate versus logarithm of fluence for hydrated and dehydrated PHEMA.

The ablation rate of wet PHEMA was also higher than PMMA. Calculation of the ablation rate from the trend lines of figures 4.2 and 4.3 for a fluence of 170mJ/cm^2

yielded rates of 0.32, 0.26 and 0.22μm/pulse respectively for wet PHEMA, PMMA and dry PHEMA.

From the results of figures 4.2 and 4.3, the ablation efficiency was calculated for each fluence. Plots of ablation efficiency with fluence are shown in figure 4.4 for PMMA and figure 4.5 for PHEMA. For PMMA, the plot showed that the ablation efficiency varied only slightly over the range of fluence values from 80 to 220mJ/cm^2. This region of invariance occurred at an efficiency of approximately 0.15mm^3/J. At the largest fluence value of 335mJ/cm^2 the efficiency decreased to 0.12mm^3/J. The efficiency plot for dry PHEMA exhibited a sharp increase at low fluence values before reaching a peak of just under 0.14mm^3/J at a fluence of 135mJ/cm^2. For larger fluence values, the efficiency tapered slightly before entering a region of plateau at approximately 0.15mm^3/J. Wet PHEMA displayed a similar trend with a peak efficiency of approximately 0.18mm^3/J.

An error analysis performed on each of the calculated points for ablation efficiency are shown in figures 4.4 and 4.5 as error bars. The error in ablation efficiency was obtained by combining the error in ablation rate with the uncertainty of the fluence. The error in the ablation rate was found from the standard error in the linear regression gradient of the ablation depth versus pulse number plot obtained for each fluence. Uncertainty in the measurement of fluence emerged as the dominant quantity in the determination of the combined error.

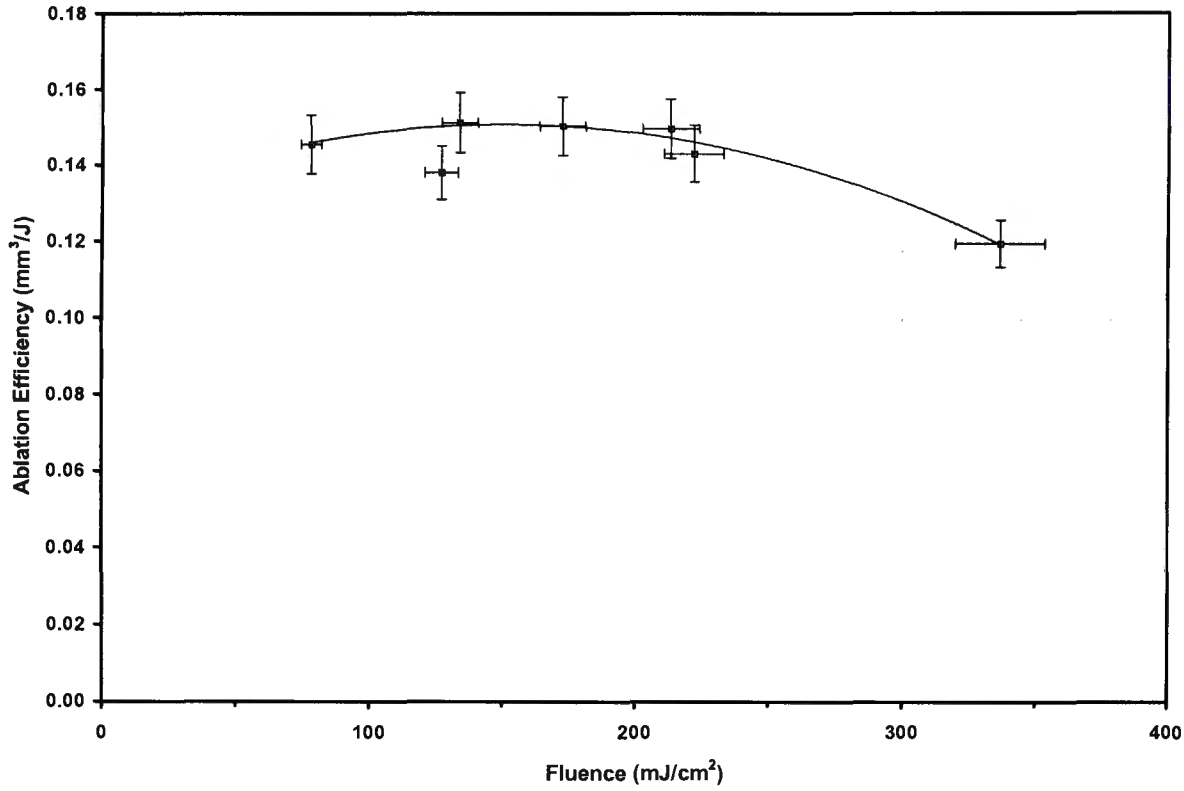

Figure 4.4. Plot of ablation efficiency versus fluence for PMMA.

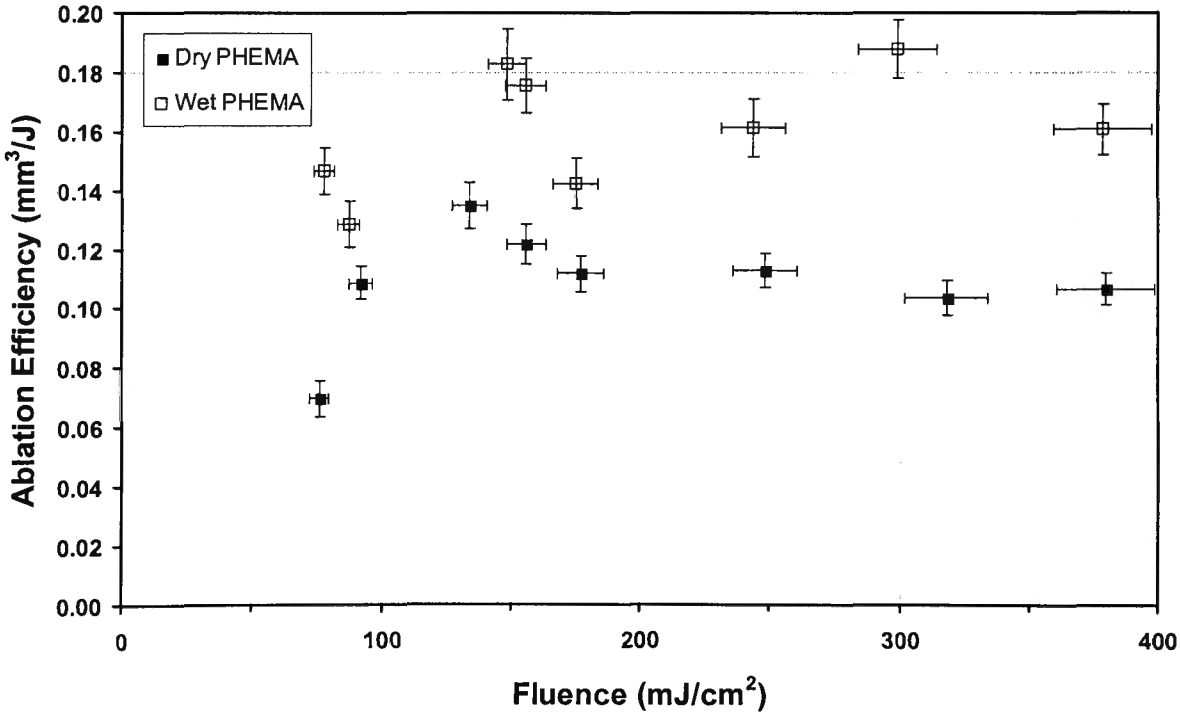

Figure 4.5. Plot of ablation efficiency versus fluence for PHEMA.

4.4 Discussion

For comparison, the data of figure 4.2 for the ablation of PMMA was plotted with data of other investigators and is shown in figure 4.6. The figure shows that the ablation rate results are comparable to those obtained previously for the fluence range investigated. The gradient of the ablation rate curve was within a factor of two of that of the combined data at a wavelength of 213nm (see figure 2.11 on page 50)[156,167,175]. Comparison with previous results at the 193nm wavelength revealed the ablation rate curve was between the data of Fuxbruner[171] and Srinivasan[172] and the gradient value was within 25% of their work.

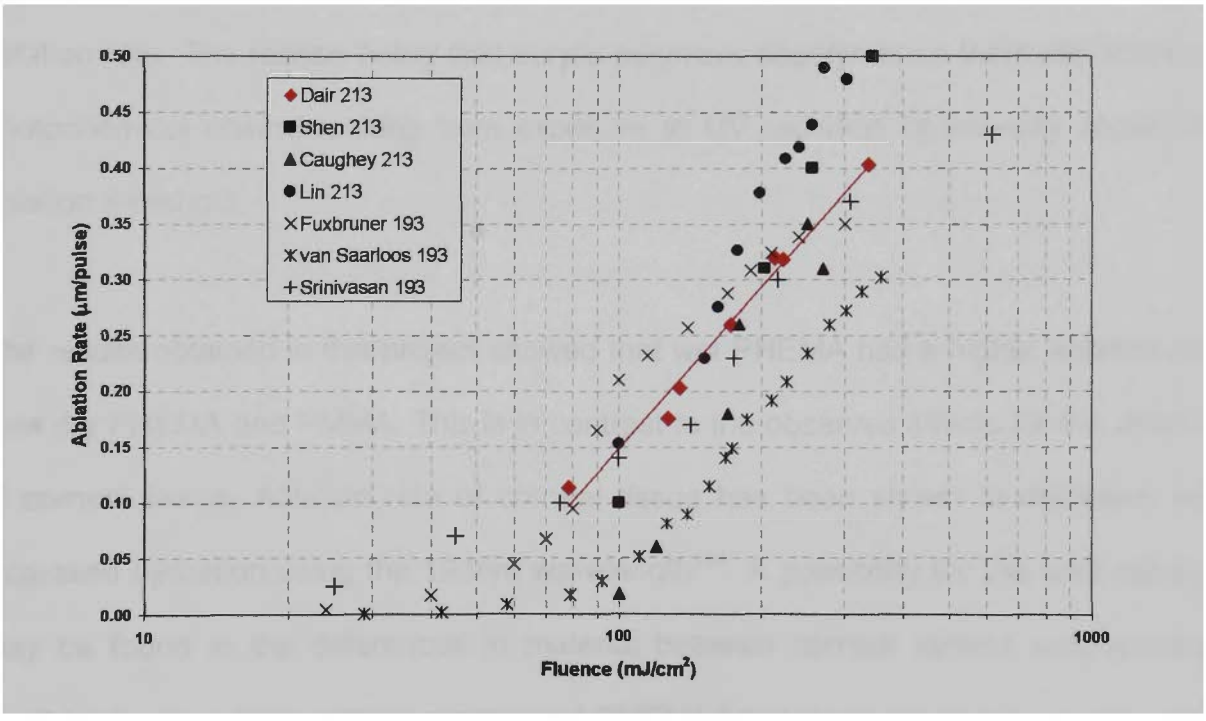

Figure 4.6. Plot of ablation rate data for PMMA by several investigators at both the 193 and 213nm wavelengths[156,167,171-173,175]. Data from the current project is shown in red.

One explanation for the differences observed in the gradients of the ablation rate curves for PMMA with that seen from the literature could be differences in the polymer material. Often PMMA is manufactured with various crosslinking agents such as EGDMA and with varying percentages. Crosslinking alters the physical properties of a

polymer by increasing the resistance of the chemical chains to movement relative to one another[192]. Increasing the percentage of crosslinking agent will render the polymer harder and less flexible.

The effect on ablation rate with different amounts of EGDMA as a crosslinking monomer in PHEMA was investigated by Costela et al[177]. Their study examined the ablation rate of PHEMA containing 0, 1 and 20% EGDMA at three different wavelengths (193, 222, 308nm). The results revealed that the ablation rate decreased with increased crosslinking for a constant fluence. This trend was also observed for each wavelength used. Costela further postulated that the presence of crosslinking material acted to limit the amount of the thermal component that contributed to the ablation rate. The reason being that acrylic polymers depolymerise thermally following photochemical chain breaking from exposure to UV radiation of intensity above the ablation threshold.

The results obtained in this project showed that wet PHEMA had a higher ablation rate than dry PHEMA and PMMA. This is in contrast to the observed effects for the ablation of corneal tissue. Ablation rate of corneal tissue has been shown to decrease with increased hydration using the 193nm wavelength[164]. A possibility for this contradiction may be found in the differences in material between corneal stroma and synthetic acrylic polymers. Both corneal stroma and PHEMA have the capacity to associate with water, however corneal stroma consists primarily of collagen, which is a large protein based molecule[162,193]. Hydration of PHEMA involves bonding of water to the hydrophilic sites within the polymer. This acts to change the structure of the material, which is manifested through swelling and a change of permeability, resulting in the formation of a hydrogel. The bonding process involved in the polymer may result in a weakening of the bonds within the material creating an increased ablation rate. For the larger, more complex structure of collagen, similar bond weakening may not occur.

Although wet PHEMA exhibited an increased ablation rate over dry PHEMA, the results only represent two reference points (corresponding to 0 and 38% hydration). A study involving several levels of hydration would allow a meaningful plot of ablation rate versus hydration to be produced. This would provide a better understanding of the role of hydration on ablation rate.

A more comprehensive study of the effect of hydration on ablation rate was carried out by Feltham and Stapleton[194]. They investigated the ablation rate of HEMA based polymer materials for several values of hydration ranging between 38 and 69%. The highest level of hydration used was closest to that of human corneal tissue, which has been reported to be between 72 to 85%[195]. The various levels of hydration were achieved by using different cross-linking materials within the HEMA. The experiments were conducted using a 193nm wavelength excimer laser. Each of the samples tested showed an increase in the ablation rate between the dry to the wet sample. This trend was consistent with the results of this project. For the hydrated samples however, a decrease in the ablation rate was observed with increasing hydration level.

Corneal hydration certainly has clinical implications on the outcome of corrective refractive surgery, at least for excimer lasers employing a wavelength of 193nm. It may be that in using a polymer to mimic the cornea for evaluating the efficacy of a laser for performing corneal ablation, it would be appropriate to use a material that is hydrated to a level similar to that found physiologically. The issue of hydration in terms of the transmission of UV laser pulses through various solutions is discussed further in chapter 6.

Chapter 5

5. Ablation Results for corneal tissue

5.1 Introduction

The previous chapter dealt with the ablation rate behaviour of the 213nm wavelength solid state laser as applied to the polymer materials; PMMA and PHEMA. Ablation of PMMA using excimer gas lasers has become an industry standard as an indicator of the efficacy of a laser source to perform ablations on the human cornea. It is even more imperative to characterise the ablation rate behaviour of a solid state laser operating in the UV for ablation of corneal tissue. Similarities observed for polymer ablation between excimer and solid state laser sources may not translate to other tissues, such as cornea. Therefore this work forms the precursor for ablation of human corneal tissue.

In particular, this chapter deals with the ablation of porcine cornea. To maintain consistency, a similar study methodology was employed for these experiments involving corneal tissue as for those of the polymer materials. Due to the required immediacy of measuring corneal ablation depth, a novel method involving a confocal microscope arrangement was used, rather than the conventional light microscope utilised in the previous chapter. This measurement method is discussed in detail in section 5.2 (Materials and methods).

The final section of the chapter presents a discussion of the results obtained with comparison to previous work. In addition to ablation rate, the ablation efficiency was also compared with past results using the excimer laser wavelength of 193nm. Based on the experimental data, the region of optimal fluence for ablation was identified.

5.2 Materials and Methods

The laser engine used to perform the ablations upon porcine corneal tissue was similar to the Nd:YAG laser system described in detail in chapter 3, the only difference being that the laser operated at a repetition rate of 10Hz. This was due to the unavailability of a 20Hz laser at the time the experiments were undertaken. All other parameters, as outlined in chapter 3, were otherwise maintained at the prescribed levels.

Ablations were carried out on porcine eyes obtained from an abattoir. All eyes were used within five hours of enucleation and stored on ice until required for ablation. Immediately prior to laser irradiation the epithelium was debrided and the eye vacuum stabilised onto a clamped syringe. The eye was positioned less than 5mm behind a 0.5 × 2.5mm slit onto which the collimated laser beam was centred. Therefore, the slit acted as an aperture for the beam rather than using focusing to produce the required beam diameter. A rectangular slit was chosen to simplify the task of measuring the depth and fluence. The pulse energy through the 1.25mm^2 slit was measured before and after each ablation using a power meter (model 1825-C; Newport, Santa Ana, CA) with a detector (model 818T-10; Newport). A small fan was used during each ablation to disperse the ablation plume to minimise any absorbing or blocking effect this may have had on the impinging laser radiation[128,196].

For each ablation trial, the fluence was held constant, and a number of eyes were ablated with a varying number of pulses. This allowed the ablation rate, defined as the etch depth per pulse to be obtained for a wide range of fluence values. This procedure was repeated for fluence values of 80, 120, 150, 180, 210 and 250mJ/cm^2. The number of pulses was varied between 100 and 400. A separate trial was undertaken to determine the fluence value for the threshold of ablation. The method employed for this trial was to irradiate eyes with low values of fluence and a large number of pulses until a notable etching effect was observed from a profiling system (described below).

In an effort to eliminate potential depth measurement errors associated with histological methods,[116,164] the ablated eyes were analysed immediately following ablation. Surface profiles of the ablated corneas across the 0.5mm cut were measured using a laboratory custom made, computer-automated confocal profiling system. An overview of the system used is shown in figure 5.1. The design of the profiling system was similar to a confocal microscope and had a depth resolution of 10μm. Although the resolution was greater than the submicrometre ablation of each pulse, it was suitable to measure the depth of an ablation resulting from a large number of pulses. Also, a resolution of this magnitude provided a convenient working distance and facilitated surface detection.

Calibration of the profiler was achieved using an interferometric method. This involved utilising the actuator that was used to oscillate the microscope objective to oscillate a plane mirror in one arm of an interferometer. This allowed accurate calibration of the actuator position.

Immediately after irradiation, the eye was placed in the profiler while affixed to the syringe to maintain intra-ocular pressure. The eye and syringe were placed on an x-y translation stage (Newport) and positioned in the beam of the profiler so that it was at the latitudinal centre of the cut. The microscope objective used to focus the beam onto the surface of the cornea was oscillated with a frequency of 25Hz. This enabled the depth measurement at each position across the cut to be averaged over many measurements to minimise error. The profile data were then analysed to obtain the depth of ablation.

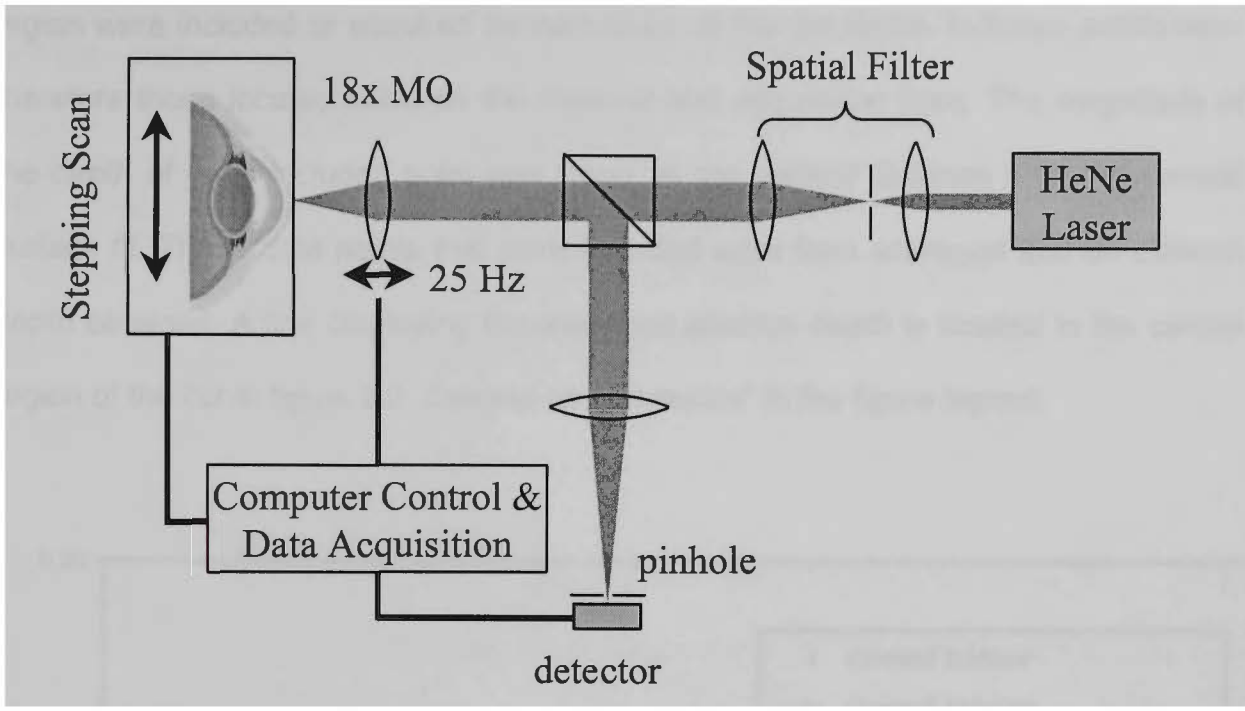

Figure 5.1. Schematic overview of confocal profiling system. MO (microscope objective).

The corneal profile data obtained from the confocal microscope was separated into two data series. The first represented the unablated corneal profile. The second series represented the ablated segment of the cornea. Additional data series were then derived and used in the calculation of ablation depth.

Figure 5.2 shows one such profile of the ablated and unablated segments of the cornea. To obtain a meaningful measurement of the ablation depth, the need arose to extrapolate the unablated curvature of the corneal surface. In this way, the depth could be calculated from the surface extrapolation rather than from a straight line across each edge of the cut. This extrapolated curve was determined by applying a second order polynomial fit to the corneal surface data points. To calculate the depth of ablation, another two polynomials were used. Each of these polynomials were parallel to the fitted curve of the unablated corneal surface. The first was drawn through the deepest point of the ablated region. The second was termed an acquisition line and was heuristically set at 75% of the distance between the surface fit and the deepest

point of the ablation. The acquisition line determined which data points from the ablated region were included or acquired for calculation of the cut depth. Included points were therefore those located between the deepest and acquisition lines. The magnitude of the depth of each included point was taken as the vertical distance from the corneal surface fit. Those data points that were included were then averaged and an ablation depth obtained. A line displaying the averaged ablation depth is located in the central region of the cut in figure 5.2, denoted as "cut centre" in the figure legend.

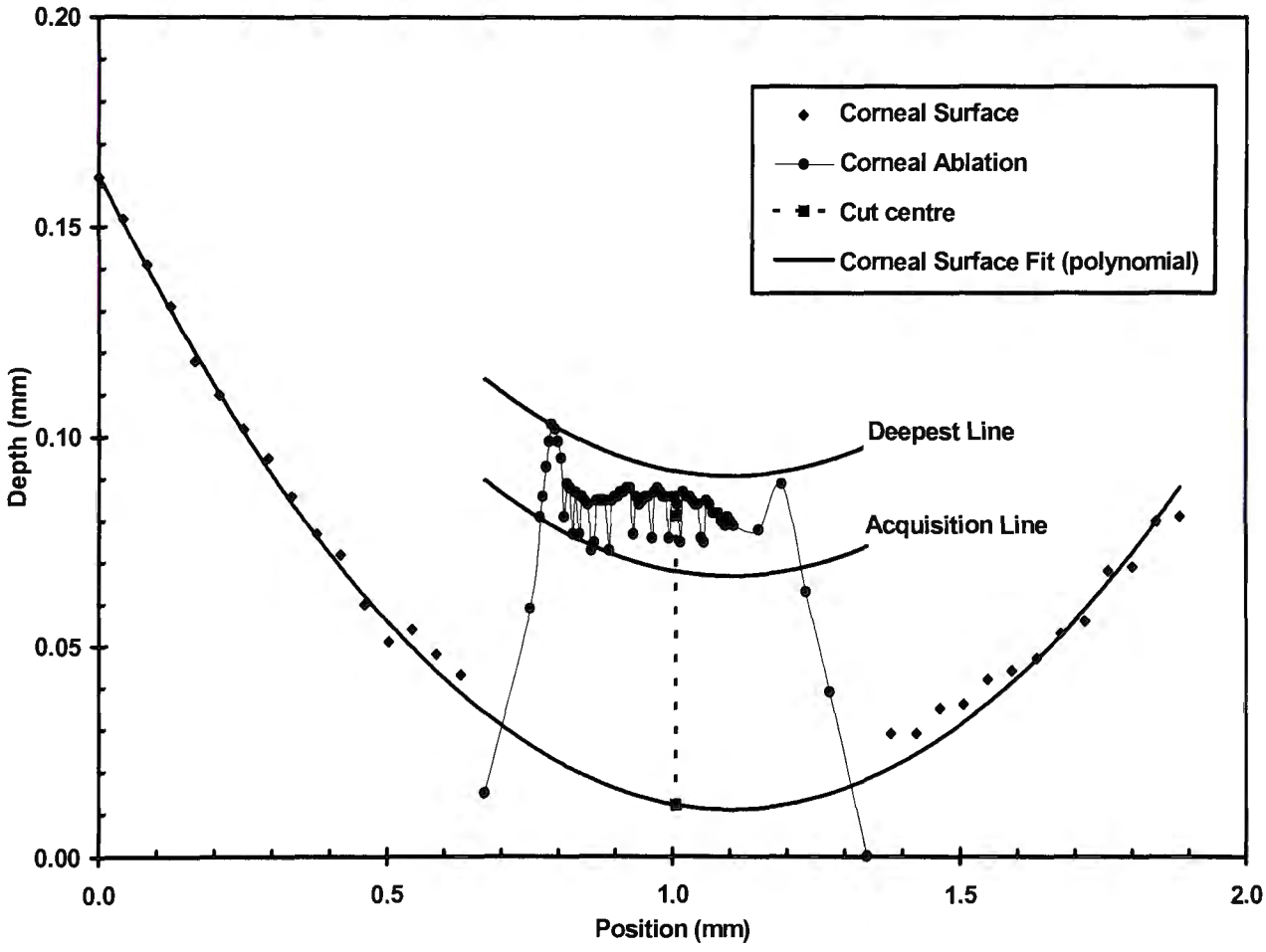

Figure 5.2. Typical confocal ablation profile. Profile represents ablation with 100 pulses at a fluence of 210 mJ/cm^2. Ablation depth for this profile was 69μm yielding an ablation rate of 0.69μm/pulse.

5.3 Results

For the fluence values for which the number of pulses was varied, the etch depth was observed to increase with increasing pulse numbers, yielding a linear relationship between etch depth and number of pulses for constant fluence. For each fluence value, the slope of the linear plot of etch depth versus pulse number was used to obtain the ablation rate in a manner corresponding to that used for the ablation experiments involving polymers (see chapter 4).

Figure 5.3 shows the relationship between ablation rate versus fluence on a semi-logarithmic plot. For the range of fluence values between 80 and 250mJ/cm^2, the plot exhibited agreement with the Beer-Lambert law of ablation. Using the gradient of this data to calculate the absorption coefficient gave a value of 16,870 cm^{-1} (equation 2.7, page 30). The threshold of ablation was found to occur for a fluence of 50mJ/cm^2. This fluence produced a cut depth of 25μm after exposure to 1200 pulses, corresponding to an ablation rate of 0.02μm/pulse. The observed cut depth at this fluence was approximately double the resolution of the confocal profiling system. In the fluence range between 150 and 250 mJ/cm^2, the rate increased to 0.45 and 0.8μm/pulse. From these results, the ablation efficiency was calculated for each fluence.

Ablation efficiency for a given fluence can be obtained by dividing the ablation rate by the value of fluence. The plot of ablation efficiency with fluence is shown in Figure 5.4. The plot reveals that a plateau in the efficiency was reached at a fluence of 150mJ/cm^2. This occurred for an efficiency value of 0.32mm^3/J. For fluences above this value up to the maximum used of 250mJ/cm^2, only a small fluctuation in efficiency was observed between 0.32 and 0.35mm^3/J. In the range from ablation threshold fluence (50mJ/cm^2) up to the fluence where the efficiency reaches a plateau, the efficiency increases steeply, from less than 0.05mm^3/J to 0.32mm^3/J.

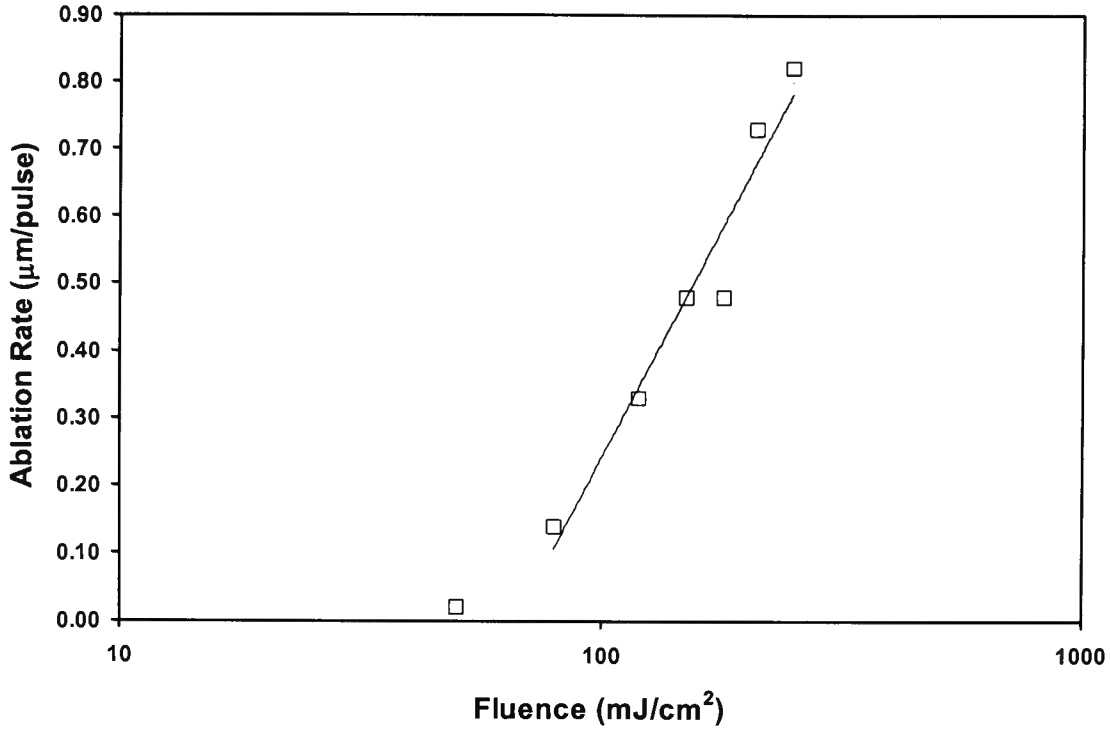

Figure 5.3. Semi-logarithmic plot of ablation rate versus fluence, displaying a linear region for a fluence range of 80 to 250mJ/cm^2.

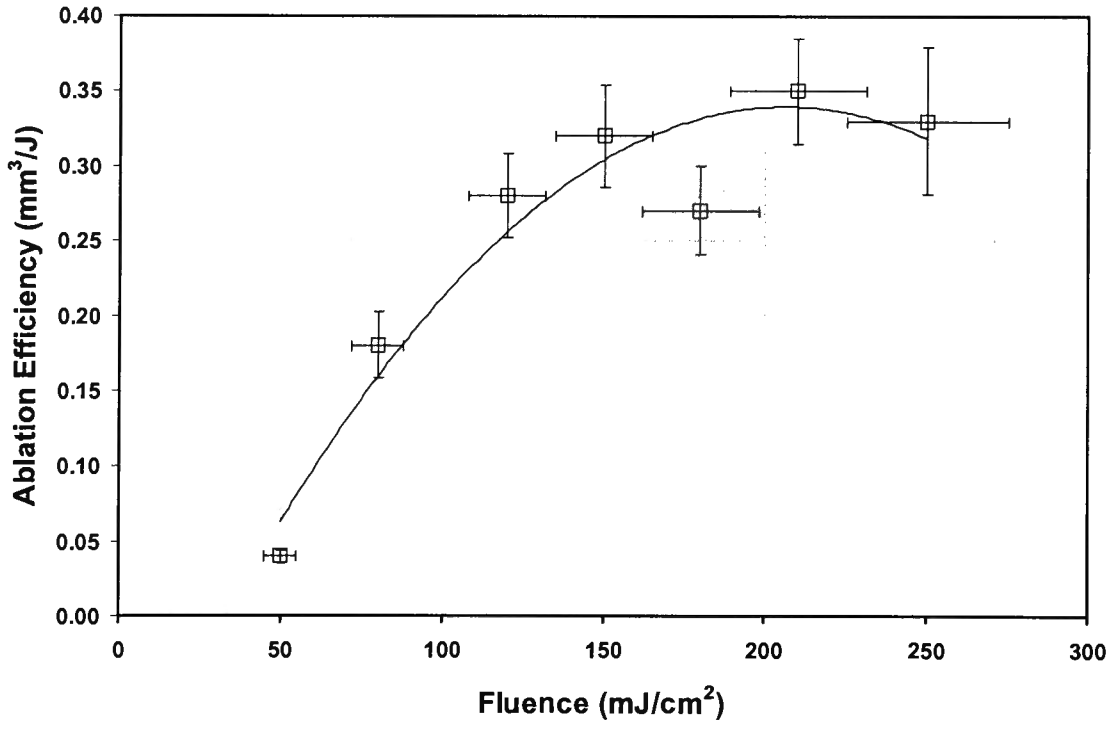

Figure 5.4. Plot of ablation efficiency versus fluence. The plot shows two regions of interest either side of the fluence value 150mJ/cm^2; a steeply increasing function from the ablation threshold fluence and a plateau region for higher fluence values.

A similar error analysis to that performed in section 4.3 for the PMMA and PHEMA ablation efficiency was also undertaken for the corneal tissue data. Results of this analysis are shown in figure 5.4 as error bars.

5.4 Discussion

The absorption of the cornea in the wavelength range from 190nm to approximately 220nm remains relatively constant[118]. This suggests that solid state laser wavelengths in this range could be suitable for performing corneal ablation and achieve ablation rates comparable to that of the excimer laser. Previous ablation studies[116,125] using the excimer wavelength of 193nm reported rates of 0.45μm/pulse at a fluence of 200mJ/cm^2.

An early study by Ren *et al.* [178] using a solid state laser at 213nm used a larger fluence (1.2J/cm^2) than used in this study. The ablation rate was obtained by counting the number of pulses required to perforate the cornea. The laser energy used was 0.4mJ/pulse in a spot size of 0.2mm diameter. The ablation rate at this fluence was estimated to be 0.3μm/pulse. This is a lower rate than obtained in this study even though the fluence value was more than four times the largest fluence used here.

A more recent study by Caughey *et al.* [167] estimated the ablation rate in porcine corneas to be 0.4μm/pulse at a fluence of 200mJ/cm^2. This work was also done at the 213nm wavelength with a maximum pulse energy of 1.1mJ and beam diameters between 0.5 and 1.1mm. Depth analysis was performed by focusing a microscope on the top and bottom sections of the cut. The results obtained here at this fluence show an agreement with this value to within 50%.

These studies revealed that the 213nm wavelength was able to produce tissue ablation with very little damage to the surrounding tissue in a similar fashion to the results

achieved with the 193nm excimer laser. Their observations of surrounding tissue damage were made using histological methods.

Further work by Shen *et al.*[156] on the ablation rate of human cornea at 213nm revealed a similar relationship between ablation rate and fluence to the results of this project. However, the ablation rates at comparable fluence values used in this project were consistently lower. Their study also used perforation of a section of tissue of known thickness to obtain the ablation rate.

The first to investigate the most efficient fluence for operation at the 193nm wavelength were Krueger and Trokel[125]. Ablation rates were found by measuring the number of pulses required to achieve corneal perforation for a wide range of fluences. From these data the fluence for highest efficiency was found by calculating the amount of radiant energy which was required to ablate 100μm of tissue. A refinement to this method was made in later work that quantified ablation efficiency as the volume of tissue removed per unit of input energy[116]. The importance of calculating ablation efficiency can be seen in terms of the amount of energy required to remove a given volume of tissue. A less efficient fluence requires more energy than is necessary to remove the same volume of tissue. As a result, a greater proportion of the energy must be spent on processes other than tissue removal. These processes may be manifest in increased heating of the cornea or a larger shock wave on the surface of the cornea.

The current work characterised the ablation behaviour of the solid state laser (Figure 5.2). The variation of the data in the ablated area suggests that the beam used in this study was not uniform. It should be noted however, that no beam smoothing techniques in the form of image rotation or spatial filtering were used. Next, the ablation efficiency was calculated in a range similar to that used in current clinical excimer lasers. The efficiency was obtained by dividing the ablation rate by the fluence and has units of cubic millimetres per Joule. The results shown in Figure 5.4 suggest that the

efficiency reaches a maximum for fluence values above 150mJ/cm^2. The work done by Krueger *et al* [125] was performed on bovine corneas and found the most efficient fluence for ablation at 193nm was 200mJ/cm^2. Others have found the most efficient fluence to be within the range 150-400mJ/cm^2 [116]. The ablation rate at these fluences was approximately 0.4μm/pulse, which is slightly lower than the value obtained here of 0.48μm/pulse (at 150mJ/cm^2) although within 20%. The fluence value of 180mJ/cm^2 used with some clinical excimer lasers falls within this range (see Table 2.4, page 46).

In addition to the laser parameters used in this study, there is scope to investigate the effect of varying other parameters and the effects this would have on ablation at this wavelength. These include the effects of pulse duration and repetition rate. Pulse duration has been shown to affect ablation threshold. Using a pulse duration of 25ps, Hu and Juhasz[129] observed an ablation threshold fluence of 3mJ/cm^2 in human corneas, which is significantly less than the 50mJ/cm^2 threshold found in the current project. The study by Hu and Juhasz used a wavelength of 211nm and a repetition rate of 1kHz. This repetition rate represents an increase of two orders of magnitude above the 10Hz rate used by many excimer lasers, and it is therefore difficult to quantify the effect. A limited study of the effect of repetition rate on ablation threshold was conducted for rates of 1, 10, and 25Hz by Krueger *et al* [119] using 193nm. The results showed there was no change in ablation threshold over this range. This is yet to be established at even higher rates in the kilohertz regimen and the longer 213nm wavelength.

This study confirms that corneal ablation rates at 213nm are comparable to those achieved with excimer lasers at 193nm for similar pulse duration and repetition rates. A solid state laser with increased energy at 213nm capable of performing large beam ablations may provide an improvement in corneal hydration[164,197] through a reduction in the time required to remove a given amount of tissue.

Chapter 6

6. Transmission Study Results

6.1 Introduction

Chapters 4 and 5 have shown that ablation rates for the wavelength of 213nm are similar to those at 193nm. Notwithstanding this, other factors that may affect ablation rate are yet to be investigated. The ablation rate of corneal tissue depends primarily on the fluence of the laser. The fluence determines the precision and efficiency with which tissue is removed. Two other related factors that have an effect on the ablation rate (at 193nm) are corneal hydration[164,197] and the presence of surface fluids. Fluid on the cornea can result in a reduction of the ablation rate during refractive surgery procedures with 193nm laser pulses[158]. This reduction in ablation rate is evidenced by the high degree of absorption of 193nm light in BSS[198]. Underlying tissue, therefore, is effectively masked from incident radiation[181]. An unknown reduction of the ablation rate can result in under correction of refractive errors or irregular ablations, such as the formation of corneal islands.

During initial patient trials with the 213nm wavelength solid state laser in our institution, it was observed that the presence of fluid on the corneal surface had little effect on the ablation rate. This suggests that while the fluid is a strong absorber for 193nm radiation, it may be a weak absorber for 213nm radiation. The implication is that fluid on the corneal surface during surgery may not have a masking effect for underlying tissue using the 213nm wavelength.

The purpose of the study for this chapter was to quantify the absorption at the 193 and 213nm laser wavelengths in two solutions commonly used during refractive surgery.

The transmission characteristics of each wavelength were investigated through the constituent components of BSS and 0.9% sodium chloride solution. Quantitative values for absorption coefficients were then derived from these data.

6.2 Materials and Methods

The transmission characteristics for each component of BSS were investigated for the ultraviolet wavelengths of 193 and 213nm. Two refractive lasers in clinical use were used for the study. An excimer laser with a pulse duration of 20ns and repetition rate of 10Hz was used to supply the 193nm wavelength. The 213nm radiation was supplied from the fifth harmonic wavelength of an Nd:YAG laser. The pulse duration was 6ns and the repetition rate 20Hz. Pulses from this laser were linearly polarised. The pulse energy of each laser was measured with an energy detector (model ED200; Gentec, Sante-Foy, Quebec) and monitored on a storage oscilloscope. The energy was obtained from the amplitude of the voltage signal delivered from the detector. In order to reduce the error arising from pulse to pulse variations, five pulses obtained randomly were averaged for each measurement.

Figure 6.1 shows the experimental setup used for obtaining the measurements for each wavelength. Solutions were held in a vessel with a fused silica window at the base to maximise transmission. Above the vessel a fused silica beam splitter was utilised in order to allow simultaneous measurement of the initial and transmitted pulse energies. The splitting ratio of the beam splitter was measured at each wavelength to allow calculation of the pulse energy incident on the solution. The reflection losses at each interface through the vessel were also calculated. This included the air-solution, solution-fused silica and fused silica-air boundaries that are encountered during a single pass through the vessel. For 193nm and 213nm, the refractive index of the solution was taken to be 1.436 and 1.409, respectively[199]. The overall reflection losses were 8.0% for 193nm and 7.4% for 213nm.

Solutions containing various concentrations of each species were tested for transmission. The depth of solution was maintained at a fixed level of 17.5mm by placing an equal volume of solution in the vessel for each concentration. This corresponded to the use of 10ml of solution. Species investigated were based on the recipe used for BSS (Alcon, New South Wales, Australia) and included sodium chloride, potassium chloride, calcium chloride, magnesium chloride, sodium acetate and sodium citrate. Each solution was prepared by diluting with deionised water. The range of concentrations used varied between the concentration found in BSS for each species down to a dilution factor of 1/200. A further range was used in the case of the chlorides for 213nm, which was in excess of the molarities found in BSS. This was necessary for 213nm because none of these species produced a detectable change in transmission for the concentration range used at 193nm. Higher concentration ranges were used for sodium chloride (1-5mol/L), potassium chloride (0.5-4mol/L), and calcium and magnesium chlorides (0.5-2mol/L) to produce an appreciable attenuation.

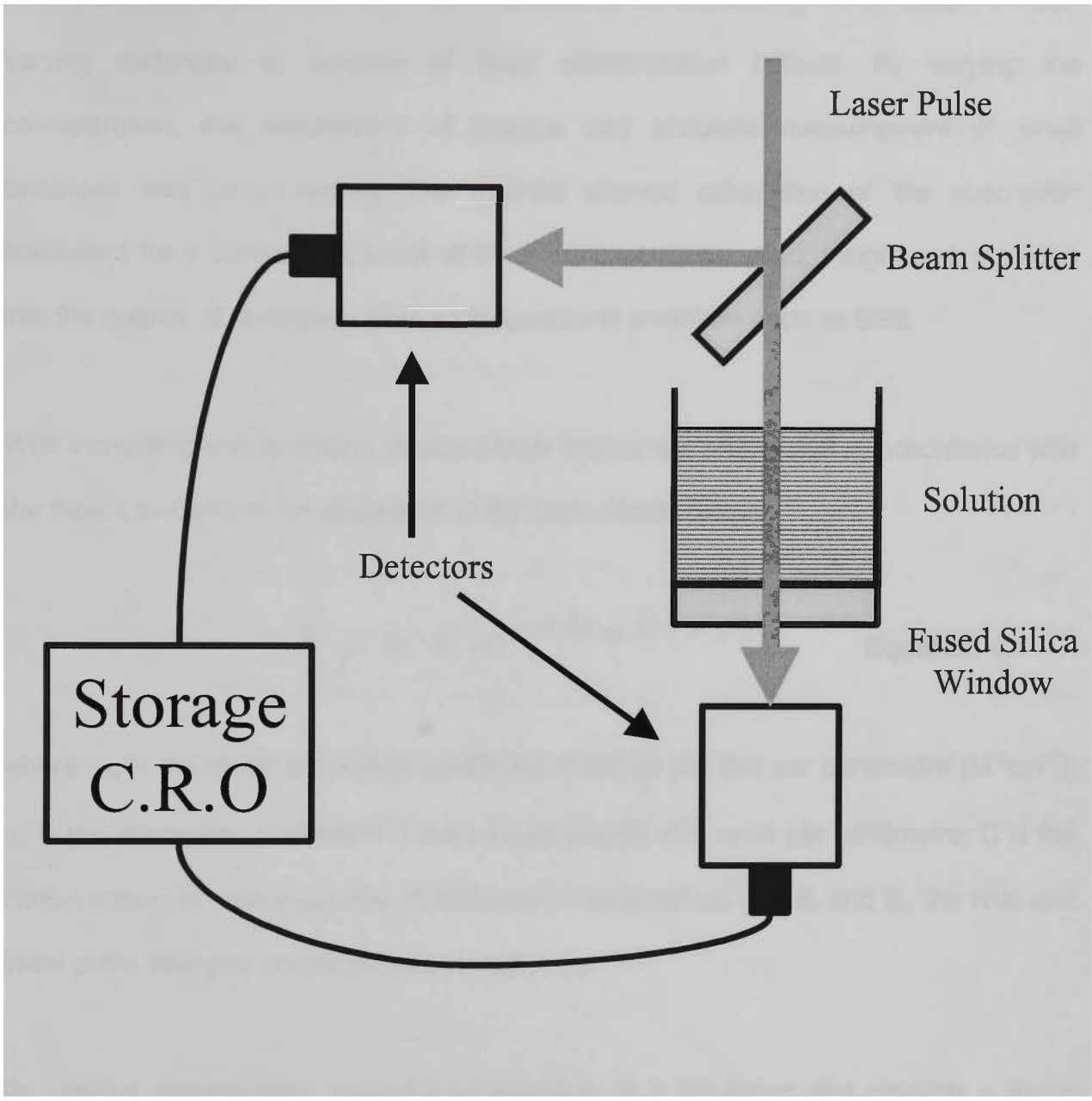

Figure 6.1. Experimental setup for measuring transmission of 193nm excimer and 213nm solid state laser pulses through various solutions. Reflection losses through the vessel were 8.0% for 193nm and 7.4% for 213nm pulses.

The method of varying concentration was employed due to the large degree of absorption observed at 193nm for sodium chloride solution and BSS. This large absorption made the more conventional method of measuring transmission through varying distances of solution of fixed concentration difficult. By varying the concentration, the requirement of precise and accurate measurement of small distances was circumvented. The method allowed calculation of the absorption coefficient for a particular species at other concentrations. Also, insight was provided into the degree of absorption from each species in a mixture such as BSS.

With increasing concentration, incident laser pulses are attenuated in accordance with the Beer-Lambert law for absorption of the form shown below:

$$E_f = E_i e^{-d(\alpha_M C + \alpha_s)} \qquad \textbf{Equation 6.1}$$

where α_M is the molar absorption coefficient in moles per litre per centimetre ($M^{-1}cm^{-1}$); α_s is the absorption coefficient of the solvent (water) with units per centimetre; C is the concentration in moles per litre; d, distance in centimetres; and E_f and E_i, the final and initial pulse energies (in millijoules), respectively.

By plotting transmission against concentration in a log-linear plot yielding a linear relationship, the gradient of the plot was used to obtain the molar absorption coefficient of each species. Multiplication of the molar absorption coefficient (α_M, $M^{-1}cm^{-1}$) with concentration produces the absorption coefficient for a given molarity (α, cm^{-1}). The distance over which 63% of the incident energy is absorbed is defined as the penetration depth and is obtained from the reciprocal of the absorption coefficient.

The absorption coefficient for each species at the molarity occurring in BSS was calculated for each wavelength. By summing the absorption coefficients from each species, an overall absorption coefficient for BSS was obtained. In this way, the

penetration depth for each species and BSS was found. The absorption coefficient and penetration depth was also found for 0.9% sodium chloride solution.

6.3 Results

Transmission was found to decrease exponentially with increasing concentration for all species tested. Figure 6.2 shows a log-linear plot of the transmission data for sodium chloride depicting a linear relationship at 193nm. Similar plots were created for each species. These data obtained at 213nm for this range of concentrations are also shown. No attenuation was detected over this range for this wavelength. Data obtained at 213nm for sodium chloride at the higher concentration range of 1.0 to 5.0mol/L are shown in figure 6.3. The gradient of each plot was used to calculate the molar absorption coefficient. Table 6.1 presents the results obtained for each species and wavelength. The largest molar absorption coefficient was found to occur in sodium citrate for each of the wavelengths tested. However, for the 193nm wavelength, the coefficient was larger by an order of magnitude. Similarly, sodium chloride showed the lowest coefficient for each wavelength, although the value for 193nm was four orders of magnitude larger.

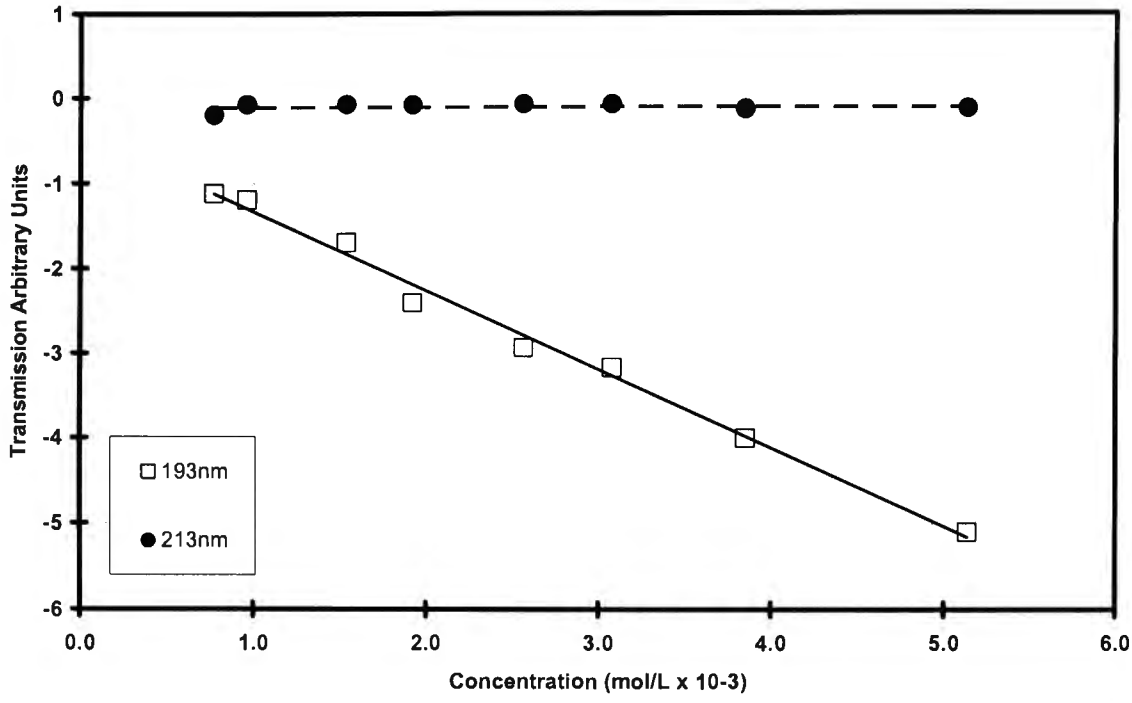

Figure 6.2. Semi-logarithmic plot of transmission in sodium chloride solution versus concentration for 193 and 213nm. Solution path length is 17.5mm.

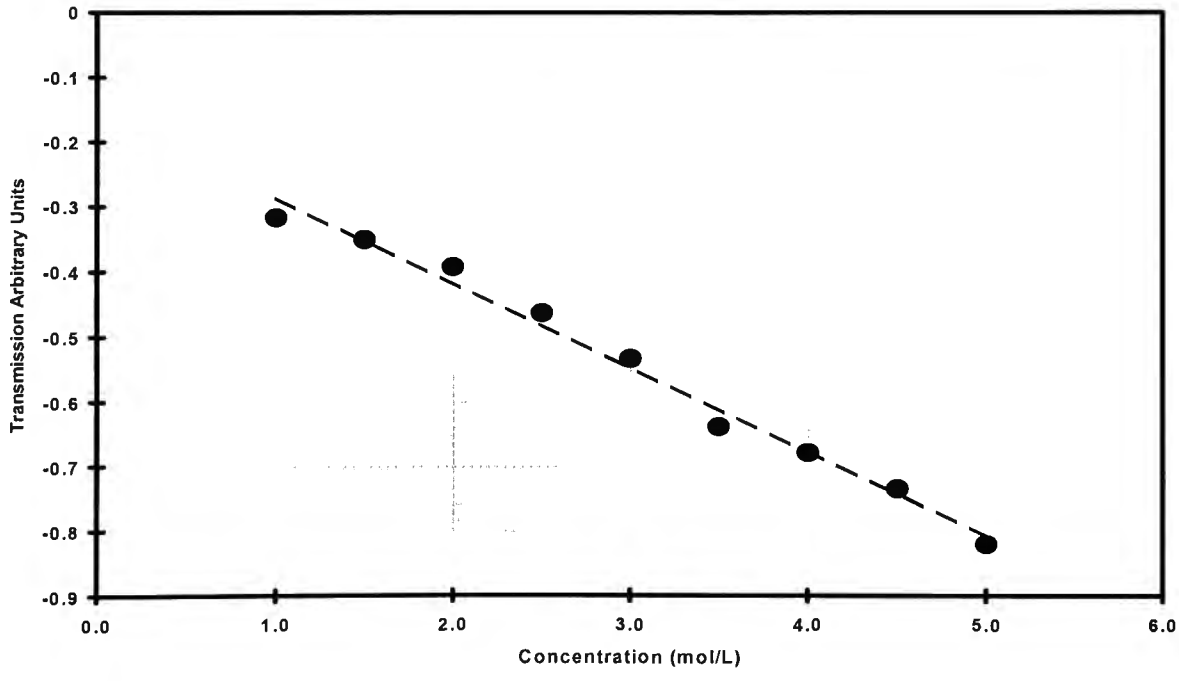

Figure 6.3. Semi-logarithmic plot of transmission in sodium chloride solution versus concentration for 213nm. Solution path length is 17.5mm. Note the different units for concentration from that of Figure 6.2.

Absorption coefficients and molarity for each substance found in BSS are shown in Table 6.2. The penetration depth calculated for each component is also presented in Table 6.2. While sodium chloride had the lowest molar absorption coefficient for 193nm, the relatively large concentration used in BSS means it showed the shortest penetration depth (173μm). Conversely, magnesium chloride exhibited the longest penetration depth (5010μm) due to the low value of concentration and despite a molar absorption coefficient comparable to calcium chloride and sodium acetate.

Species	α_M ($M^{-1}cm^{-1}$)	
	193nm	**213nm**
Sodium Chloride	527	0.07
Potassium Chloride	673	0.19
Calcium Chloride	1588	0.31
Magnesium Chloride	1349	0.15
Sodium Acetate	1145	58
Sodium Citrate	6070	899

Table 6.1. Molar absorption coefficient(α_M) results.

For 213nm, sodium acetate and, in particular, sodium citrate were responsible for the observed absorption at this wavelength. The contribution to the absorption from the four chloride solutions was negligible by comparison. The absorption due to sodium citrate was relatively weak compared with that of 193nm, exhibiting a penetration depth of almost 2mm compared with approximately 0.3mm for 193nm.

Species	Molarity in BSS (mol/L x 10^{-3})	193nm		213nm	
		α (cm^{-1})	Penetration depth (μm)	α (cm^{-1})	Penetration depth (μm)
Sodium Chloride	109.51	57.7	173	0.008	1.2×10^{6}
Potassium Chloride	10.06	6.8	1477	0.002	5.2×10^{6}
Calcium Chloride	3.27	5.2	1926	0.001	9.9×10^{6}
Magnesium Chloride	1.48	2.0	5010	0.0002	4.5×10^{7}
Sodium Acetate	28.67	32.8	305	1.7	6019
Sodium Citrate	5.78	35.1	285	5.2	1925

Table 6.2. Absorption coefficients (α) and penetration depths for components of BSS.

Table 6.3 displays results for absorption coefficient and penetration depth in BSS, 0.9% sodium chloride solution, and water. The results for water were included to provide a basis for comparison and were taken from the literature[151]. Calculation of α_s from equation 6.1 for pure water produced values of 0.17 and $0.02cm^{-1}$ for the 193 and 213nm wavelengths, respectively. Although these values are of similar magnitude to the literature values ($0.12cm^{-1}$ for 193nm and $0.04cm^{-1}$ for 213nm), they should be accepted with caution. This is because the calculation represents the absorption through only a single data point or depth of solution. To properly characterise the absorption coefficient for water, a more rigorous method incorporating several depths should be used.

The molarity of 0.9% sodium chloride solution (0.154mol/L) is approximately 40% higher than the molarity of sodium chloride in BSS (0.11mol/L). The results of Table 6.3 show that the penetration depth in BSS for the 213nm wavelength is longer than 193nm by a factor of 20. In the 0.9% sodium chloride solution, the penetration depth for 213nm is three orders of magnitude longer than that obtained for 193nm.

Solution	193nm		213nm	
	α (cm^{-1})	Penetration Depth (μm)	α (cm^{-1})	Penetration Depth (μm)
BSS (Alcon)	140	72	6.9	1450
0.9% Saline	81	123	0.05	2.0×10^5
Water†	0.12	8.3×10^4	0.04	2.5×10^5

Table 6.3. Absorption coefficients (α) and penetration depths for various fluids. †Data obtained from Hale and Querry[151].

6.4 Discussion

By obtaining the molar absorption coefficient for the various components used in the production of BSS, the penetration depth can be calculated for any concentration of a particular species or for a mixture of species. For sodium chloride, this allows the comparison of penetration depths for solutions of varying molarity. BSS contains 0.64% sodium chloride (0.11 mol/L), which is a lower concentration than that of 0.9% sodium chloride solution (0.154 mol/L).

A study by Kornmehl and coworkers[181] on the masking properties of various fluids suggested that 0.9% sodium chloride solution (saline) exhibits significant absorption at 193nm and negligible absorption for 213nm. The study did not however, calculate any absorption coefficients. Absorbance was shown in relative terms over a spectrum of wavelengths between 190 and 240nm. This trend for the two wavelengths investigated in this project is consistent with these results.

Another study by Keates et al.[198] investigated the absorption coefficient of BSS for the 193 and 308nm wavelengths. Experiments were performed by measuring the

transmission through an increasing thickness of solution. For 193nm, the total thickness of solution was 200μm. These data yielded an absorption coefficient of $145cm^{-1}$ for a penetration depth of 69μm. This value agrees to within 5% for results obtained here in BSS at 193nm.

For each trial, the transmission through pure water was measured initially corresponding to a concentration of zero. At 193nm, an average transmission of 75% was observed; for 213nm, the average transmission was 96%. These transmission values are predicted in data by Hale and Querry,[151] who tabulated absorption coefficients for water over a broad spectral range. For 193nm, an absorption coefficient of approximately $0.12cm^{-1}$ was calculated. The depth of solution used in this study of 17.5mm would produce approximately 80% transmission through pure water based on this value for the absorption coefficient. For 213nm, Hale and Querry calculated an absorption coefficient of $0.04cm^{-1}$, resulting in approximately 93% transmission for the experiments of this project. For each wavelength, the readings obtained here corresponded to within 50% to the findings of Hale and Querry.

The above findings may have implications for refractive laser surgery. Corneal hydration has been shown to be an important factor in determining refractive outcome following laser surgery at the 193nm wavelength[200,201]. Dougherty et al[164] showed that ablations carried out on dehydrated cornea resulted in over correction of the refractive error. Similarly, superhydration of the cornea produced an under correction of the refractive error. More predictable results were achieved with corneas at a physiological level of hydration. In addition to this, work by Campos et al[202] examined the effects of using a nitrogen gas blower to remove the ablation plume. The study found that the gas acted to dehydrate the cornea and an irregular ablated surface resulted. For ablations performed without the presence of the nitrogen gas, the ablated surface appeared smooth. Subsequent work, however, showed that corneal hydration could be better controlled by employing humidified gases to remove the ablation plume[203]. These

points suggest that corneal hydration should be closely monitored during refractive surgery. Corneal hydration is often controlled during surgery by the topical application of BSS and removal of excess surface fluid. A possible consequence of the long penetration depth of this fluid at 213nm compared 193nm could be a relaxation of the close monitoring requirement of corneal surface fluid.

The use of BSS or sodium chloride solution also has application for phototherapeutic keratectomy procedures as a masking agent for 193nm lasers. Phototherapeutic keratectomy is used to treat corneal irregularities and protuberances. The role of a masking fluid is to shield deeper lying areas of tissue while exposing the corneal irregularities to the incident laser radiation. This results in a smooth and regular postoperative corneal surface. A range of masking fluids have been used for this procedure[181,182,204] in addition to BSS[205]. Desirable properties of a masking agent for phototherapeutic keratectomy include moderate viscosity and high absorbance[181]. The results obtained in this project show that the solid state laser wavelength of 213nm is weakly absorbed in BSS and 0.9% sodium chloride solution compared with the 193nm excimer laser wavelength. The increased penetration depth of the 213nm wavelength may affect the suitability of these solutions as masking fluids for phototherapeutic keratectomy procedures.

It is worth noting that the penetration depths for the fluids investigated are large compared with the corneal tear film thickness (5 – 10μm). The tear film however, is a complex solution comprising a variety of substances including proteins and enzymes[206] and therefore a meaningful comparison with the simple solutions examined in this project was not possible.

The results of this study reveal the difference in absorption coefficient for BSS at the 193 and 213nm laser wavelengths, which could have implications for both refractive and therapeutic laser procedures. For phototherapeutic keratectomy, other solutions

used as masking agents at 193nm should be investigated for suitable absorption before being used at the longer solid state laser wavelength. In terms of refractive procedures, the possibility that BSS or sodium chloride solution have little effect on the corneal ablation rate may translate to a less stringent monitoring requirement of excess fluid on the cornea. This should, however, be verified with an ablation rate study incorporating known levels of surface fluid on the cornea.

Chapter 7

7. Conclusions

The two laser systems investigated in the course of this project yielded varying results in terms of being able to generate wavelengths in the UV. The Nd:YAG laser based system proved to be the most efficacious and stable, and provided enough UV energy to complete the later experiments of the project. On the other hand, the Ti:sapphire laser based system did not appear to be a viable option for generating UV harmonic wavelengths. This was at least the case with the chosen harmonic conversion scheme. After the initial characterisation of the system, this laser was excluded from the later experiments of the project involving material ablation and fluid transmission.

The experiments of chapters 4 and 5 on the ablation of polymer material and porcine corneal tissue showed that these materials could be etched with a degree of precision suitable for ophthalmic applications. A preliminary investigation into the effect of hydration on ablation rate was undertaken for PHEMA. Corneal hydration is an important factor in determining the outcome of refractive surgery.

The differences observed in the work for the transmission of the solid state 213nm wavelength through BSS and sodium chloride solution were not borne out in the ablation results for PHEMA. The increased ablation rate obtained from the dry to the wet PHEMA samples was in contradiction to the postulated theory based on the transmission study results. One would have expected very little change in the ablation rate of the hydrated samples if the 213nm wavelength radiation was not influenced by hydration.

The results of the transmission studies showed that the solid state laser wavelength of 213nm was weakly absorbed in BSS and 0.9% saline solution compared to the 193nm excimer laser wavelength. The increased penetration depth of the 213nm wavelength in these solutions certainly has implications for phototherapeutic applications using BSS as a masking agent. Also, it may translate into an independence of the corneal ablation rate to corneal hydration. This could provide an improvement to the predictability of results for refractive surgery procedures. Although this idea was not supported by the initial results for the ablation of hydrated PHEMA samples, further work on the potential effect this weak absorption may have on the corneal ablation rate and refractive outcome is required. An ablation rate study incorporating known levels of surface fluid on the cornea or using PHEMA samples at several different levels of hydration could achieve this task.

7.1 Future studies

A great deal of scope exists for continuation of the current work, both in the areas of solid state laser development and in characterising the ablative behaviour of the various wavelengths. A thorough investigation of the role of pulse duration on the ablation process in the deep UV region would be of great interest. A systematic study incorporating femto-, pico-, and nano-second pulses in the UV has never been completed. A number of problems exist for achieving this. Harmonic generation of ultra-short pulses is difficult due to the effects of group velocity dispersion. Laser systems achieving pico- and femto-second pulses in the UV generally exhibit repetition rates of several kilo-Hertz and pulse energies of a few nano-Joules. This is because ultra-short pulse durations are achieved through mode locking of the laser cavity. Development of a mode locked laser with a low repetition rate (tens of Hertz) could however, be accomplished with current pulse selecting technology. Also, amplification of the pulse energy may be required if a pulse duration study was to be undertaken in order to keep

the repetition rate and energy constant across the three pulse regimes. These laser systems tend to be quite complex and so far have been restricted to the laboratory.

Also, other laser sources may be investigated. Recently, high quality laser rods of Cr:LiCAF and Cr:LiSAF have become commercially available. These rods exhibit properties making them more suitable for flashlamp pumped operation while having a broadly tunable output wavelength in the near IR (720 – 920nm). These properties may prove more appropriate for fourth harmonic generation than we were able to achieve with an arrangement involving Ti:sapphire. One could then attempt to perform studies in the wavelength range between 193 and 213nm, which have been the two fixed wavelengths investigated in this and other studies.

Another recent innovation in laser rod technology may provide an alternative to the Nd:YAG laser. Neodymium doped potassium – gadolinium – tungstate (Nd:KGW) laser rods combine a similar wavelength (1067.2nm) with a lower pumping threshold for laser action. Another favourable characteristic of this material is a larger emission bandwidth. This allows shorter pulse durations to be achieved than currently accomplished with Nd:YLF or Nd:YAG lasers.

Recent developments in corneal ablation techniques have focused on intra-stromal ablation. These lasers use an infra red pulse from a mode locked laser source, such as Nd:Glass or Nd:YLF, with a duration of several picoseconds. Such devices have been used commercially for corneal flap preparation as part of LASIK procedures in a way similar to current microkeratome technology. Although relatively expensive compared to a microkeratome, the performance of a complete LASIK procedure using only a laser, may become a reality in the next few years.

Also, the availability of reliable and robust optical parametric oscillator devices could signal a resurgence in interest for corneal ablation using the 2.94μm wavelength. This

wavelength was investigated using Er:YAG lasers with limited success due to the problems associated with obtaining nano-second output pulses from this laser. A parametric oscillator pumped by an Nd:YAG laser is able to overcome this as the resulting output pulse duration is governed by that of the pump laser.

In terms of UV pulse production using nonlinear harmonic generation, the crystal CLBO is still a relatively recent innovation. Further work involving this harmonic scheme should lead to refinements in handling and control of these crystals. This could take the form of fully characterising the temperature dependence of the refractive indices as well as the possibility of using index matching fluid to maintain a controlled, homogenous environment for the crystals. Improvements to the crystal lifetime and consistency of performance could have a very large impact in the commercial arena. Also, the possibility of a new crystal being developed with even more favourable properties for UV harmonic generation than CLBO should not be discounted.

The mechanism of ablation remains largely misunderstood and the absorption coefficient of corneal tissue is also still being debated. Although it may be argued that these are of interest purely from a scientific viewpoint, deeper knowledge of the ablation mechanism has the potential to lead to improvements in algorithm design for performing custom ablations and in the emerging wavefront technology.

In addition to the ophthalmic applications discussed for pulsed UV lasers, several other applications warrant investigation in this wavelength regime. Medical applications involving liver, bone and cardiovascular tissue may prove interesting. Dental applications using UV lasers have also been investigated in recent times.

8. References

1. Maiman TH. Stimulated optical radiation in ruby. Nature. 1960;187:493-494.

2. Sliney DH. Safety of ophthalmic excimer lasers with emphasis on compressed gases. Refract Corneal Surg. 1991;7:308-314.

3. Mori Y, Kuroda I, Nakajima S, Sasaki T, Nakai S. New nonlinear optical crystal: Cesium lithium borate. Appl Phys Lett. 1995;67:1818-1820.

4. Srinivasan R. Ablation of polymers and biological tissue by ultraviolet lasers. Science. 1986;234:559-565.

5. Svelto, O. Principles of Lasers. Fourth Edition. 1998. Plenum.

6. Marshall J, Trokel SL, Rothery S, Krueger RR. A comparative study of corneal incisions induced by diamond and steel knives and two ultraviolet radiations from an excimer laser. Br J Ophthalmol. 1986;70:482-501.

7. Barnes NP, Gettemy DJ, Esterowitz L, Allen R. Comparison of Nd 1.06 and 1.33μm operation in various hosts. IEEE J Quantum Electron. 1987;23:1434-1451.

8. Koechner W. Solid State Laser Engineering. Third Edition. 1992. Springer-Verlag.

9. Markiewicz JP, Emmett JL. Design of flashlamp driving circuits. IEEE J Quantum Electron. 1966;2:707-711.

10. Holzrichter JF, Emmett JL. Design and analysis of a high brightness axial flash lamp. Appl Opt. 1969;8:1459-1464.

11. Perlman DE. Characteristics and operation of Xenon filled linear flashlamps. Rev Sci Instrum. 1966;37:340-343.

12. An overview of flashlamps and cw arc lamps. Technical Bulletin 3. 1995. ILC Technology.

13. Siegman AE. Lasers. 1986. The Maple-Vail Book Manufacturing Company.

14. Benson RC, Mirarchi MR. The spinning reflector technique for ruby laser pulse control. IEEE Trans Milit Electr. 1964;8:13-21.

15. Kafalas P, Masters JI, Murray EME. Dye cell Q-switching. J Appl Phys. 1964;35:2350.

16. Soffer BH. Giant pulse laser operation by a passive, reversibly bleachable absorber. J Appl Phys. 1964;35:2551.

17. Chesler RB, Geusic JE, Karr MA. A practical, high repetition rate Q-switched Nd:YAIG laser. IEEE J Quantum Electron. 1969;5:345.

18. Continuum Surelite. 2001. <http://www.continuumlasers.com/resmains>

19. High Power Pulsed Nd:YAG Laser. (2001). <http://www.spectronlasers.com/ >

20. Quanta-Ray PRO Series Pulsed Nd:YAG. 2001. Spectra Physics. <http://www.spectra-physics.com/products/isl_products/labandpro.html>

21. Herbst RL, Komine H, Byer RL. A 200mJ unstable resonator Nd:YAG oscillator. Opt Commun. 1977;21:5-7.

22. Byer RL, Herbst RL. The unstable resonator YAG. Laser Focus 14(7), 48-57. 1978.

23. De Silvestri S, Laporta P, Magni V, Svelto O. Solid-state laser unstable resonators with tapered reflectivity mirrors: The super-gaussian approach. IEEE J Quantum Electron. 1988;24:1172-1177.

24. De Silvestri S, Laporta P, Magni V, Valentini G, Cerullo G. Comparative analysis of Nd:YAG unstable resonators with super-gaussian variable reflectance mirrors. Opt Commun. 1990;77:179-184.

25. De Silvestri S, Laporta P, Magni V, Svelto O, Majocchi B. Unstable laser resonators with super-gaussian mirrors. Opt Lett. 1988;13:201-203.

26. De Silvestri S, Magni V, Svelto O, Valentini G. Lasers with super-gaussian mirrors. IEEE J Quantum Electron. 1990;26:1500-1509.

27. Hodgson N, Bostanjoglo G, Weber H. The near-concentric unstable resonator (NCUR) - an improved resonator design for high power solid state lasers. Opt Commun. 1993; 99:75-81.

28. Magni V, De Silvestri S, Qian L-J, Svelto O. Rod-imaging supergaussian unstable resonator for high power solid-state lasers. Opt Commun. 1992;94:87-91.

29. Parent A, Lavigne P. Increased frequency conversion of Nd:YAG laser radiation with a variable-reflectivity mirror. Opt Lett. 1989;14:399-401.

30. Moulton PF. Ti-doped sapphire: tunable solid-state laser. Opt News. 1982;8:9.

31. Kneipp H, Kolenda J, Rairoux P et al. Ti:Sapphire laser based lidar systems. SPIE. 1992;1714:270-278.

32. Pinto JF, Esterowitz L, Rosenblatt G, Kokta M, Peressini D. 55% Increase in Ti:Sapphire Laser Slope Efficiency with New High Figure of Merit Crystals. 728-729. 1992. IEEE Lasers and Electro-Optics Society.

33. Blair RJ, Hauck J. Energy scaling of flashlamp pumped Titanium Sapphire lasers. SPIE. 1993;1864:78-85.

34. Carts YA. Titanium sapphire's star rises. Laser Focus World. 1989;9:73-88.

35. Spence DE, Kean PN, Sibbett W. 60-fsec pulse generation from a self-mode-locked Ti:sapphire laser. Opt Lett. 1991;16:42-44.

36. Squier J, Salin F, Mourou G, Harter D. 100-fs pulse generation and amplification in Ti:Al_2O_3. Opt Lett. 1991;16:324-326.

37. Asaki MT, Huang C-P, Garvey D, et al. Generation of 11-fs pulses from a self-mode-locked Ti:sapphire laser. Opt Lett. 1993;18:977-979.

38. Zhou J, Huang C-P, Murnane MM, Kapteyn HC. Amplification of 26-fs, 2-TW pulses near the gain-narrowing limit in Ti:sapphire. Opt Lett. 1995;20:64-66.

39. Solis J, Siegel J, Afonso CN et al. Experimental study of a self-starting Kerr-lens mode-locked titanium-doped sapphire laser. Opt Commun. 1996;123:547-552.

40. Moulton PF. Spectroscopic and laser characteristics of Ti:Al_2O_3. J Opt Soc Am B. 1986;3:125-132.

41. Barnes NP, Remelius DK. Ti:Al_2O_3 Laser Pumped by a Frequency Doubled Nd:YAG Laser. Byer RL, Gustafson EK, Trebino R. 51, 78-81. 1984. Springer Verlag. Tunable Solid State Lasers for Remote Sensing,Proc. of the NASA Conf.,1984.

42. Rines GA, Moulton PF. Performance of gain-switched Ti:Al_2O_3 unstable-resonator lasers. Opt Lett. 1990;15:434-436.

43. Vasa NJ, Okada T, Maeda M, Uchino O. Mechanism of a tuning operation of a Ti:sapphire laser by injection seeding. Jpn J Appl Phys. 1996;35:4333-4337.

44. Albers P, Stark E, Huber G. Continuous wave laser operation and quantum efficiency of titanium doped sapphire. J Opt Soc Am B. 1986;3:134-139.

45. Hoffstadt A. Design and performance of a high-average-power flashlamp-pumped Ti:Sapphire laser and amplifier. IEEE J Quantum Electron. 1997;33:1850-1863.

46. Hoffstadt A. High-average-power flash-lamp-pumped Ti:sapphire laser. Opt Lett. 1994;19:1523-1525.

47. Lutz Y, Hirth A, Von Salisch M. Optimization of the excitation characteristics of a flashlamp-pumped titanium sapphire laser. Opt Laser Technol. 1994;26:39-43.

48. Esterowitz L, Allen R, Khattak CP. Stimulated Emission from Flashpumped Ti:Al_2O_3. Hammerling P, Budgor AB, Pinto A. 47, 73-75. 1984. Springer Verlag. Tunable Solid State Lasers,Proc. of the First Int. Conf., 1984.

49. Sevast'yanov BK, Bagdasarov KhS, Fedorov EA, et al. Tunable laser based on Al_2O_3:Ti^{3+} crystal. Sov Phys Crystallogr. 1984;29:566-567.

50. Lacovara P, Esterowitz L, Allen R. Flash-lamp-pumped Ti:Al_2O_3 laser using fluorescent conversion. Opt Lett. 1985;10:273-275.

51. Brown AJW, Fisher CH. A 6.5 J Flashlamp-Pumped Ti:Al_2O_3 Laser. IEEE J Quantum Electron. 1993;29:2513-2517.

52. Sierra RA, Afzal RS. Flashlamp-pumped Ti:Sapphire Laser Technology. 726-727. 1992. IEEE Lasers and Electro-Optics Society.

53. Yu J, Douard M, Rambaldi P, Vezin B, Wolf JP. Laser-diode injection seeding of a flashlamp-pumped Q-switched $Ti:Al_2O_3$ laser oscillator. Opt Commun. 1996;132:263-268.

54. Segawa Y, Oda S, Kodama N. E/O Q-switching of a flashlamp-pumped Ti:sapphire laser. OSA Proceedings on advanced solid state lasers. 1991;10:149-152.

55. Sun X, Chen X, Li Z, et al. Q-switching and tuning of a flashlamp pumped Ti:Sapphire laser with electrooptic crystal. SPIE. 1998;3549:95-99.

56. Russell JA, Sierra RA. Flash-lamp-excited self-injection-seeded Q-switched $Ti:Al_2O_3$ laser oscillator. Appl Opt. 1996;35:4754-4757.

57. Titterton, D. H. and Stokeo, C. Progress with a flashlamp pumped titanium sapphire laser. SPIE 1995, 2380, 115-126.

58. Suzuki H, Kuribayashi O, Kannari F. Synchronous dual-wavelength operation of a self-injection-seeded narrow-linewidth flash-lamp-pumped Q-switched $Ti:Al_2O_3$ laser. Opt Lett. 1997;22:1710-1712.

59. Carts YA. Flashlamp pumps Ti:sapphire laser. Laser Focus World. 1989;8:21-24.

60. Hecht E. Optics . Second Edition. 1987. Addison-Wesley.

61. Zernike F, Midwinter JE. Applied Nonlinear Optics. 1972. John Wiley & sons.

62. Dmitriev VG, Gurzadyan GG, Nikogosyan DN. Handbook of nonlinear optical crystals. Second Edition. 1996. Springer-Verlag.

63. Bloembergen N. Conservation laws in nonlinear optics. J Opt Soc Am. 1980;70:1429-1436.

64. Kato K. Second harmonic generation in CDA and CD*A. IEEE J Quantum Electron. 1974;10:616-618.

65. Kato K. Efficienct second harmonic generation in CDA. Opt Commun . 1973;9:249-251.

66. Wu Y, Sasaki T, Nakai S et al. CsB_3O_5: A new nonlinear optical crystal. Appl Phys Lett. 1993;62:2614-2615.

67. Bhar GC, Das S, Datta PK. Efficiency frequency doubling of Nd laser radiation. Physica Status Solidi-A. 1990;119:173-176.

68. Chen C, Wu Y, Jiang A et al. New nonlinear-optical crystal: LiB_3O_5. J Opt Soc Am B. 1989;6:616-621.

69. Zumsteg FC, Bierlein JD, Gier TE. $K_xRb_{1-x}TiOPO_4$: A new nonlinear optical material. J Appl Phys. 1976;47:4980.

70. Dowley MW, Hodges EB. Studies of high power CW and quasi-CW parametric UV generation by ADP and KDP in Argon-ion laser cavity. IEEE J Quantum Electron. 1968;4:552-558.

71. Machewirth VP, Webb R, Anafi D. High power harmonics produced with high efficiency in KD*P. Laser Focus. 1976;12:104-107.

72. Butyagin OF, Kazakov AA, Kolyushenko EA. Characteristics of second harmonic intensity distribution at the output of a linearly inhomogeneous medium. Opt Spectrosc. 1974;36:112-115.

73. Deserno U, Nath G. A new stable high power giant-pulse laser at 0.53μ using $LiIO_3$. Phys Lett. 1969;30A:483-484.

74. Yap YK, Haramura S, Taguchi A, Mori Y, Sasaki T. $CsLiB_6O_{10}$ crystal for frequency doubling the Nd:YAG laser. Opt Commun. 1998;145 :101-104.

75. Chen C, Wu B, Zeng W, Wang Y, Ye N, Yu L. New nonlinear optical crystal $Sr_2Be_2B_2O_7$: Growth and Properties. 229-230. 1996. CLEO '96.

76. Mei L, Wang Y, Chen C, Wu B. Nonlinear optical materials based on $MBe_2BO_3F_2$ (M=Na,K). J Appl Phys. 1993;74:7014-7015.

77. Kato K. Frequency conversion of Nd:YAG laser radiation in RDA. Opt Commun. 1975;13:93-95.

78. Kato K, Nakao S. Frequency doubling of Nd:YAG laser radiation in RDP. Jpn J Appl Phys. 1974;13:1681-1682.

79. Barnes NP, Gettemy DJ, Adhav RS. Variation of the refractive index with temperature and the tuning rate for KDP isomorphs. J Opt Soc Am. 1982;72:895-898.

80. Kato K. Temperature-tuned 90° phase-matching properties of LiB_3O_5. IEEE J Quantum Electron. 1994;30:2950-2952.

81. Lin JT, Montgomery JL, Kato K. Temperature tuned noncritically phase matched frequency conversion in LiB_3O_5 crystal. Opt Commun. 1990;80:159-165.

82. Lin S, Sun Z, Wu B, Chen C. The nonlinear optical characteristics of a LiB_3 O_5 crystal. J Appl Phys. 1990;67:634-638.

83. Belt RF, Gashurov G, Liu YS. KTP as a harmonic generator for Nd:YAG lasers. Laser Focus. 1985;21:110-124.

84. Boulanger B, Rousseau I, Feve JP et al. Optical studies of laser induced gray tracking in KTP. IEEE J Quantum Electron. 1999;35:281-286.

85. Roth M, Angert N, Tseitlin M, Alexandrovski A. On the optical quality of KTP crystals for nonlinear optical and electro-optic applications. Opt Mater. 2001;16:131-136.

86. Motokoshi S, Jitsuno T, Nakatsuka M, Izawa Y. Evaluation of KTiOPO4 crystals for high power laser. SPIE. 2000;3902:423-427.

87. Pierce JW, Beausoleil RG. High efficiency fourth harmonic generation. SPIE. 1995;265-281.

88. Marshall CD, Payne SA, Henesian MA, Speth JA, Powell HT. Ultraviolet-induced transient absorption in potassium dihydrogen phosphate and its influence on frequency conversion. J Opt Soc Am B. 1994;11:774-785.

89. Kato K. Phase matched generation of 2128 Å in $KB_5O_8.4H_2O$. Opt Commun. 1976;19:332-333.

90. Kato K. High efficiency high power UV generation at 2128 Å in urea. IEEE J Quantum Electron. 1980;16:810-811.

91. Kato K. Fourth and fifth harmonic generation of Nd:YAG laser radiation in beta-BaB_2O_4. Review of Laser Engineering. 1990;18:3-7.

92. Lago A, Wallenstein R, Chen C, Fan YX, Byer RL. Coherent 70.9-nm radiation generated in neon by frequency tripling the fifth harmonic of a Nd:YAG laser. Opt Lett. 1988;13:221-223.

93. Yap YK, Inagaki M, Nakajima S, Mori Y, Sasaki T. High-power fourth-and fifth-harmonic generation of a Nd:YAG laser by means of a $CsLiB_6O_{10}$. Opt Lett. 1996;21:1348-1350.

94. Mori Y, Nakajima S, Miyamoto A, Inagaki M, Sasaki T. Generation of ultraviolet light by using new nonlinear optical crystal $CsLiB_6O_{10}$. SPIE. 1995;2633:299-307.

95. Ryu G, Yoon CS, Han TPJ, Gallagher HG. Growth and characterisation of $CsLiB_6O_{10}$ (CLBO) crystals. J Cryst Growth. 1998;191:492-500.

96. Yap YK, Inoue T, Sakai H et al. Long-term operation of $CsLiB_6O_{10}$ at elevated crystal temperature. Opt Lett. 1998;23:34-36.

97. Kojima T, Konno S, Fujikawa S et al. 20-W ultraviolet beam generation by fourth harmonic generation of an all solid state laser. Opt Lett. 2000;25:58-60.

98. Nebel A, Beigang R. External frequency conversion of cw mode-locked $Ti:Al_2O_3$ laser radiation. Opt Lett. 1991;16:1729-1731.

99. Krylov V, Kalintsev A. Second, third and fourth harmonic generation of amplified femtosecond Ti:sapphire laser pulses. SPIE. 1996;2701:24-30.

100. Zhou W-L, Mori Y, Sasaki T, Nakai S. High-efficiency intracavity continuous-wave ultraviolet generation using crystals $CsLiB_6O_{10}$, β-BaB_2O_4 and LiB_3O_5. Opt Commun. 1996;123:583-586.

101. Skripko GA, Bartoshevich SG, Mikhnyuk IV, Tarazevich IG. LiB_3O_5: a highly efficient frequency converter for Ti:sapphire lasers. Opt Lett. 1991;16:1726-1728.

102. Chen D, Lin JT. Temperature-tuned phase-matching properties of LiB_3O_5 for Ti:sapphire laser frequency doubling. IEEE J Quantum Electron. 1993;29:307-310.

103. Kato K. Second-harmonic generation to 2048 A in β-BaB_2O_4. IEEE J Quantum Electron. 1986;QE-22:1013-1014.

104. Bourzeix S, de Beauvoir B, Nez F et al. Ultra-violet generation at 205 nm by two frequency doubling steps of a cw titanium-sapphire laser. Opt Commun. 1997;133:239-244.

105. Seifert F, Ringling J, Noack F, Kittelmann O, Petrov V. All-solid-state laser system for the generation of tunable femtosecond light pulses in the vacuum uv down to 172.7 nm. SPIE. 1995;2380, 73-79.

106. Petrov V, Rotermund F, Noack F et al. Frequency conversion of Ti:sapphire based femtosecond laser systems to the 200 nm spectral region using nonlinear optical crystals. IEEE J Sel Top Quant. 1999;5:1532-1542.

107. Rotermund F, Petrov V. Generation of the fourth harmonic of a femtosecond Ti:sapphire laser. Opt Lett. 1998;23:1040-1042.

108. Ringling J, Kittelmann O, Noack F, Korn G, Squier J. Tunable femtosecond pulses in the near vacuum ultraviolet generated by frequency conversion of amplified Ti:sapphire laser pulses. Opt Lett. 1993;18:2035-2037.

109. Sakuma J, Deki K, Finch A, Ohsako Y, Yokota T. All solid state, high power, deep uv system based on cascaded sum frequency mixing in $CsLiB_6O_{10}$ crystals. Appl Opt. 2000;39:5505-5511.

110. Bhar GC, Kumbhakar P, Chatterjee U, Rudra AM, Nagahori A. Widely tunable deep ultraviolet generation in CLBO. Opt Commun. 2000;176:199-205.

111. Umemura N, Kato K. Ultraviolet generation tunable to 0.185 μm in $CsLiB_6O_{10}$. Appl Opt. 1997;36:6794-6796.

112. Min Z, Quandt RW, Bersohn R, Kim HL. Extended range of second harmonic generation in β-BaB_2O_4. IEEE J Quantum Electron. 1998;34:2409.

113. Srinivasan R. Kinetics of the ablative photodecomposition of organic polymers in the far ultraviolet (193 nm). J Vac Sci Technol B. 1983;1:923-925.

114. Srinivasan R, Dyer PE, Braren B. Far-ultraviolet laser ablation of the cornea: Photoacoustic studies. Lasers Surg Med. 1987;6:514-519.

115. Aron-Rosa DS, Boulnoy JL, Carré F et al. Excimer laser surgery of the cornea: Qualitative and quantitative aspects of photoablation according to the energy density. J Cataract Refract Surg. 1986;12:27-33.

116. Van Saarloos PP, Constable IJ. Bovine Corneal Stroma Ablation Rate With 193-nm Excimer Laser Radiation: Quantitative Measurement. J Refract Corneal Surg. 1990;6:424-429.

117. Puliafito CA, Steinert RF, Deutsch TF et al. Excimer laser ablation of the cornea and lens. Experimental studies. Ophthalmology. 1985;92:741-748.

118. Lembares A, Hu X-H, Kalmus GW. Absorption spectra of corneas in the far ultraviolet region. Inves Ophthalmol Vis Sci. 1997;38:1283-1287.

119. Krueger RR, Trokel SL, Schubert HD. Interaction of ultraviolet laser light with the cornea. Inves Ophthalmol Vis Sci. 1985;26:1455-1464.

120. Berns MW, Chao L, Giebel AW et al. Human corneal ablation threshold using the 193nm ArF excimer laser. Inves Ophthalmol Vis Sci. 1999;40:826-830.

121. Pettit GH, Ediger MN, Weiblinger RP. Excimer laser ablation of the cornea. Opt Eng. 1995;34:661-667.

122. Pettit GH, Ediger MN. Corneal-tissue absorption coefficients for 193- and 213-nm ultraviolet radiation. Appl Opt. 1996;35:3386-3391.

123. Yablon AD, Nishioka NS, Mikic BB, Venugopalan V. Measurement of tissue absorption coefficients by use of interferometric photothermal spectroscopy. Appl Opt. 1999;38:1259-1272.

124. Trokel SL, Srinivasan R, Braren B. Excimer laser surgery of the cornea. Am J Ophth. 1983;96:710-715.

125. Krueger RR, Trokel SL. Quantitation of corneal ablation by ultraviolet laser light. Arch Ophthalmol. 1985;103:1741-1742.

126. Sutcliffe E, Srinivasan R. Dynamics of UV laser ablation of organic polymer surfaces. J Appl Phys. 1986;60:3315-3322.

127. Dyer PE, Srinivasan R. Nanosecond photoacoustic studies on ultraviolet laser ablation of organic polymers. Appl Phys Lett. 1986;48:445-447.

128. Srinivasan R, Sutcliffe E. Dynamics of the ultraviolet laser ablation of corneal tissue. Am J Ophth. 1987;103:470-471.

129. Hu X-H, Juhasz T. Study of corneal ablation with picosecond laser pulses at 211 nm and 263 nm. Lasers Surg Med. 1996;18:373-380.

130. Srinivasan R, Braren B. Influence of pulse width on ultraviolet laser ablation of poly(methylmethacrylate). Appl Phys Lett. 1988;53:1233-1235.

131. Kahle G, Städter H, Seiler T, Wollensak J. Gas chromatographic and mass spectroscopic analysis of excimer and erbium: yttrium aluminum garnet laser-ablated human cornea. Inves Ophthalmol Vis Sci. 1992;33:2180-2184.

132. Koren G, Yeh JTC. Emission spectra and etching of polymers and graphite irradiated by excimer lasers. J Appl Phys. 1984;56:2120-2126.

133. Hahn DW, Ediger MN, Pettit GH. Dynamics of ablation plume particles generated during excimer laser corneal ablation. Lasers Surg Med. 1995;16:384-389.

134. Srinivasan R, Braren B, Casey KG, Yeh M . Ultrafast imaging of ultraviolet laser ablation and etching of polymethylmethacrylate. Appl Phys Lett. 1989;55:2790-2791.

135. Siano S, Pini R, Rossi F, Salimbeni R, Gobbi PG. Acoustic focusing associated with excimer laser ablation of the cornea. Appl Phys Lett. 1998;72:647-649.

136. Krueger RR, Krasinski JS, Radzewicz C, Stonecipher KG, Rowsey JJ. Photography of shock waves during excimer laser ablation of the cornea. Cornea. 1993;12:330-334.

137. Noack J, Tönnies R, Hohla K, Birngruber R, Vogel A. Influence of ablation plume dynamics on the formation of central islands in excimer laser photorefractive keratectomy. Ophthalmology. 1997;104:823-830.

138. Bor Z, Hopp B, Rácz B et al. Plume Emission, Shock Wave and Surface Wave Formation During Excimer Laser Ablation of the Cornea. J Refract Corneal Surg. 1993;9:S111-S115.

139. Liu X, Mourou G. Ultrashort laser pulses tackle precision machining. Laser Focus World. 1997;8 :101-118.

140. Mainster MA, Sliney DH, Belcher CD, Buzney SM. Laser Photodisruptors - Damage Mechanisms, Instrument Design and Safety. Ophthalmology. 1983;90:973-991.

141. Hanuch OE, Agrawal VB, Bassage S, del Cerro M, Aquavella JV. Myopic picosecond laser keratomileusis with the Neodymium-Yttrium Lithium Fluoride laser in the cat cornea. Ophthalmology. 1998;105:142-149.

142. Niemz MH. Threshold dependence of laser-induced optical breakdown on pulse duration. Appl Phys Lett. 1995;66:1181-1183.

143. Stern D, Schoenlein RW, Puliafito CA et al. Corneal ablation by nanosecond, picosecond, and femtosecond lasers at 532nm and 625nm. Arch Ophthalmol. 1989;107:587-592.

144. Loesel FH, Niemz MH, Bille JF, Juhasz T. Laser-induced optical breakdown on hard and soft tissues and its dependence on the pulse duration: Experiment and model. IEEE J Quantum Electron. 1996;32:1717-1722.

145. Oraevsky AA, Da Silva LB, Rubenchik AM et al. Plasma mediated ablation of biological tissues with nanosecond-to-femtosecond laser pulses: Relative role of linear and nonlinear absorption. IEEE J Sel Top Quant. 1996;2:801-809.

146. Vogel A, Busch S, Jungnickel K, Birngruber R. Mechanisms of intraocular photodisruption with picosecond and nanosecond laser pulses. Lasers Surg Med. 1994;15:32-43.

147. Zysset B, Fujimoto JG, Puliafito CA, Birngruber R, Deutsch TF. Picosecond optical breakdown: Tissue effects and reduction of collateral damage. Lasers Surg Med. 1989;9:193-204.

148. Loesel FH, Kurtz RM, Horvath C, Sayegh S, Mourou G, Bille JF, Juhasz T. Ultra-precise medical applications with ultrafast lasers: corneal surgery with femtosecond lasers. SPIE. 1998; 3564, 86-93.

149. Juhasz T, Hu X-H, Turi L, Bor Z. Dynamics of shock waves and cavitation bubbles generated by picosecond laser pulses in corneal tissue and water. Lasers Surg Med. 1994;15:91-98.

150. Vogel A, Capon MRC, Asiyo-Vogel MN, Birngruber R. Intraocular photodisruption with picosecond and nanosecond laser pulses: Tissue effects in cornea, lens, and retina. Inves Ophthalmol Vis Sci. 1994;35:3032-3044.

151. Hale GM, Querry MR. Optical constants of water in the 200nm to 200μm wavelength region. Appl Opt. 1973;12:555-563.

152. Niemz MH. Laser-Tissue Interactions. First Edition. 1996. Springer.

153. Hoffman HJ, Telfair WB. Photospallation: A new theory and mechanism for mid-infrared corneal ablations. J Refract Surg. 2000;16:90-94.

154. Telfair WB, Bekker C, Hoffman HJ et al. Histological comparison of corneal ablation with Er:YAG laser, Nd:YAG optical parametric oscillator, and excimer laser. J Refract Surg . 2000;16:40-50.

155. Gailitis P, Ren Q, Thompson KP, Lin JT, Waring GO. Solid State Ultraviolet Laser (213nm) Ablation of the Cornea and Synthetic Collagen Lenticules. Lasers Surg Med. 1991;556-562.

156. Shen J-H, Joos KM, Manns F et al. Ablation rate of PMMA and human cornea with a frequency-quintipled Nd:YAG laser (213 nm). Lasers Surg Med. 1997;21:179-185.

157. Puliafito CA, Wong K, Steinert RF. Quantitative and ultrastructural studies of excimer laser ablation of the cornea at 193 and 248 nanometers. Lasers Surg Med. 1987;7:155-159.

158. Campos M, Wang XW, Hertzog L et al. Ablation rates and surface ultrastructure of 193nm excimer laser keratectomies. Inves Ophthalmol Vis Sci. 1993;34:2493-2500.

159. Seiler T, Kriegerowski M, Schnoy N, Bende T. Ablation rate of human corneal epithelium and Bowman's layer with the excimer laser (193nm). Refract Corneal Surg. 1990;6:99-102.

160. Al-qahtani JM, McLean IW, Weiblinger RP, Ediger MN. Preliminary in vitro study of the histological effects of low fluence 193nm excimer laser irradiation of corneal tissue. J Refract Surg. 2001;17:105-109.

161. Fantes FE, Waring GO. Effect of excimer laser radiant exposure on uniformity of ablated corneal surface. Lasers Surg Med. 1989;9:533-542.

162. Junqueira LC, Carneiro J, Kelley RO. Basic Histology. 6th Edition. 1989. Appleton and Lang.

163. Bachmann W, Jean B, Bende T et al. Silicon cast method for quantification of photoablation. Refract Corneal Surg. 1992;8:363-367.

164. Dougherty PJ, Wellish KL, Maloney RK. Excimer laser ablation rate and corneal hydration. Am J Ophth. 1994;118:169-176.

165. Huebscher H, Genth U, Seiler T. Determination of excimer laser ablation rate of the human cornea using in vivo scheimpflug videography. Inves Ophthalmol Vis Sci. 1996;37:42-46.

166. Sciberras HC. Refractive index of corneal stroma. 2002.

167. Caughey TA, Cheng F-C, Trokel SL et al. An investigation of laser-tissue interaction of a 213 nm laser beam with animal corneas. Lasers Light Ophthalmol. 1994;6:77-85.

168. Jones AJ, Denning NT. Polymeric biomaterials. 1989.

169. Know Your Plastics. Second Edition. 1992. Plastics Institute of Australia.

170. Park JB, Lakes RS. Chapter 7 Polymeric implant materials. Biomaterials: An introduction. Second Edition, 141-168. 1992. Plenum Press.

171. Fuxbruner A, Hemo I, Lewis A et al. Controlled lens formation with unapertured excimer lasers: use with organic polymers and corneal tissues. Appl Opt. 1990;29:5380-5386.

172. Srinivasan R, Braren B, Dreyfus RW, Hadel L, Seeger DE. Mechanism of the ultraviolet laser ablation of polymethylmethacrylate at 193 and 248nm: laser-induced fluorescence analysis, chemical analysis, and doping studies. J Opt Soc Am B. 1986;3:785-791.

173. Van Saarloos PP, Constable IJ. Quantitative measurement of the ablation rate of poly(methyl methacrylate) with 193-nm excimer laser radiation. J Appl Phys. 1990;68:377-379.

174. Philipp HR, Cole HS, Liu YS, Sitnik TA. Optical absorption of some polymers in the region 240-170nm. Appl Phys Lett. 1986;48:192-194.

175. Lin JT. A multi-wavelength solid state laser for ophthalmic applications. SPIE. 1992;1644:266-275.

176. Chirila TV, Van Saarloos PP. Ablation of Ploy(2-Hydroxyethyl Methacrylate) by 193nm excimer laser radiation. J Appl Polym Sci. 1992;44:1355-1363.

177. Costela A, Figuera JM, Florido F et al. Ablation of poly(methyl methacrylate) and poly(2-hydroxyethylmethacrylate) by 308, 222 and 193nm excimer laser radiation. Applied Physics A. 1995;60:261-270.

178. Ren Q, Gailitis P, Thompson KP, Lin JT. Ablation of the cornea and synthetic polymers using a uv (213 nm) solid-state laser. IEEE J Quantum Electron. 1990;26:2284-2288.

179. Ren Q, Simon G, Parel J-M. Ultraviolet solid-state laser (213 nm) photorefractive keratectomy: in vitro study. Ophthalmology. 1993;100:1828-1834.

180. Ren Q, Simon G, Legeais J-M et al. Ultraviolet solid-state laser (213 nm) photorefractive keratectomy: in vivo study . Ophthalmology. 1994;101:883-889.

181. Kornmehl EW, Steinert RF, Puliafito CA. A comparative study of masking fluids for excimer laser phototherapeutic keratectomy. Arch Ophthalmol.1991;109:860-863.

182. Förster W, Grewe S, Atzler U, Lunecke C, Busse H. Phototherapeutic keratectomy in corneal diseases. J Refract Corneal Surg . 1993;9:S85-S90.

183. Welz, B. Atomic Absorption Spectrometry. Second Edition. 1985. Verlag Chemie.

184. Krauss JM, Puliafito CA, Steinert RF. Laser interactions with the cornea. Surv Ophthalmol. 1986;31:37-53.

185. Azzolini C, Gobbi PG, Brancato R et al. Interaction between infrared radiation and vitreous substitutes. Arch Ophthalmol. 1997;115:899-903.

186. Reid PG, Sciberras HC, Wang Z, Dair GT. Improved crystal mounting in solid state laser systems. International patent application No. PCT/AU01/01341. Priority date: 19/10/2000.

187. Machat JJ. Chapter 3. Fundamental concepts and principles of the excimer laser and LASIK. The art of LASIK. Second Edition, 41-43. 1999. New Jersey, Slack Incorporated.

188. Tsuruta T, Hayashi T, Kataoka K, Ishihara K, Kimura Y. Biomedical applications of polymeric materials. 1993. CRC Press.

189. Monti P, Simoni R. The role of water in the molecular structure and properties of soft contact lenses and surface interactions. J Mol Struct. 1992;269:243-255.

190. Chirila TV. Modern artificial corneas: the use of porous polymers. Trends Polym Sci. 1994;2:296-300.

191. Chirila TV. An overview of the development of artificial corneas with porous skirts and the use of PHEMA for such an application. Biomaterials. 2001;22:3311-3317.

192. Brown TL, LeMay HE, Bursten BE. Chapter 12. Modern materials. Chemistry: The central science . Fifth Edition, 405-435. 1991. Prentice Hall.

193. Maurice DM. Some puzzles in the microscopic structure of the stroma. J Refract Surg. 1999;15:692-694.

194. Feltham MH, Stapleton F. The effect of water content on the 193nm excimer laser ablation. Clin Exp Ophthalmol. 2002;30:99-103.

195. Doughty MJ, Aakre BM, Patel S. Hydration (water binding) of the mammalian corneal stroma ex vivo and in vitro: sample mass and error considerations. Optometry Vision Sci. 1996;73:666-675.

196. Lubatschowski H, Kermani O, Welling H, Ertmer W. A scanning and rotating slit ArF excimer laser delivery system for refractive surgery. J Refract Surg. 1998;14:S186-S191.

197. Fields CR, Taylor SM, Barker FM. Effect of Corneal Edema Upon the Smoothness of Excimer Laser Ablation. Optometry Vision Sci. 1994;71:109-114.

198. Keates RH, Bloom RT, Schneider RT et al. Absorption of 308-nm excimer laser radiation by balanced salt solution, sodium hyaluronate, and human cadaver eyes. Arch Ophthalmol. 1990;108:1611-1613.

199. Huibers PDT. Models for the wavelength dependence of the index of refraction of water. Appl Opt. 1997;36:3785-3787.

200. Kim WS, Jo JM. Corneal hydration affects ablation during laser in situ keratomileusis surgery. Cornea. 2001;20:394-397.

201. Feltham MH, Stapleton F. Change in central corneal thickness following laser in situ keratomileusis for myopia. Clin Exp Ophthalmol. 2000;28:185-187.

202. Campos M, Cuevas K, Garbus J, Lee M, Donnell PJ. Corneal wound healing after excimer laser ablation: Effects of nitrogen gas blower. Ophthalmology. 1992;99:893-897.

203. Krueger RR, Campos M, Wang XW, Lee M, McDonnell PJ. Corneal surface morphology following excimer laser ablation with humidified gases. Arch Ophthalmol. 1993;111:1131-1137.

204. Thompson V, Durrie DS, Cavanaugh TB. Philosophy and technique for excimer laser phototherapeutic keratectomy. J Refract Corneal Surg. 1993;9:S81-S85.

205. Horgan SE, McLaughlin-Borlace L, Stevens JD, Munro PMG. Phototherapeutic smoothing as an adjunct to photorefractive keratectomy in porcine corneas. J Refract Surg. 1999;15:331-333.

206. Van Haeringen NJ. Clinical biochemistry of tears. Surv Ophthalmol. 1981;26:84-95.

Publications and presentations resulting from this project

Dair GT, Eikelboom RH, Ashman RA, van Saarloos PP, Reid PG, Reinholz F.

Absorption of 193 and 213nm refractive laser wavelengths in saline and balanced salt solution.

Archives of Ophthalmology, 2001, 119(4), 533-537.

Dair GT, Pelouch WS, van Saarloos PP, Lloyd DJ, Paz-Linares SM, Reinholz F.

Investigation of corneal ablation efficiency using 213nm solid state laser pulses.

Investigative Ophthalmology and Visual Science, 1999, 40, 2752-2756.

Dair GT, Crawford G, Ashman RA, van Saarloos PP, Keller P.

Can BSS be used to mask 193 and 213nm laser wavelengths.

World Refractive Surgery Symposium, Dallas USA October 2000. (Oral presentation)

Eikelboom RH, Dair GT, Ashman RA, van Saarloos PP, Sciberras HC, Reid PG.

Saline is a barrier to 193nm laser ablation, but not to 213nm solid state laser ablation,

ARVO Conference, Fort Lauderdale USA May 2000. (Poster presentation)

Pelouch WS, van Saarloos PP, Dair GT, Lloyd DJ, Paz S

Results of corneal ablation by ultraviolet 213nm laser pulses

ARVO Conference, Fort Lauderdale USA May 1998, (Oral presentation)

U.S patent application No. 10/124,445 and Australian patent application No. 2754/02 **"Masking agent"**, Inventors: **Geoffrey T. Dair, Hank C. Sciberras, Sharon L. Humphris**, Priority date: 27/04/01

List of Figures

List of Tables